HARVARD UNIVERSITY
Graduate School of Arts and Sciences

DISSERTATION ACCEPTANCE CERTIFICATE

The undersigned, appointed by the

Harvard John A. Paulson School of Engineering and Applied Sciences

have examined a dissertation entitled:

"Electrode Suspensions with Tailored Flow Behavior and Electrochemical Performance for Multiscale Lithium Ion Batteries"

presented by: Teng-Sing Wei

candidate for the degree of Doctor of Philosophy and here by certify that it is worthy of acceptance.

Signature _____

Typed name: Professor J. Lewis

Signature _____

Typed name: Professor M. Aziz

Signature _____

Typed name: Professor V. Manoharan

Date: April 17, 2017

Electrode Suspensions with Tailored Flow Behavior and Electrochemical Performance for Multiscale Lithium Ion Batteries

A dissertation presented

by

Teng-Sing Wei

to

The John A. Paulson School of Engineering and Applied Sciences

in partial fulfillment of the requirements for the degree of

Doctor of Philosophy

in the subject of

Applied Physics

Harvard University

Cambridge, Massachusetts

May 2017

Dissertation Advisor: Jennifer A. Lewis Teng-Sing Wei

Electrode Suspensions with Tailored Flow Behavior and Electrochemical Performance for Multiscale Lithium Ion Batteries

Abstract

Rechargeable Li-ion batteries (LIBs) are widely used in applications ranging from portable electronics to electric vehicles. They are also being explored for grid-scale energy storage. To date, commercial LIBs have been confined to coin, cylinder, prismatic and pouch cells, which are composed of thin electrode layers (20-100 μm thick). However, the growing demand for LIBs with higher capacity, faster charge-discharge rates, lower cost, and customized form factors underscores the need for new electrode materials, battery architectures, and fabrication methods.

My Ph.D. dissertation focuses on fabricating high energy density Li-ion batteries with ultrathick (up to 1.5 mm), biphasic, semisolid electrodes for use in applications ranging from customized Li-ion microbatteries to semisolid flow cells. As an initial demonstration, we printed Li-ion microbatteries (< 1 mm^3 in volume) in the form of interdigitated, high aspect ratio LFP/LTO electrodes on patterned gold current collectors, which deliver an areal capacity of ~1.5 mAh cm^{-2} at a discharge rate below 5C.

To improve their electronic transport and area capacity, we created biphasic semisolid electrode inks that are electrolyte-infused for printing LIBs with ultrathick electrodes (~ 1 mm). Specifically, the interactions between the active particles, LFP or LTO, are rendered repulsive, while those between the conductive carbon particles are attractive. Our biphasic ink design enables high solids loading of active materials within

a percolative network of conductive carbon particles, which gives rise to electrodes that simultaneously exhibit good flowability, charge transport, and high energy density. These fully 3D printed and packaged LIBs exhibit an areal capacity more than an order of magnitude higher than the micro-LIBs with exceptional cycling performance.

As a final demonstration, we used these biphasic electrode suspensions in semisolid flow batteries. Their quick and efficient charge transport reduces overpotential during cell cycling using 1.5 mm thick semisolid electrodes. Based on these measured properties, we also developed an analytical model that predicts the pressure drop required for a given target current. These efficient and scalable biphasic semisolid flow cells offer a promising approach for grid-scale energy storage.

Acknowledgements

I would like to thank my wife, Whitney Bai, for her love, support, and encouragement throughout the challenging Ph.D. program. Your thoughtfulness has kept me healthy, positive, and motivated to continue to move forward on this journey. I am truly blessed as I could not have asked for a better life partner than you.

I would like to express deep gratitude to my advisor, Jennifer Lewis, for your continual support and teaching for not only my research, but also to foster a tenacious and resilient mentality in me. I am privileged to have such an innovative mentor who inspires me to constantly seek out the unexplored, less traveled directions in the field. Your honorable work ethic, attention to detail, effective communication, and the ability to efficiently capture the essence of an idea continue to drive me to improve.

I wish to also thank the Lewis group battery team members, my patient lab mentor Bok Yeop Ahn, and my capable undergraduate assistant Julia Grotto. Your help has been essential to the success of this work. The brainstorming and troubleshooting discussions we've had drove this project forward in ways that I could not have realized alone.

I am very proud to be a part of the Lewis Group, where members are genuinely nice, positive, supportive, and collaborative and open discussions are promoted and minds are freed to pursue cool ideas. I want to thank many present and past members, namely, Scott Slimmer, Lori Sanders, Joseph Muth, David Kolesky, Jochen Mueller, Thomas Ober, James Hardin, Sydney Gladman, Alex Valentine, Ryan Truby, Mike Lis, Jordan Raney, Mark Skylar-Scott, Kimberly Homan, Daniele Foresti, Sebastien Uzel, Class Visser, Brett Compton, Arda Kotikian, Nanjia Zhou, Will Boley, Kundan Chaudhary, Analisa Russo, Chris Hansen, Lucas Osterbut, Steve Kranz, John Vericella, David Lorang,

Brett Walker, Jaime Jaurez, Travis Busbee, Michael Bell, Koseki Kobayashi, John Ahrens, Katharina Kroll, Nicole Black, and Tina Knight.

I also want to thank my collaborators outside of the Lewis lab, including Professors Shen Dillon, Kyle Smith, Yet-Ming Chiang, Gareth McKinley, Jeffrey Moore, Joaquín Rodríguez-Lopez, and Dr. Jung Yoon Seo, Dr. Ahmed Helal, Elena Montoto, Vinay Iyer, and particularly Dr. Frank Fan and Dr. Ke Sun. You have not only helped complete this work, but also greatly facilitated my understanding in the field of electrochemistry.

I want to thank my dissertation committee and qualification exam committee members, Professors Michael Aziz, Vinothan Manoharan, Dave Weitz, and Frans Spaepen for your support and guidance with invaluable feedback and suggestions.

Finally, I would also like to thank my family for always believing in me and for living your lives so wonderfully, being great role models for me to learn from. I can always count on you to provide guidance when I am in need. I want to especially thank my parents Yau-Huei Wei and Yeh-Jen Lin for so prudently investing in me and providing me with a quality education and many life experiences that have allowed me to become the person I am today.

Table of contents

Chapter 1

Introduction

Li-ion batteries (LIBs) (**Figure 1.1**) have been adopted for applications ranging from portable electronics to electric automobile. They are also being explored for grid-scale storage due to their exceptional energy efficiency, high energy density, and low self-discharge characteristics compared to other secondary batteries[1] (**Figure 1.2a**). To date, Li-ion battery technology has achieved a 3-fold increase in energy density and a 10-fold reduction in cost[1] (**Figure 1.2b**).

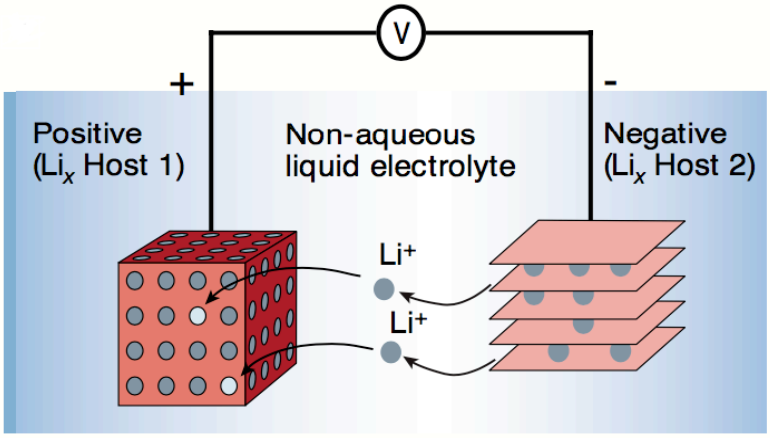

Figure 1.1: Schematic representation and operating principles of Li-ion batteries. Adapted from: [2]

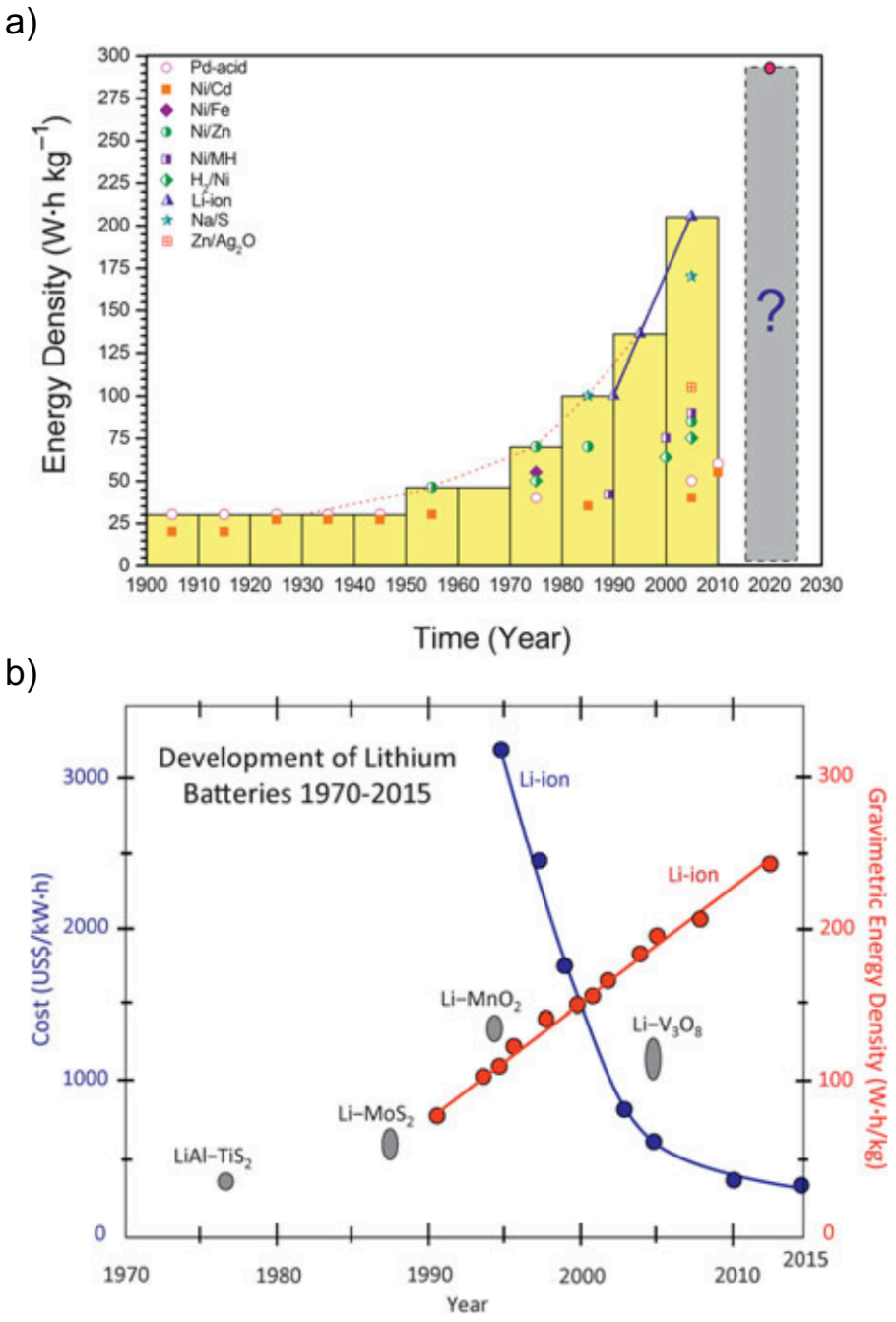

Figure 1.2: (a) History of the development of the energy density of secondary batteries based on different chemistries. The dashed line shows the progress of the past 80 years, and the solid line shows the progress in Li-ion batteries from commercialization in 1991 to 2010. Adapted from: [1] (b) Development of lithium batteries during the period of 1970–2015, showing the cost (blue, left axis) and gravimetric energy density (red, right axis) of Li-ion batteries following their commercialization by Sony in 1991. The gravimetric energy densities of Li- or LiAl-metal anode batteries against four cathodes, commercialized in the years indicated and withdrawn from the market for reasons of safety or market appeal, are shown in gray and refer to the right axis. Adapted from: [1]

LIBs used in personal electronics are available in a limited number of form factors, including cylindrical, coin, prismatic and pouch cells. As these devices become smaller, there will be a need for creating microscale LIBs in customized sizes and shapes (**Figure 1.3**). At a much larger scale, the growing adoption of renewable energy technologies, e.g., wind and solar, have created a pressing need for alternatives to geographically-limited pumped hydro-electric systems[3] (**Figure 1.4**). LIBs are one of the front runners to fulfill the promise of grid-scale energy storage systems. It is worth noting that LIBs are also the top choice of the electric vehicle sector, which has contributed to the rapidly falling cost of LIB packs. [4]

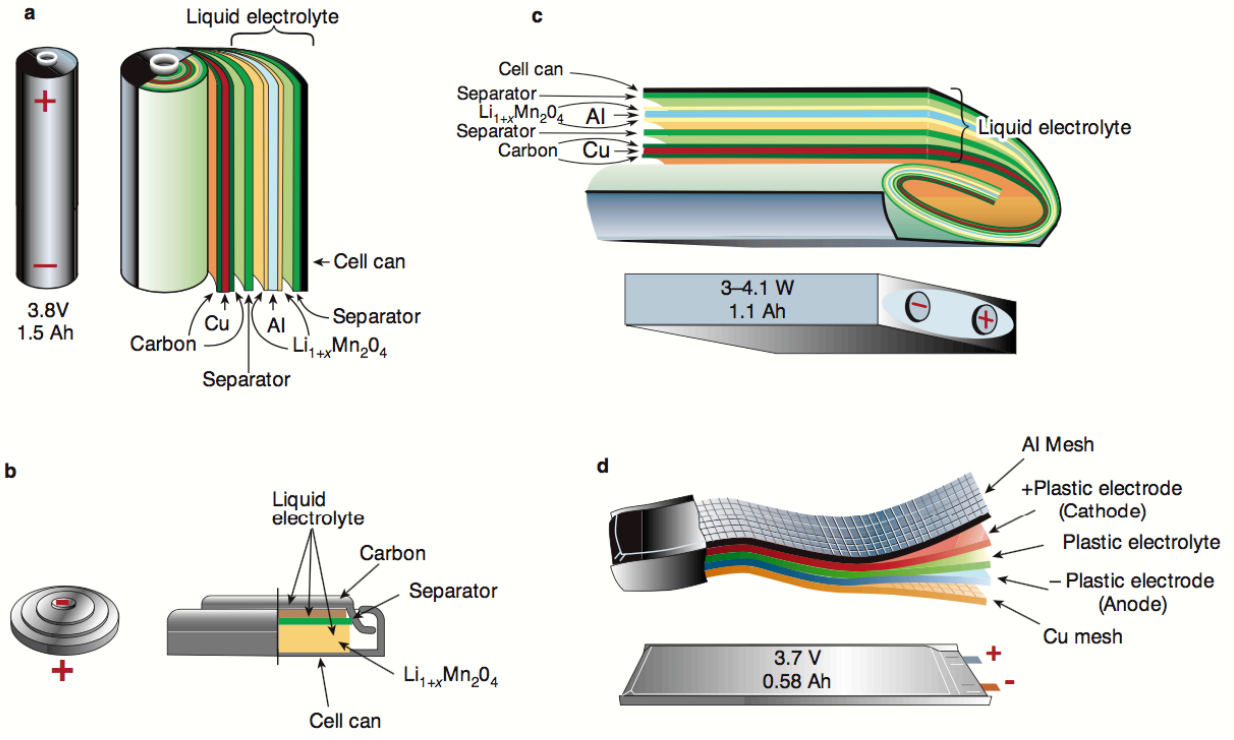

Figure 1.3: Schematic showing the shape and components of the common Li-ion cell configurations: a) cylindrical, b) coin, c) prismatic, and d) pouch. Adapted from: [2]

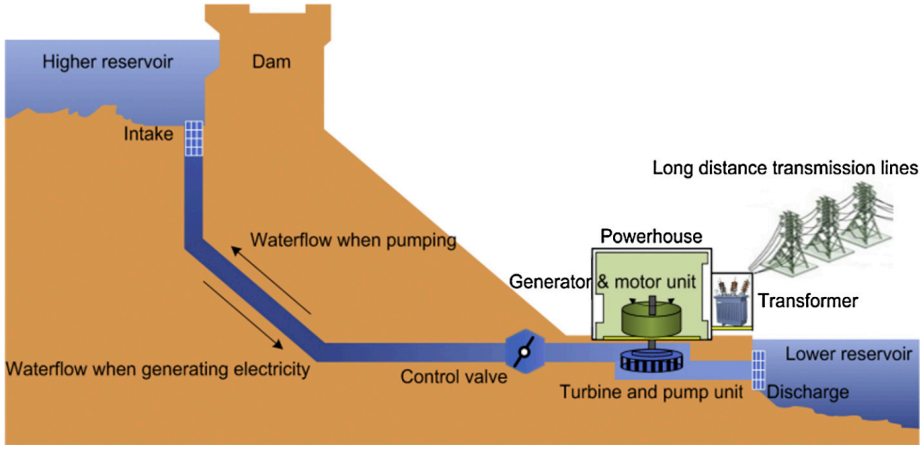

Figure 1.4: Schematic showing a pumped hydro-electric system. Adapted from: [5]

Looking ahead, it is clear that LIBs will play a major role for micro- to macro-scale energy storage applications. Hence, further improvement in their energy and power density is a top priority. The energy density of LIBs is generally determined by the areal capacity of its electrodes [6], hence recent efforts have focused on optimizing electrode composition to achieve fast ionic and electronic transport in batteries with ultrathick electrodes. My Ph.D. dissertation focuses on developing electrode suspensions with tailored flow behavior and electrochemical performance for both micro-LIBs in customized form factors and semisolid flow batteries.

1.1 Dissertation Scope

The first aim of my dissertation is to fabricate Li-ion microbatteries composed of high aspect ratio, interdigitated electrodes via 3D printing. The second aim of my research is to expand these capabilities to fabricate fully 3D-printed LIBs composed of ultrathick semisolid biphasic electrodes. Finally, the third aim is to use these semisolid biphasic LIB electrodes in flow batteries, specifically in semisolid flow cells (SSFCs).[7]

Towards those objectives, the principle outcome of my dissertation is to develop electrode suspensions with tailored flow behavior and electrochemical performance for Li-ion batteries with high areal capacity. In one embodiment, two 3D-printable aqueous composed of $LiFePO_4$ (LFP, cathode) or $Li_4Ti_5O_{12}$ (LTO, anode) nanoparticles were created and sequentially printed in the form of 3D interdigitated electrode microarchitectures. We successfully fabricated high aspect ratio electrodes (width: 60 μm, height: 200 ~400 μm), which vastly exceed commercial thicknesses of 20 ~ 100 μm [8]. The energy and power densities of this 3D printed Li-ion microbattery are amongst the best values reported for microbatteries in the literature. To further enhance battery performance, we developed a new class of semisolid electrode inks based on biphasic mixtures of active LFP or LTO combined with electronically conductive carbon particles that are infused with electrolyte. We also developed printable UV-curable packaging and separator composite inks. Using a custom-designed environment-controlled 3D printer, LIBs were fabricated in arbitrary designs with ultrathick (1 mm) electrodes. As the first fully 3D-printed LIB, these packaged batteries deliver energy and power densities that are comparable to other high areal capacity batteries reported in the literature. Finally, we implemented these semisolid biphasic electrodes in flow batteries. Since the biphasic electrodes simultaneously possess high energy density, fast charge transport, and good flowability, they are ideally suited for semisolid flow cells. Specifically, we demonstrated a lab-scale flow battery with 1.5 mm thick electrodes with an energy density roughly five-fold higher than the state-of-the-art, all-vanadium flow batteries [9].

1.2 Dissertation Organization

In Chapter 2, the relevant literature is reviewed with an emphasis on Li-ion batteries, composed of LFP and LTO, 3D printing methods, biphasic suspensions, and flow batteries. In Chapter 3, 3D-printed interdigitated Li-ion microbattery electrode architectures are discussed, including electrode ink rheology, printing behavior, and battery electrochemical performance. In Chapter 4, fully 3D-printed Li-ion batteries are discussed, including biphasic electrode suspension design, flow behavior, and electrochemical performance along with separator and packaging inks. In Chapter 5, the use of biphasic electrode suspensions for semisolid flow cells is discussed, including suspension rheology, conductivity, and flow behavior as well as electrochemical properties. Finally, the conclusions of this dissertation are provided in Chapter 6.

Chapter 2

Literature Review

2.1 Introduction

Microscale devices, such as micro electromechanical systems (MEMS), [10] biomedical sensors, [11,12] wireless sensors, [13] and actuators [14], require rechargeable energy dense Li-ion batteries in customized form factors. While macroscale batteries are needed due to the growing adoption of renewable energy. Li-ion flow batteries offer a promising solution for grid scale storage, required to overcome the intermittency associated with solar and wind energy.[15,16] In this chapter, we review the field of LIBs. First, the key challenges and prior research efforts in creating high areal capacity Li-ion batteries will be described. Second, we will introduce $LiFePO_4$ (LFP, cathode) and $Li_4Ti_5O_{12}$ (LTO, anode) as the electrochemical couple of interest for my dissertation. Next, we will describe 3D printing technology and the design of colloidal inks. Finally, we will discuss recent efforts to use high-performance Li-ion semisolid electrodes in flow batteries for grid-scale applications.

2.2 Lithium Ion Batteries

Since SONY first commercialized the Li-ion technologies in 1991 [17] with a $LiCoO_2$ (LCO)/graphite electrochemical couple (**Figure 2.1**), significant advancements have led to continual improvements in their electrochemical performance, safety, and reliability. [2,18-26] In addition to new electrochemical materials, advances in separator and electrolyte research have also been reported. [27-30] Beyond materials, efforts have also focused on

transforming layered (current collector - electrode-separator - electrode - current collector) designs widely used in coin, cylindrical, prismatic, and pouch cell configurations [2] (Figure 1.2) to other motifs, including flexible and bendable wire-type batteries [31-33], stretchable and foldable batteries [34-37], and unique Li-ion flow batteries for grid-scale applications [7,38-40].

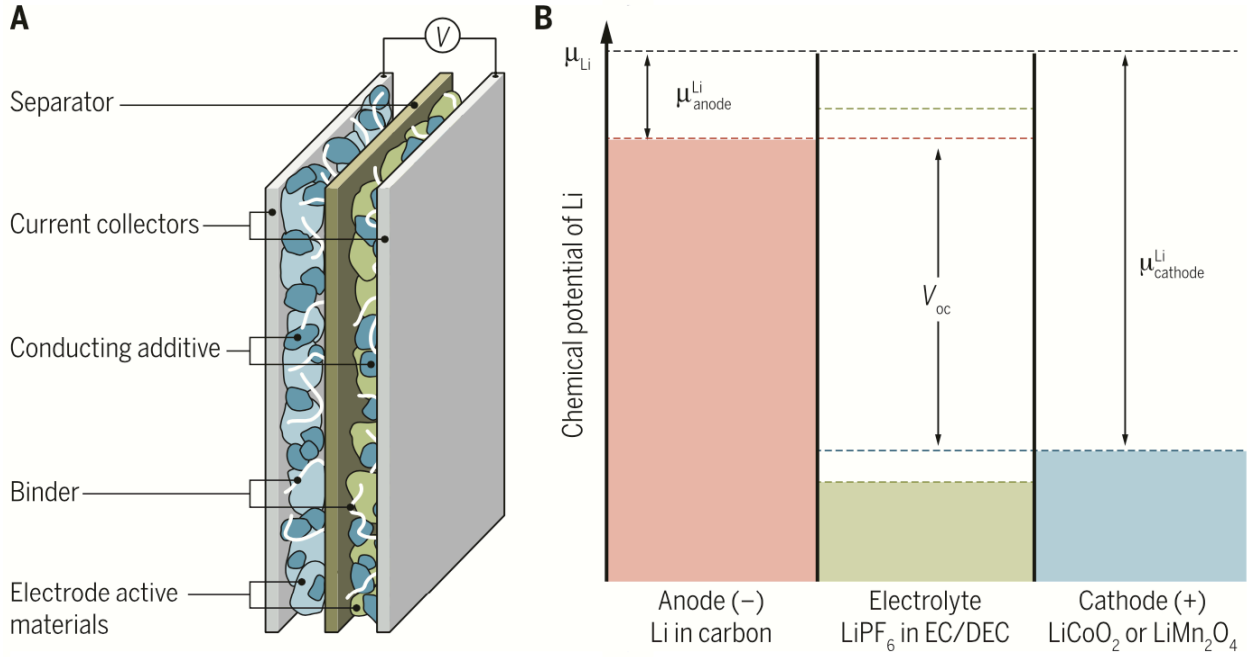

Figure 2.1: Schematic of a LCO/graphite Li-ion battery showing the energy levels involved. a) Architecture of a typical cell with composite electrodes. b) Illustration of the energy levels involved in a Li-ion electrochemical cell. The dashed red, blue, and green lines correspond to the chemical potential of Li in the negative electrode, the chemical potential of Li in the positive electrode, and a typical placement for the voltage window of the electrolyte, respectively. V_{oc}, open-circuit voltage of the cell; μ, chemical potential. Adapted from: [17]

2.2.1 Lithium Iron Phosphate/Lithium Titanium Oxide

Several issues associated with Li-ion batteries composed of LCO/graphite electrodes have led to the use of alternative materials, despite the high theoretical specific capacity (274 mAh g^{-1}), low self-discharge, high discharge voltage (3.8 V vs. Li/Li^+), and

good cyclability of LCO. The biggest disadvantages of using LCO are its high cost, low thermal and chemical stability, and fast capacity fade at high C-rates or deep cycling. [41] For example, the infamous LIB malfunction of Boeing 787 airplanes in 2013 resulted from thermal runaway. Deep cycling LCO also induces lattice distortion that deteriorates cycling performance, limiting the full utilization of their theoretical capacity. [41] Low-cost graphite anodes exhibit high lithium diffusivity, high electronic conductivity, and little volume change upon lithiation and delithiation. However, graphitic carbon suffers two major problems. First, it exfoliates in propylene carbonate (PC)-based electrolytes, which are widely used in LIBs. [41] Second, unstable SEI layer formation occurs and leads to poor cycle life. [41]

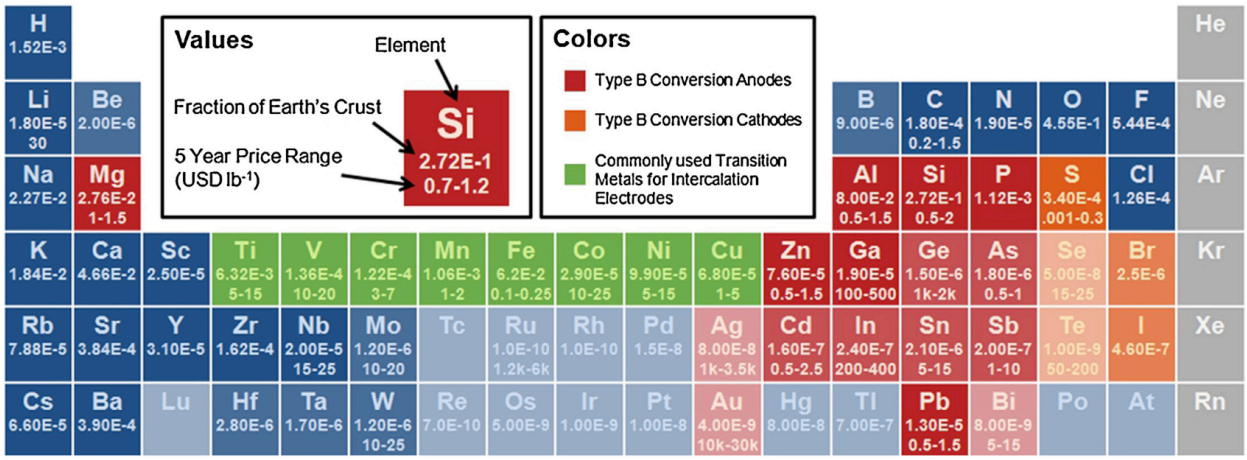

Figure 2.2: Availability of elements that may host Li as electrodes. Elements with abundance (as fraction of Earth's crust) below 10^{-5} are slightly faded, and elements below 10^{-7} are faded further. Prices are approximate 5-year ranges of metal prices (except Ge, which is a 3 year range). Gravimetric and volumetric capacities are theoretical values calculated based on delithiated mass and lithiated volume. Adapted from: [17]

In the search for better cathode materials, several candidates have been explored. For reference, **Figure 2.2** shows the availability and cost of elements suitable for Li-

based electrodes. [17] One alternative cathode material is $LiNiO_2$ (LNO), which has comparable energy density, but poorer thermal stability. [41] Partial substitution of LNO has improved its stability, leading to Panasonic's use of $LiNi_{0.8}Co_{0.15}Al_{0.05}O_2$ (NCA) for Tesla's electric vehicles. NCA has high usable discharge capacity (200 mAh g^{-1}), low self-discharge, but its capacity fades at modest temperatures (40~70 °C) is quite severe. [41] $LiMnO_2$ (LMO) has also been studied since manganese is far cheaper and less toxic than cobalt or nickel. [41] Unfortunately, LMO is chemically unstable (Mn dissolution), which leads to poor cycling performance. $LiNi_{0.33}Co_{0.33}Mn_{0.33}O_2$ (NMC, 3.7 V vs. Li/Li^+) is the most successful transition metal oxide cathode material developed to date, leveraging the ability to precisely control the level of cation substitution to achieve optimized capacity (Ni), voltage (Co), and safety (Mn). [41]

To further improve safety, another class of intercalation cathode material: olivine compounds with polyanions was recently developed, i.e., LFP. LFP is known for its superior thermal stability, high power capability, low volume change upon cycling (ε_{linear} = 2.2%) [42], and minimal cycling memory effect [43]. However, LFP also has slightly lower average potential (3.4 V vs. Li/Li^+), lower theoretical capacity (170 mAh g^{-1}), and lower intrinsic electrical and ionic conductivities. **Figure 2.3** nicely summarizes the pros and cons of several cathode materials and clearly show LFP's superior safety, lifetime and stability, recyclability, and low synthesis losses. [44-46] To realize the potential of high power LFP batteries, researchers have used LFP nanoparticles [41,44,46] coated with carbon to improve their conductivity, leading to improved rate capability (**Figure 2.4**). [47-51].

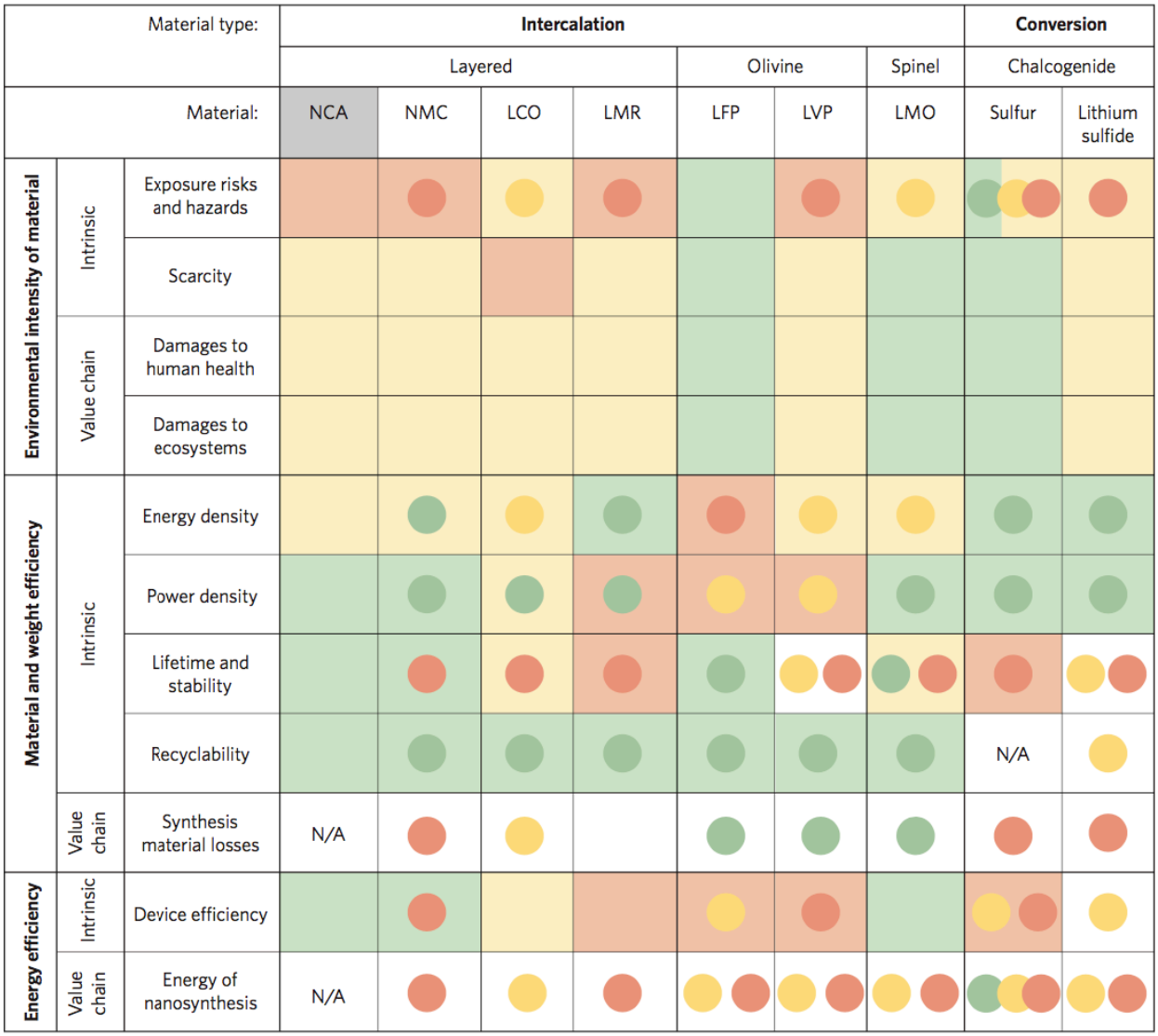

Figure 2.3: Common cathode materials for Li-ion batteries. Nanoarchitectured materials are given by a circle. Background colors reflect characteristics of bulk materials. Green denotes relative strength, red relative weakness, yellow intermediate characteristics and white no data. Absence of circle indicates no data for the nanomaterial. The grey background denotes the 'baseline' material. NCA, lithium nickel cobalt aluminum oxide; NMC, lithium nickel manganese cobalt oxide; LCO, lithium cobalt oxide; LMR, lithium/manganese rich transition metal oxide; LFP, lithium iron phosphate; LVP, lithium vanadyl phosphate; LMO, lithium manganese oxide. Adapted from: [44]

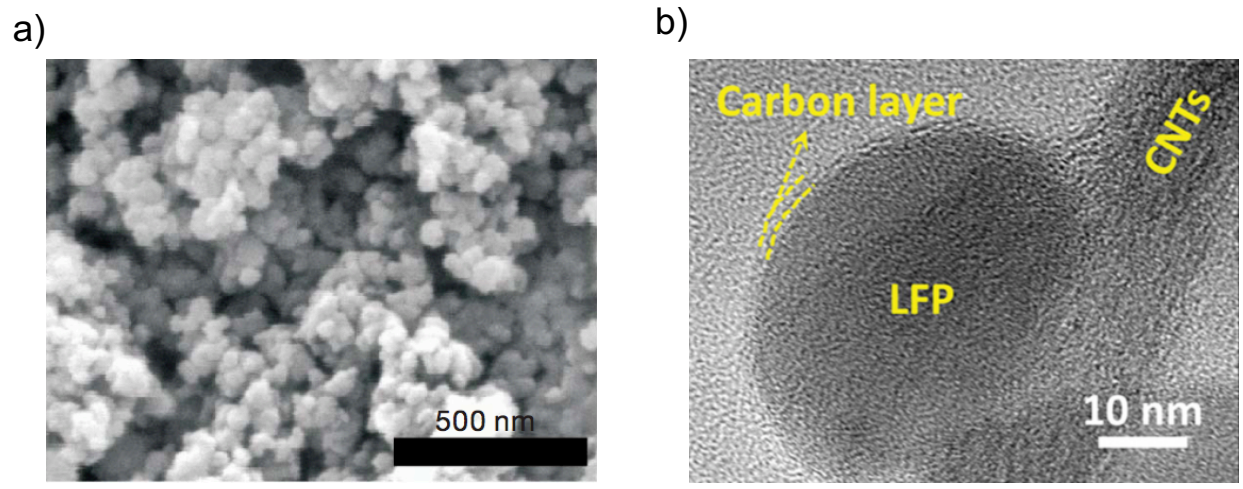

Figure 2.4: Effective methods to improve cycling performance of LFP, towards high power Li-ion battery. a) Nano-sized LFP particles. Adapted from: [46] b) Carbon-coated LFP particles. Adapted from: [47]

Researchers have also explored alternative anode materials to overcome the exfoliation and unstable SEI issues associated with graphite anodes. Lithium metal is often referred to as the "Holy Grail" due to its high theoretical capacity (3860 mAh g^{-1}), low density (0.59 g cc^{-1}), and the lowest negative electrochemical potential (-3.040 V) versus standard hydrogen electrode (SHE). However, Li dendrite growth and low Coulombic efficiency have limited its application. [52] Hard carbon, which is composed of small graphitic grains with disordered orientation, is also of interest, since it is less susceptible to exfoliation and the nanovoids between grains provide excess capacity (372 mAh g^{-1}). [41] However, hard carbons exhibit poor coulombic efficiency, and are therefore unsuitable for practical use.

Similar to LFP cathodes the intercalation anode LTO has been successfully commercialized due to its high thermal stability, high rate, zero strain intercalation mechanism (ε_{linear} = 0.07%) [53], minimal cycling memory, long cycle life, efficient hydrothermal synthesis [44], and relatively high volumetric capacity (600 mAh cm^{-3}). [41,54]

LTO does have its disadvantages, namely, the relatively low capacity (175 mAh g^{-1}), higher cost of Ti than C (Figure 2.2), the reduced cell voltage (1.55 V vs. Li/Li^+). [41,55] The higher equilibrium potential (>1 V) and minimal volume change allow LTO to form extremely stable SEI, which extends battery life and improves efficiency. LTO is also very safe, with no Li dendrite formation, even at high cycling rates. [41] With the use of nano-sized LTO particles (**Figure 2.5a**), high-rate LIBs can be prepared, despite LTO's low intrinsic Li and electronic conductivity. [41,54,56,57] To further improve battery life, carbon-coated LTO (**Figure 2.5b**) is often used to suppress gassing due to unwanted reaction between the electrolyte and the LTO particles. [41,58,59] In my dissertation, we chose to use LFP and LTO electrodes to create Li-ion batteries with good performance and safety. **Figure 2.6** shows the typical charge and discharge curves of a LFP/LTO full cell, a LFP/Li half-cell, and a LTO/Li half-cell. The LFP/LTO full cell have an equilibrium discharge potential of 1.85 V (3.4 V – 1.55 V) and a theoretical discharge capacity of 170 mAh g^{-1}.

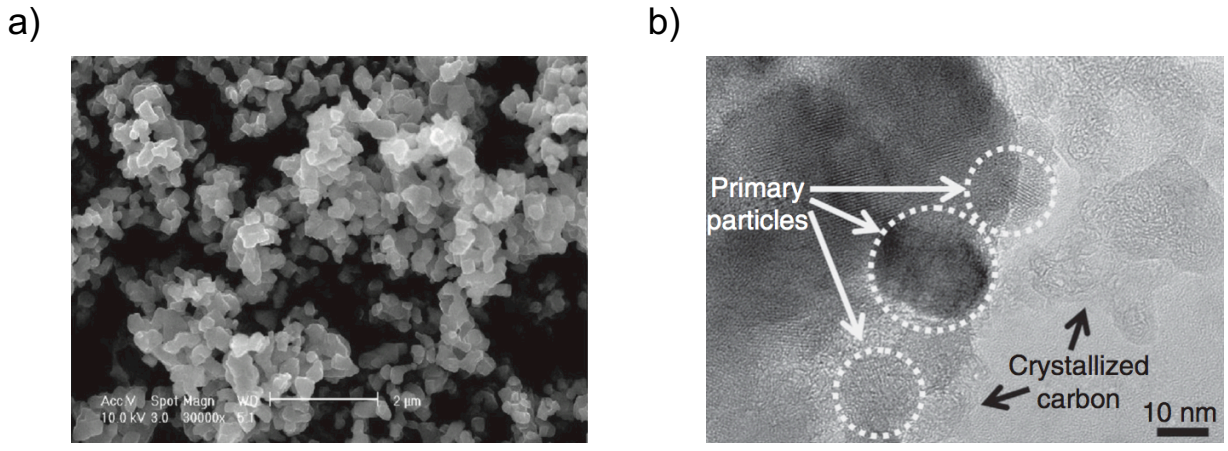

Figure 2.5: Effective methods to improve cycling performance of LTO, towards high power Li-ion battery. a) Nano-sized LTO particles. Adapted from: [54] b) Carbon-coated LTO particles. Adapted from: [58]

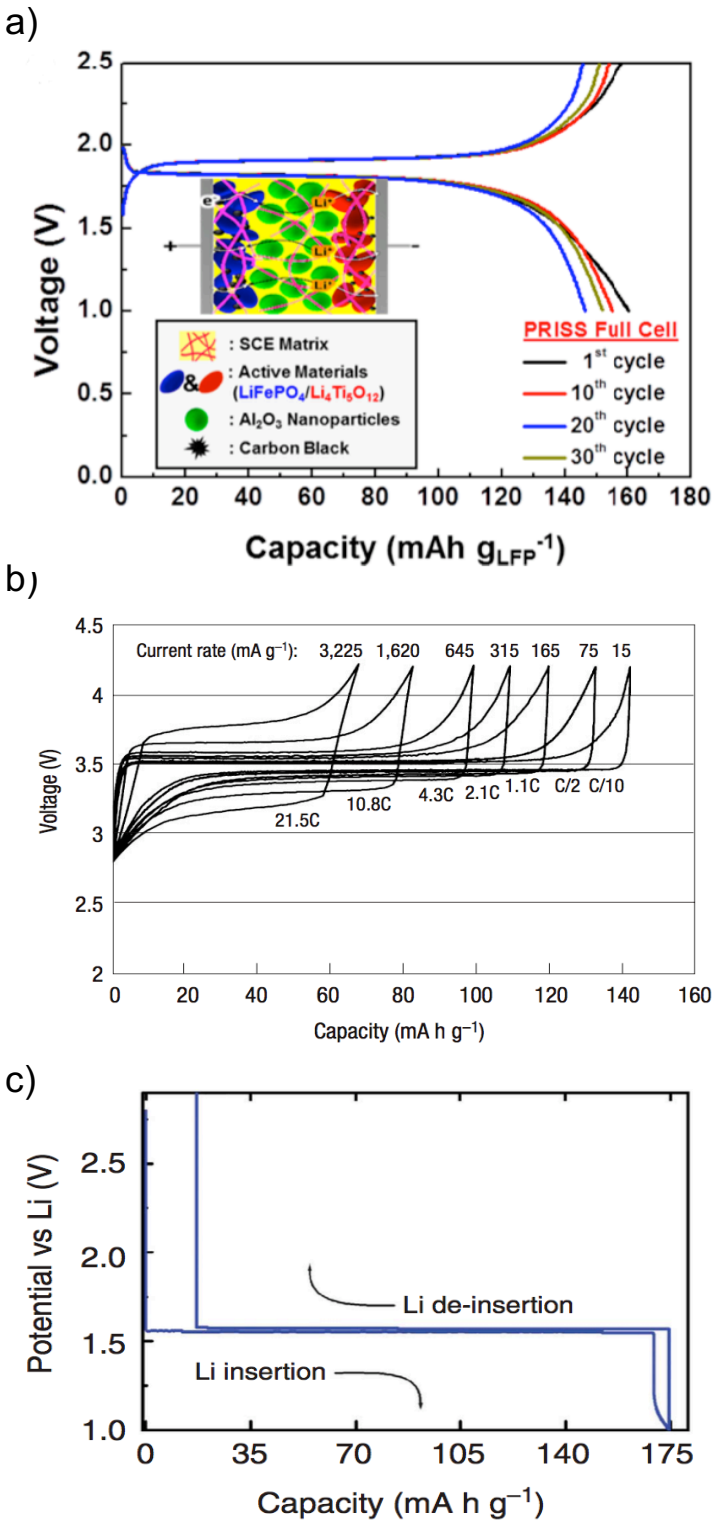

Figure 2.6: Typical charge and discharge curves of a) LFP/LTO full cell (adapted from: [60]), b) LFP/Li half cell (adapted from: [45]), and c) LTO/Li half cell (adapted from: [58]).

2.2.2 Thick Electrode Li-ion Batteries

One can vastly improve the areal capacity of LIBs by increasing the electrode thickness. However, several challenges are often encountered, including delamination [61] and cracking [35,62-64] (**Figure 2.11**). The critical cracking thickness (h_{max}) of particulate-based LIB electrode layers is given by [65]:

$$h_{max} = 0.64 \left[\frac{GM\phi_{rcp}R^3}{2\gamma}\right]^{1/2} \left[\frac{2\gamma}{(-P_{max})R}\right]^{3/2} \quad \textbf{(Equation: 2.1)}$$

where G is the shear modulus of the particles, M is the coordination number, ϕ_{rcp} is the particle volume fraction at random close packing, R is the particle radius, γ is the solvent-air interfacial tension, and P_{max} is the maximum capillary pressure beyond which the liquid menisci recede into the porous film, limiting the deformation of the film. [65] When a thin film of colloidal suspension dried on a substrate, particles consolidate into closed packed array as solvent evaporates. Upon further drying, capillary stresses develop as the liquid menisci form. [65,66] To minimize cracking and delamination, one can increase the adhesion between particles, control drying by increasing humidity or using supercritical drying methods, or modifying substrate properties to provide a slip-inducing interface between the film and substrate. [62]

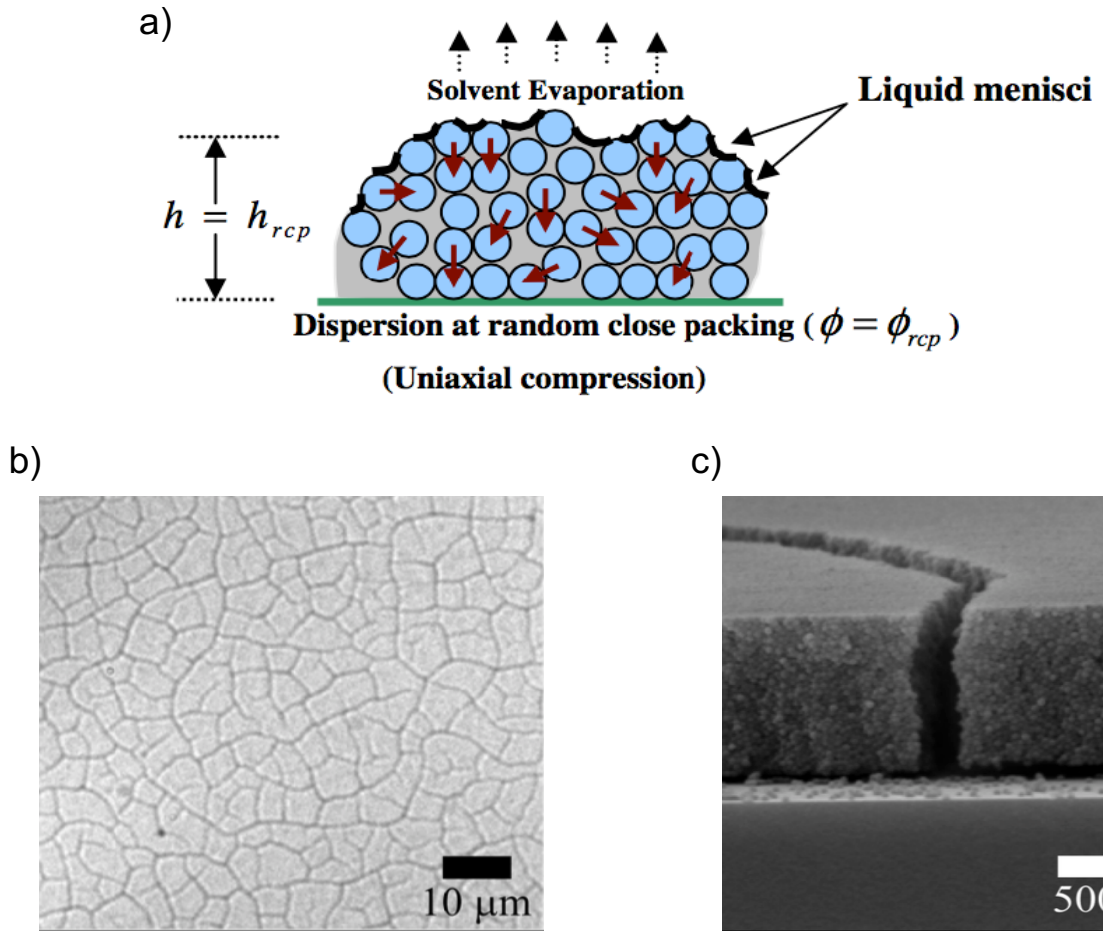

Figure 2.11: (a) Schematic showing compression force formation of a colloidal thin film, as a result of solvent evaporation and condensed particle packing. Adapted from: [65] (b) Interconnected crack network formed in a ~500 nm thin film of 22.5% silica due to drying. (c) Zoomed-in view of the (b). Adapted from: [67]

Thick LIB electrodes also exhibit poor power density, largely due to their poor ionic and electronic conductivity. [68-70] **Figure 2.12** shows inhomogeneous state of charge (SOC) and depth of discharge (DOD) at the anode and cathode, respectively, and lowered specific capacity of a NCM ($LiNi_{1/3}Co_{1/3}Mn_{1/3}O_2$) electrode with increasing electrode thickness, which led to specific energy of thicker electrodes to drop much faster as power increases (faster discharge rate). [68] However, Hasan et. al. showed that when the

electrode porosity is high, there is ample electrolyte surrounding active particles, which prevents local depletion of Li. [71]

As electrode thickness increases, the internal resistance in electronic transport also increases, causing shortened cycle life (worsened capacity retention) due to increased voltage polarization, uneven heat distribution, and inhomogeneity in SOC or DOD (**Figure 2.13**). Improving electronic conductivity by engineering efficient conductive pathway throughout the electrodes is an effective way to reduce internal resistance and voltage polarization. Because ohmic heat is more serious for high current applications, batteries with thicker electrodes are best suited for low-power applications, with high energy, intermittent discharge cycles, and infrequent recharge cycles.

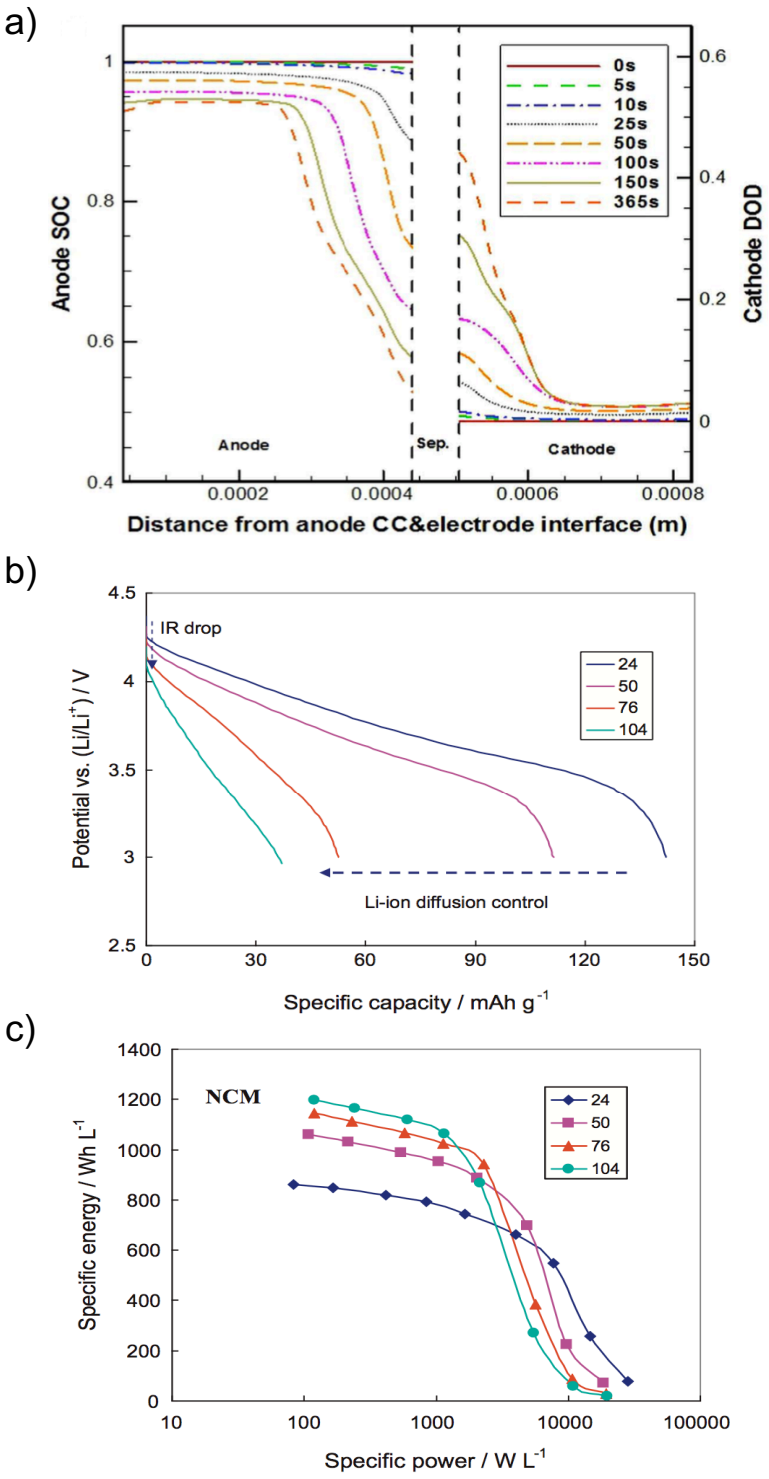

Figure 2.12: a) Time-variation of SOC in anode and DOD in cathode showing inhomogeneity as a result of slow ion diffusion in thick electrodes. Adapted from: [69] b) Comparison of discharge curves for the NCM electrode at the same current density of 5C. Adapted from: [68] c) Ragone plot for the NCM cathodes at different electrode thicknesses. Adapted from: [68]

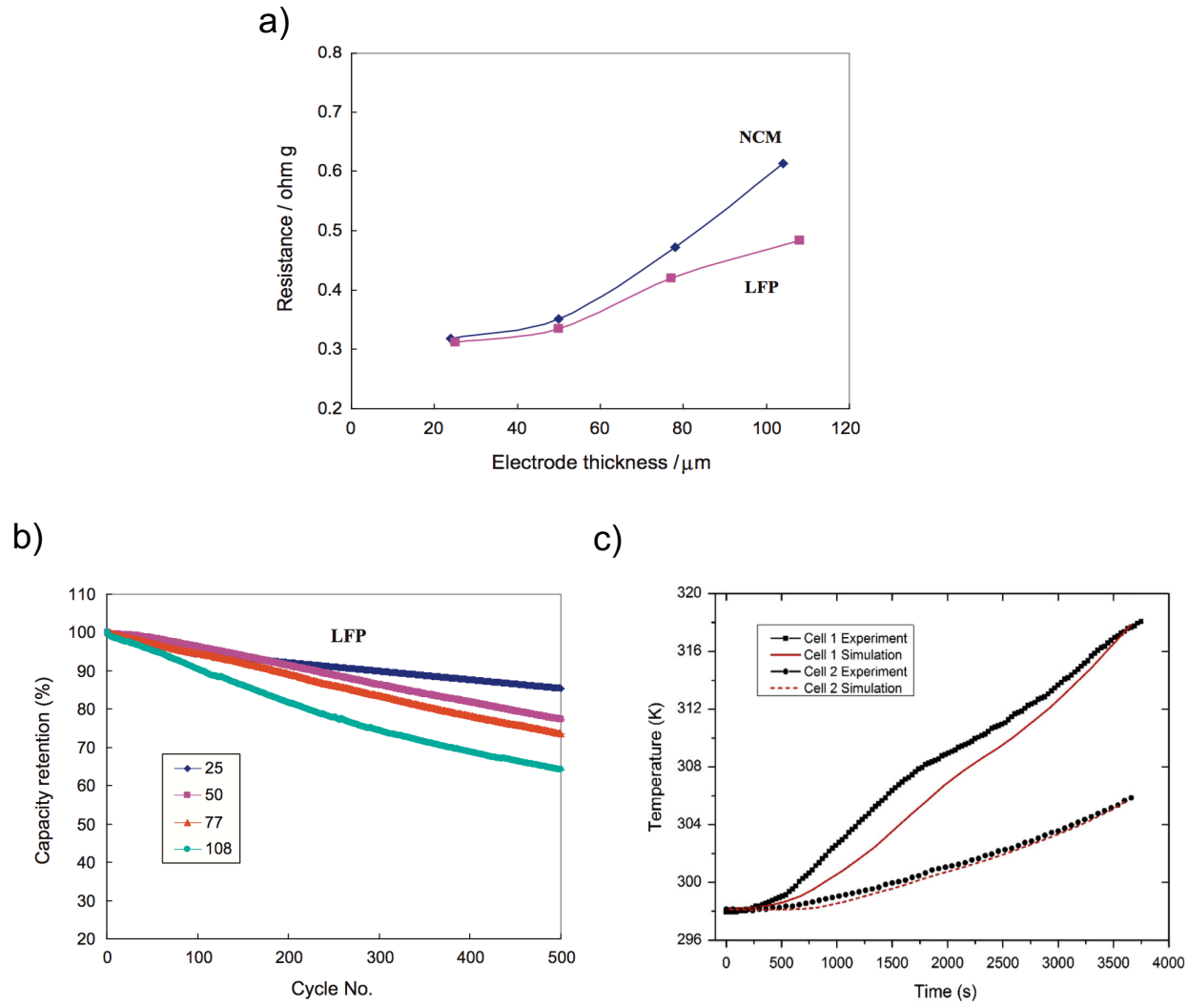

Figure 2.13: a) Increasing weight specific impedance of NCM and LFP electrodes with increasing electrode thickness. Adapted from: [68] b) Worsened capacity retention of with increasing electrode thickness of LFP cathodes. Adapted from: [68] c) Temperature curves of cell 1 (thick electrodes) and cell 2 (thin electrodes) acquired from experiments and simulations under 1C discharge rate. Adapted from: [70]

Finally, thick electrodes often suffer from incomplete electrolyte infiltration, forming inactive regions that lower capacity utilization and thus energy density. [72] This is due to the poor wettability of the tortuous electrode porosity with deep penetration distance, which can be improved by increasing porosity and surface chemistry of the particle surface to promote wetting. [72] During the drying process, microstructural inhomogeneity

may arise due to differences in local particle rearrangement or binder migration (**Figure 2.14**). [61,73,74] Such phenomena also lead to shortened battery life due to variation in SOC and DOD, and inferior mechanical stability especially for active materials with large volume change upon lithiation and delithiation. Methods to improve microstructural homogeneity include decreasing solids content and using high molecular weight polymeric binder with lower mobility.

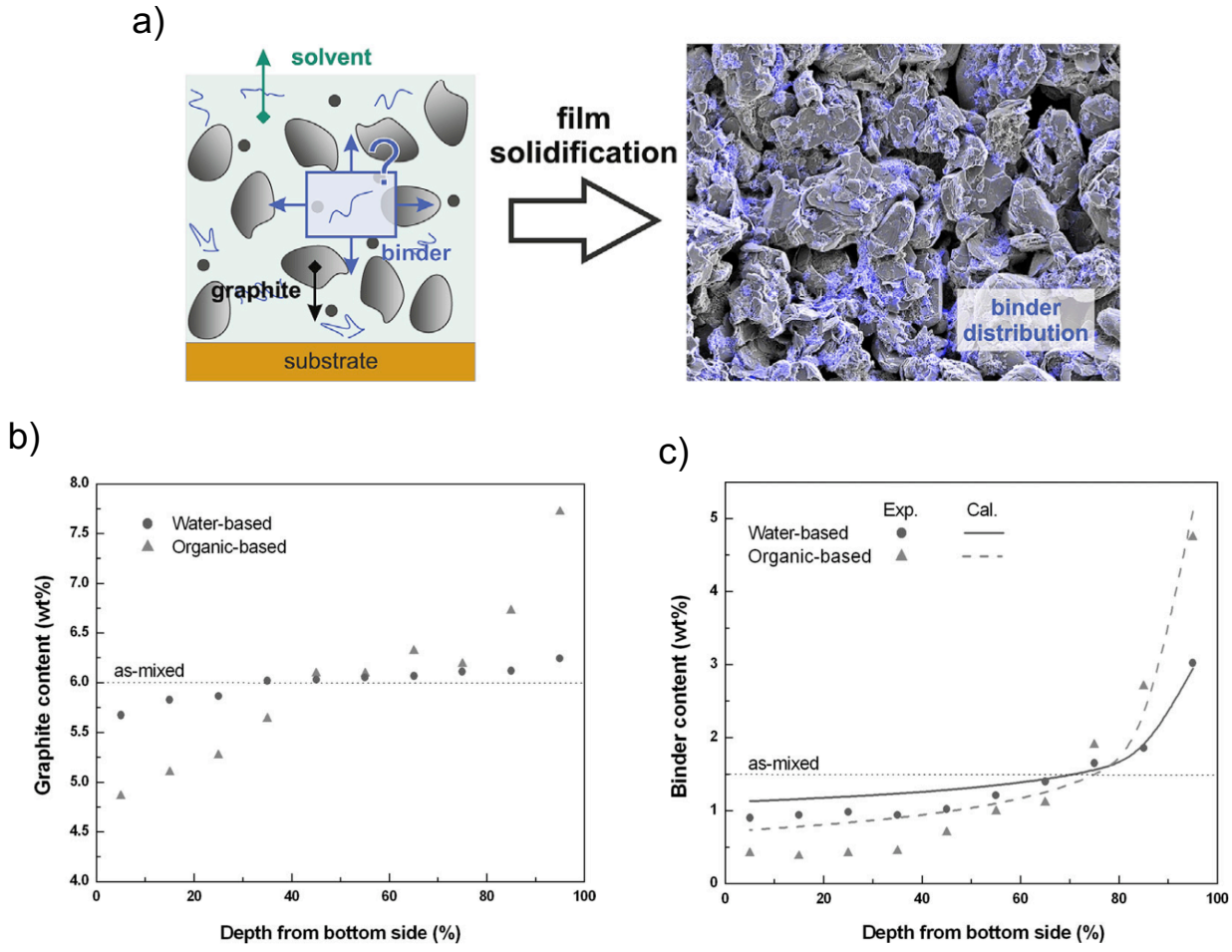

Figure 2.14: a) Schematic and SEM image showing inhomogeneous graphite rearrangement and binder migration of as solvent evaporates during drying. Adapted from: [61] b) Inhomogeneity of graphite particles in dried $LiCoO_2$ electrode sheets (1500 µm thick), deviating from the as-mixed (dotted-line) uniform graphite distribution. Adapted from: [74] c) Inhomogeneity of binder distribution in dried $LiCoO_2$ electrode sheets (1500 µm thick), deviating from the as-mixed (dotted-line) uniform binder distribution. Adapted from: [74]

Owing to those challenges, commercial electrode thicknesses are typically 20 μm to 100 μm [8], which greatly lowers the ratio of active/inactive materials, and hence leads to low energy density. However, several strategies have been introduced for creating high areal capacity LIBs using thick electrodes. [8,20,35,75,76] **Figure 2.15** shows a mechanically robust thick Li_2S cathode electrode made by stacking multiple layers of free-standing flexible electrode sheets to prevent cracking and delamination. [35] Their free-standing flexible electrode is prepared by carbonizing low-cost cellulose-based porous polymer sheets into conductive 3D porous carbon sheets, followed by infiltrating active sulfur particles into the pores. [35] Areal capacity is increased simply by increasing the number of layers of the free-standing flexible electrodes. Stacked multi-layer electrodes [35,62] are effective in avoiding cracks and delamination, but still suffer from the other problems described previously.

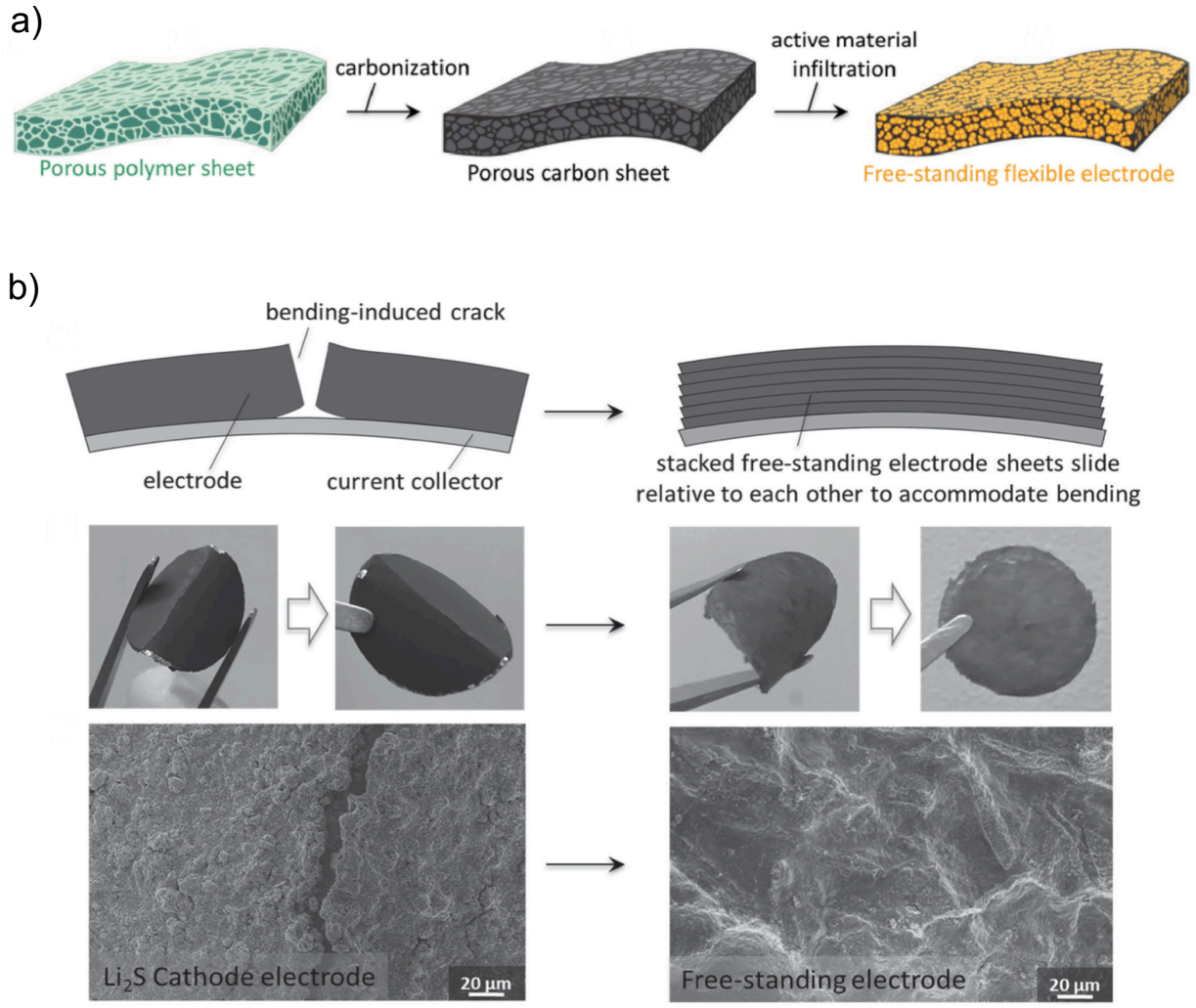

Figure 2.15: a) The fabrication process of the free-standing flexible electrode of conductive porous carbon sheet infiltrated with active sulfur. Adapted from: [35] b) Mechanical flexibility comparison of a conventionally produced thick electrode (left panel) vs. an electrode produced by stacking thin free-standing electrode sheets (right panel) showing no cracks or delamination forming for the stacked electrodes. Adapted from: [35]

Increasing the electronic conductivity of thicker electrodes is an effective way to reduce their internal resistance. One popular method is to replace traditional conductive particles with thick conductive 3D porous current collectors, as shown in **Figure 2.16a**. [8,77,78]

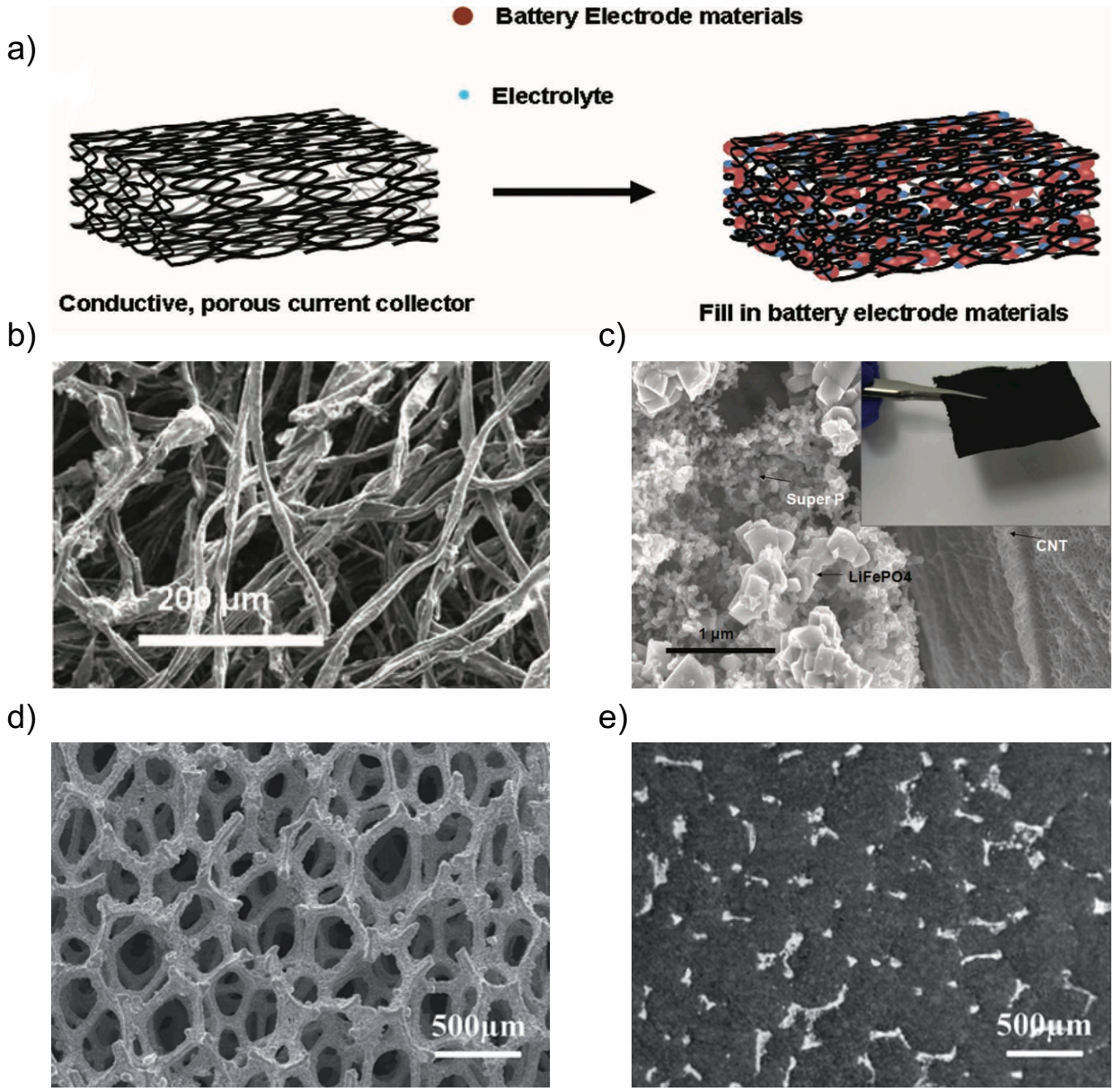

Figure 2.16: a) Schematic of 3D porous current collectors filled with battery electrode materials. Adapted from: [77] b) SEM image of a 3D porous conductive CNT textile as a current collector. Adapted from: [77] c) SEM shows the interface between $LiFePO_4$, conductive additive Super-P, and conductive 3D porous CNT current collector. Adapted from: [77] d) SEM image of a 3D porous conductive Ni metal foam as a current collector. Adapted from: [8] e) SEM image of LFP-filled 3D porous conductive Ni metal foam as a cathode. Adapted from: [8]

By utilizing a 3D porous conductive carbon nanotube (CNT) textile as current collectors,

Hu et. al. created 600 µm (areal loading = 170 mg cm^{-2}) LFP cathodes delivering areal

capacities as high as 23.2 mAh cm^{-2} at 2.3 mA cm^{-2} (**Figure 2.16b,c**). [77] Similarly, Yang et al. also created high performance LFP cathodes as thick as ~0.6 mm (areal loading = 56.3 mg cm^{-2}) by using 3D porous metal foam current collectors. These LIBs delivered a high areal capacity of 8.8 mAh cm^{-2} at 1 mA cm^{-2} (**Figure 2.16d,e**). [8] The use of conductive 3D porous current collector has been shown to effectively improve electronic conductivity and thus cycling performance, however, the infiltration of active materials often requires several coating sequences and inhomogeneous electrolyte wetting remains an issue. [72]

To improve their ionic conductivity, Shen et. al. created anisotropic, conductive 3D carbon current anodes for sodium ion batteries (SIBs) and LIBs capable of reaching areal capacity of 13.6 mAh cm^{-2} at 0.55 mA cm^{-2} with a 850 μm thick (55 mg cm^{-2}) anode (**Figure 2.17**). [20] The mesoporous carbon anodes are binder-free, current collector-free, have low-tortuosity to improve ionic conductivity, and are created inexpensively by directly carbonizing wood. [20] The unique mesoporous and large straight channels contributed greatly to the high ionic conductivity while the carbon walls provided an efficient electronic conductive pathway. [20] This is a promising technique as it bypasses all of the thick electrode problems discussed in the previous section. Carbon, however, has poor cycling stability, as described earlier.

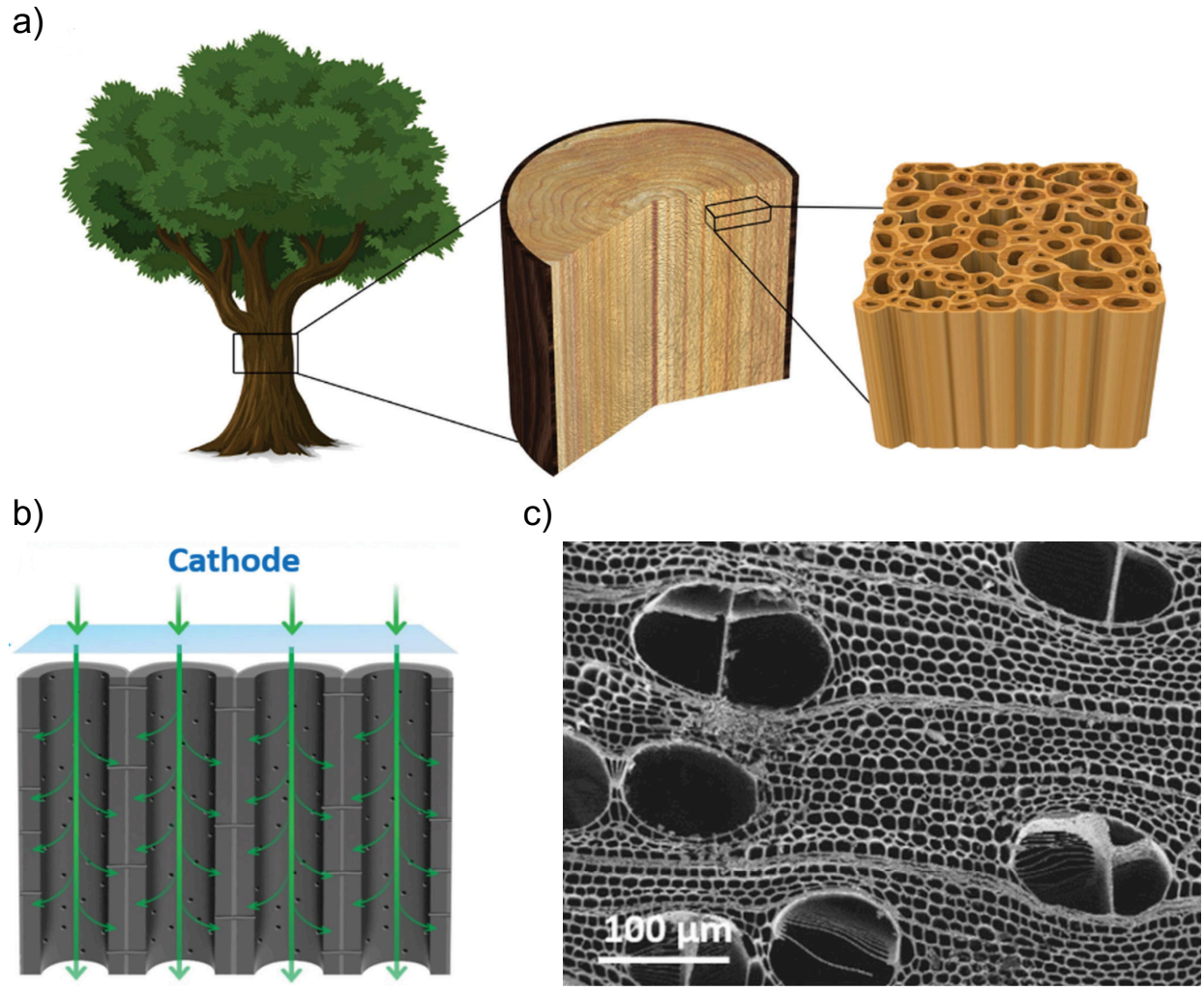

Figure 2.17: a) Schematic to show the unique anisotropic natural wood with well-defined channels along the tree growth direction. Adapted from: [20] b) Schematic showing ion transporting from the cathode across the separator then into the anode structure through the mesoporous structure with straight channels. The low tortuosity along the channel direction allows fast ion transport. Adapted from: [20] c) Top-viewed SEM image of a wood slab after carbonization showing the directional channels. Adapted from: [20]

Another strategy to increase active material packing is to pattern and sinter electrodes.[75,76] Sander et al. recently achieved an areal capacity ~12 mAh cm^{-2} at 0.64 mA cm^{-2} with a sintered, 310 µm thick LCO cathode (**Figure 2.18a,b**) that contains

directional pore channels to facilitate ion transport. [75] The aligned pore channels were created by magnetically aligning sacrificial microrods or emulsion droplets that are removed during the drying and sintering process. However, the sintered LCO electrodes have porosities ~ 40%, [75] which are still quite high. The use of sintered electrodes is also reported demonstrated by Lai et. al. (**Figure 2.18c**), where thick sintered electrodes (0.8 mm) as dense as 87% were prepared, delivering an impressive 49 mAh cm^{-2}, albeit at low (C/50) rates. [76] Sintered electrodes are certainly effective in increasing areal capacity, however ionic and electronic transport becomes even more challenging as the pore content decreases.

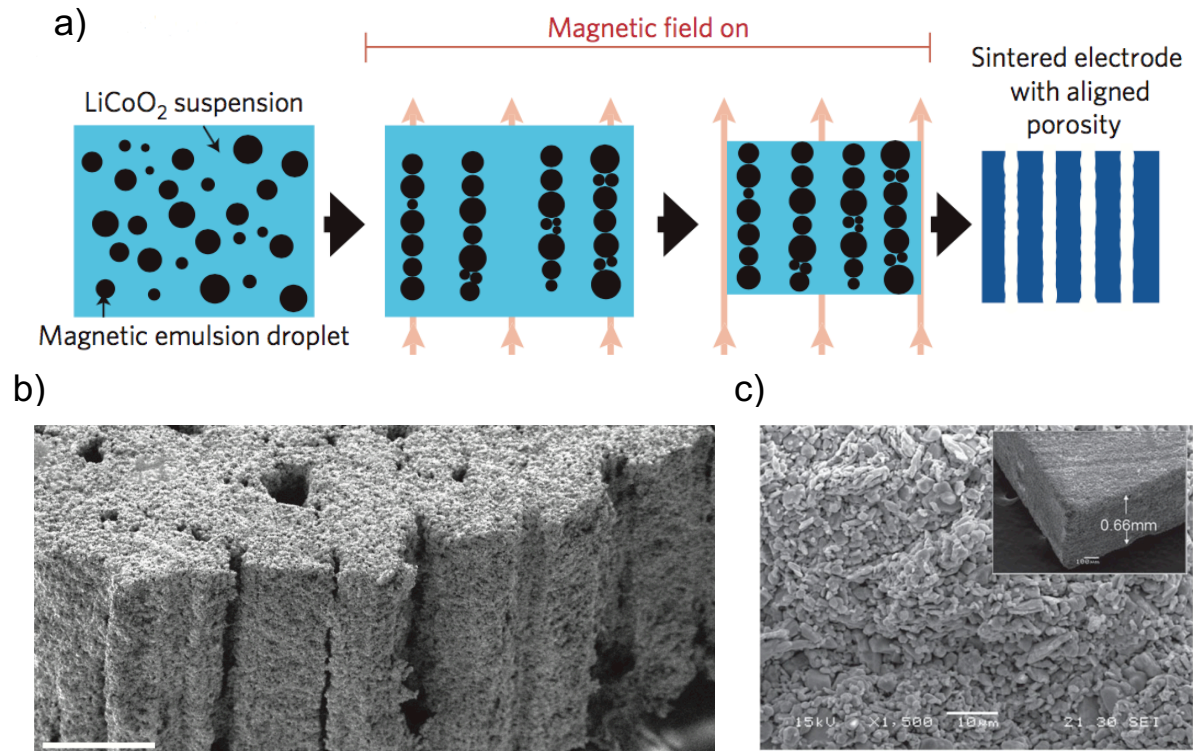

Figure 2.18: a) Electrode fabrication using magnetic alignment of sacrificial emulsion droplets. The droplets are mixed with a suspension of electrode-active particles and aligned with an external magnetic field. The red arrows indicate the direction of the magnetic field. Adapted from: [75] b) Cross-section of a sintered $LiCoO_2$ electrode with aligned pore channels templated by magnetically chained emulsions (scale bar = 100 µm). Adapted from: [75] c) SEM image of a 660 µm thick, sintered monolithic cathode (inset)

and cross section of a fracture surface from a 74% dense sintered cathode (scale bar = 10 μm). Adapted from: [76]

In this dissertation, we use direct ink writing (DIW), an extrusion-based 3DP technique to create LIBs with structured, thick electrodes. In the following section, we discuss the basics of this 3D printing process.

2.3 Direct ink writing Li-ion Batteries with Thick Electrodes

3D printing transforms computer-aided designs (CAD) into physical 3D objects, without the need for expensive molds, dies, or lithographic masks. [79] It enables a wide range of objects to be rapidly fabricated with customizable designs and minimal material waste (**Figure 2.19a,b**). [80] Direct ink writing (DIW) uses a computer-controlled robotic building platform to deposit inks in a layer-by-layer manner (Figure 2.19c). [80] Since DIW is an extrusion-based 3DP method, it has the ability to print a wide range of materials compared to other 3DP techniques. [80] To date, DIW has been used to create metallic electrodes [81-88], bio-inspired composites [89-93], optical architectures [94-96], soft robots [79,84,97], and even vascularized human tissues [98-103]. Pivotal to DIW's success is the development of functional inks, whose rheological properties are optimized for DIW. [79]

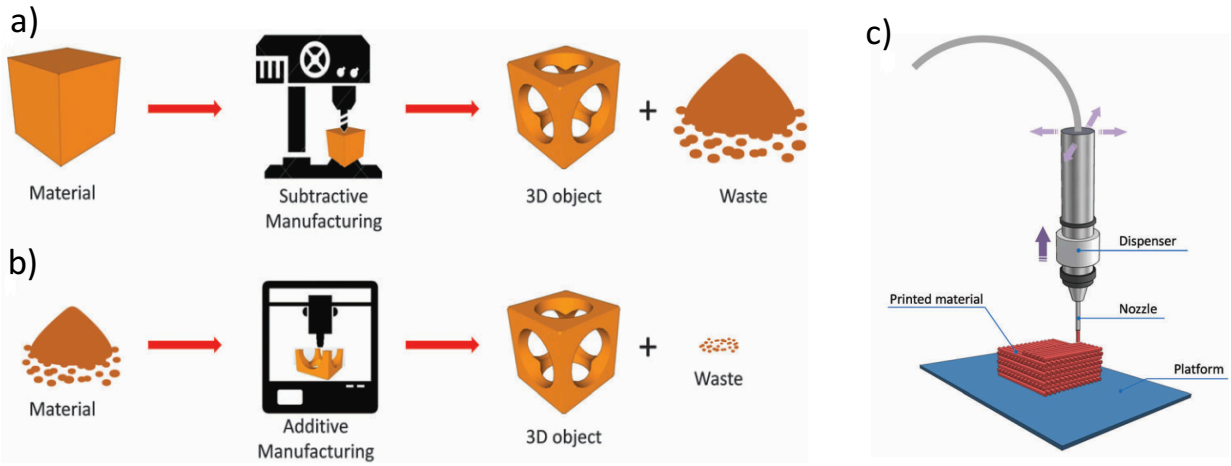

Figure 2.19: Additive vs. subtractive manufacturing. a) In subtractive manufacturing, a block of material is processed by material-removing machines with a large amount of residual material. Adapted from: [80] b) In additive manufacturing, a starting material is processed by a 3D-printing machine, which deposits just the required amount of material in a layer-by- layer fashion, with minimal residual material. Adapted from: [80] c) A schematic of direct ink writing with a material dispenser connected to a computer-controlled robotic building platform, depositing the ink material in a layer-by-layer manner. Adapted from: [80]

To create high areal capacity LIBs via DIW, thick electrodes must be printed. The electrode inks should contain a high loading of active material as well as provide electronic and ionic transport pathways for efficient electrochemical reactions. My Ph.D. research focuses on meeting these objectives to enable 3DP of high-performance LIBs in customized form factors.

Colloidal inks developed for DIW must exhibit both shear thinning and yield-stress behaviors (**Figure 2.20**). [104] Shear thinning behavior enables these inks to flow readily through fine nozzles during the printing process, while yield-stress behavior enables the ink to rapidly (re)solidify upon exiting the nozzle to retain its filamentary form. When the applied shear stress (τ) exceeds the yield stress (τ_y), the ink yields into a liquid-like ($G'' > G'$), flowable state, to enable ink deposition. Once the ink exits the printhead and the shear stress returns to zero, it returns to a solid-like ($G' > G''$), rigid state. Shape retention of the printed 3D structure relies on this rapid dynamic recovery of shear elastic modulus.[105]

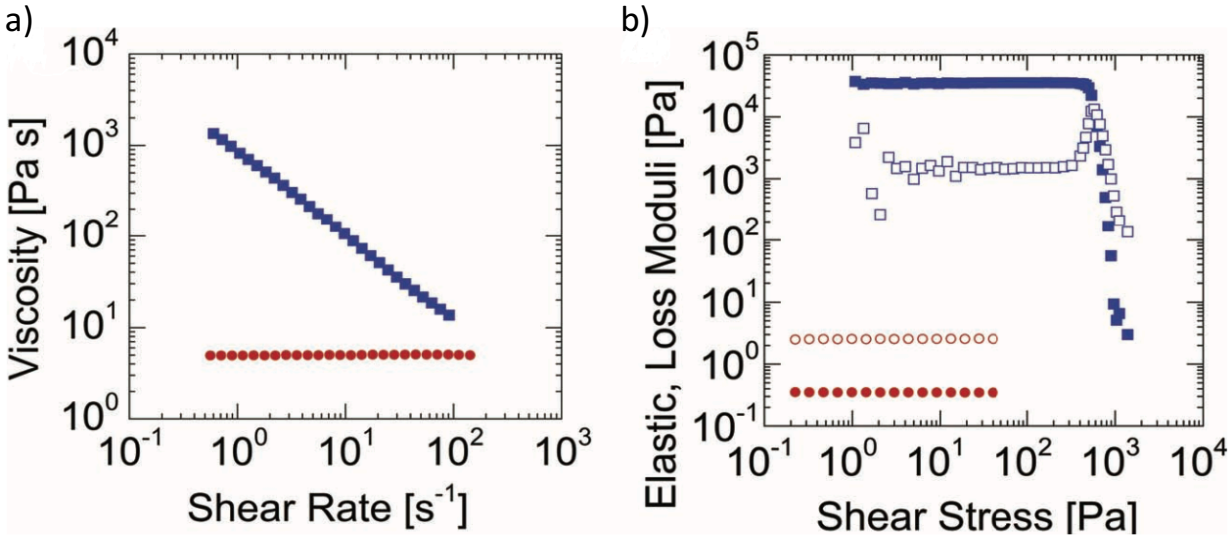

Figure 2.20: Shear thinning and viscoelasticity. a) Log–log plot of viscosity as a function of shear rate; b) log–log plot of shear elastic (filled symbols) and loss (open symbols) moduli as a function of shear stress for a non-3D printable ink (red, Ormo-Clear) and a 3D printable ink (blue, aqueous Pluronic F127). Adapted from: [96]

More specifically, a viscoelastic ink flows through the deposition nozzle when the shear stress (τ) at the nozzle wall developed by the pressure drop ΔP exceeds the yield stress (τ_y)[105]:

$$\tau_r = \frac{r\Delta P}{2l} \quad \textbf{(Equation 2.2)}$$

where r is the radial position ($r = R$ at the nozzle wall) and l is the length of the nozzle. Once the ink is yielded ($\tau > \tau_y$), many DIW inks exhibit shear thinning behavior that can be described by the Herschel Bulkley equation[105]:

$$\tau = \tau_y + K\dot{\gamma}^n \quad \textbf{(Equation 2.3)}$$

where n is the shear thinning exponent (<1), K is the viscosity parameter, and $\dot{\gamma}$ is the shear rate.

Concentrated colloidal inks with suitable rheological properties are especially relevant for 3D printed LIBs, since it is desirable to have high loading of active materials to maximize energy density and areal capacity. Unfortunately, as one increases the solids loading, the suspension viscosity increases, as described by the Krieger-Dougherty model:

$$\eta_{rel} = \left(1 - \frac{\phi}{\phi_{max}}\right)^{-K\phi_{max}} \quad \textbf{(Equation 2.4)}$$

where η_{rel} is the relative viscosity, which is equal to apparent viscosity divided by solution viscosity (η/η_o), ϕ is the volume fraction of colloidal particles in suspension, ϕ_{max} is the maximum volume fraction of colloidal particles in suspension (ϕ_{max} =0.6~0.64 for monomodal systems), and K = 2.5 for monodisperse spheres. [105] As ϕ approaches ϕ_{max}, η_{rel} increases dramatically, greatly reducing flowability.

To achieve good flowability at high solids content, concentrated colloidal suspensions must be prepared in the dispersed state. One must therefore control interparticle forces to introduce a significant repulsive barrier >> k_bT (between colloidal particles) (**Figure 2.21**). [105]

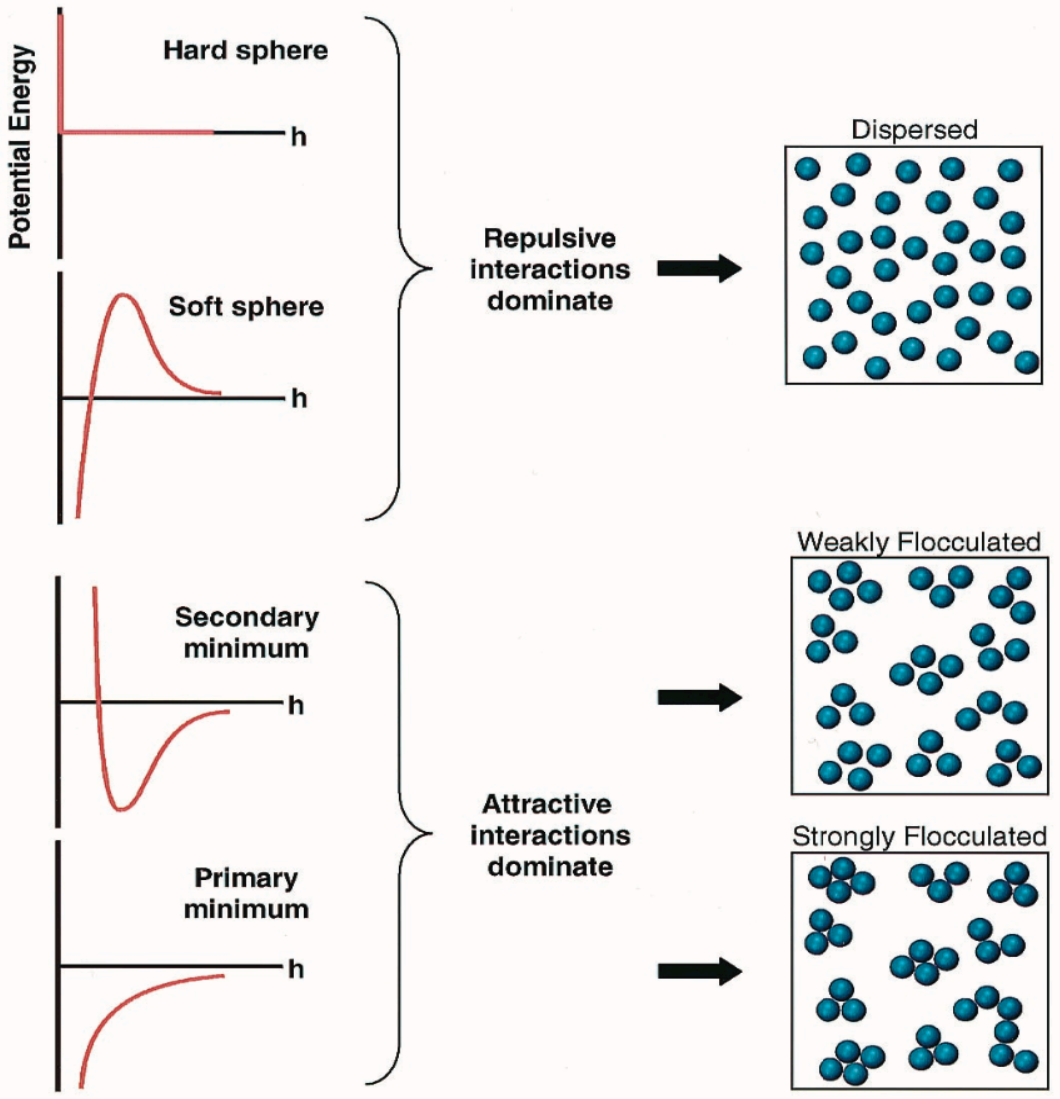

Figure 2.21: Schematic illustration of the relationship between the total interparticle potential energy and the resulting suspension structure. Adapted from: [105]

The total interparticle potential energy, V_{total}:

$$V_{total} = V_{vdW} + V_{elect} + V_{steric} \qquad \textbf{(Equation 2.5)}$$

where V_{vdW} is the attractive potential energy resulting from the long-range van der Waals interactions between particles, V_{elect} is the repulsive potential energy resulting from the electrostatic interactions between like-charged particle surfaces, and V_{steric} is the repulsive potential energy resulting from steric interactions between particle surfaces coated with polymeric species. The first two terms, V_{vdW} and V_{elect}, constitute the well-known DLVO theory developed by Derjaguin, Landau, Verwey, and Overbeek. [105] Since V_{vdw} is always negative (attractive), stable suspensions can only be formed when the repulsive interparticle potential energies (V_{elec}, V_{steric}) are high enough to overcome the particle's tendency to flocculate. (**Figure 2.22**)

Electrostatically stabilized colloidal suspensions are kinetically stable, relying on the repulsive surface potential induced on the interacting colloidal particles and the dielectric properties of the intervening medium. [105] However, it may be difficult to effectively design stable suspensions based solely on electrostatic stabilization in practice since the suitable pH or range or ionic strength are often narrowly limited. The effect on high ionic strength is especially of interest for Li-ion batteries as the electrolyte used often have high ionic strength ($\geq$ 1 M), forcing the Debye-Hückel screening length ($1/\kappa$) to shorten due to charge screening. [105] κ is described as:

$$\kappa = \left(\frac{F^2 \sum_i N_i Z_i^2}{\varepsilon_r \varepsilon_0 kT}\right)^{1/2} \qquad \textbf{(Equation 2.6)}$$

where F is the Faraday constant, N_i and Z_i are the number density and valence of the counterions of type i, ε_r is the dielectric constant of the solvent, ε_o is the permittivity of vacuum, k is the Boltzmann constant, and T is temperature in Kelvin.

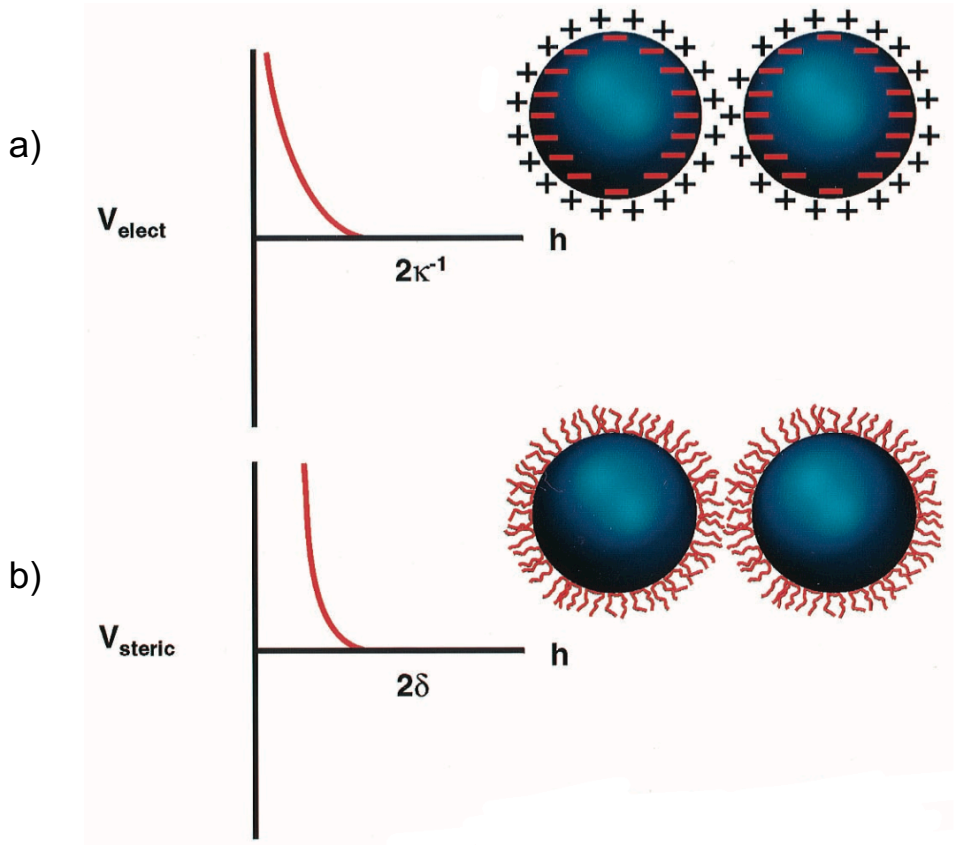

Figure 2.22: Schematic illustration of the interaction potential energy and relevant length scales for a) electrostatic, and b) steric, where κ^{-1} is the effective double-layer thickness, δ is the adlayer thickness. Adapted from: [105]

By contrast, steric stabilization is effective in both aqueous and non-aqueous colloidal systems. The thickness and adsorption density of the polymeric molecules forming the adlayer on particle surfaces are key to steric stabilization. As particles

approach one another, the adsorbed polymer chains first interpenetrate, then compress to induce a repulsive force that prevents particles from coming into contact. [105] A few typical polymer architectures used for steric stabilization is shown in **Figure 2.23**, including homopolymers, diblock and comb copolymers, and short-chain dispersants.

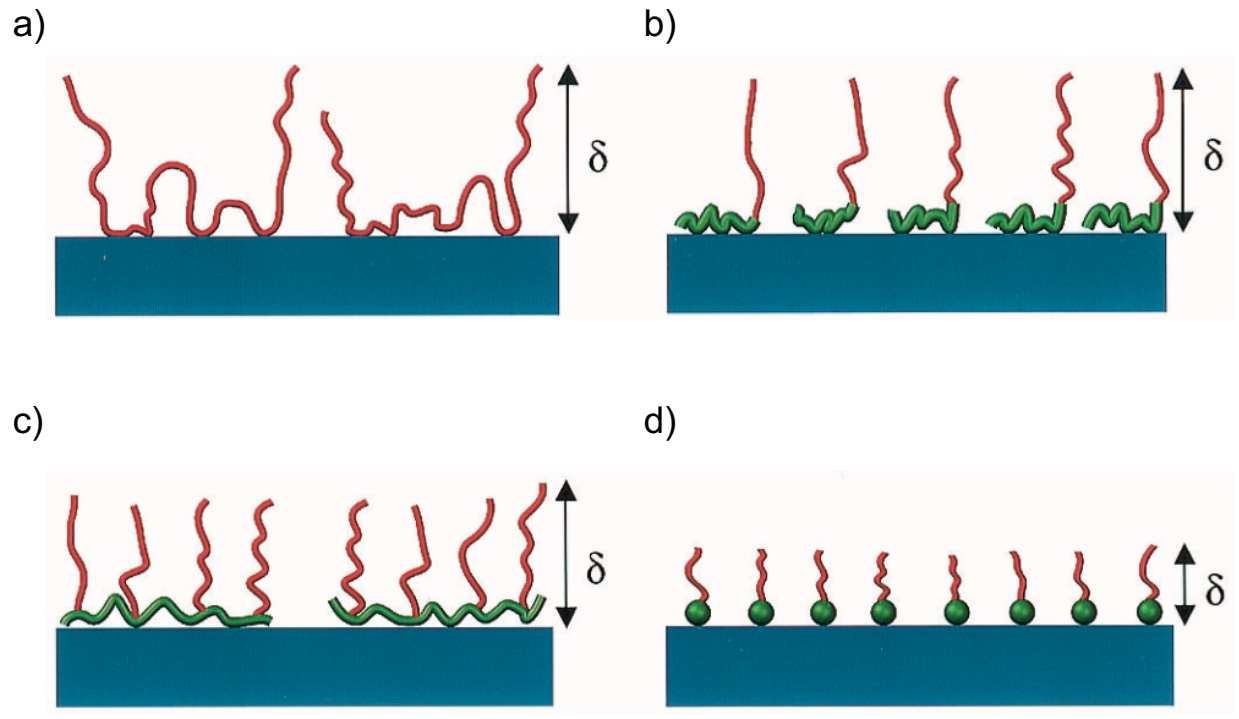

Figure 2.23: Schematics of common types of polymer architectures used in steric stabilization: a) homopolymer, consisting of tails, loops, and train configuration; b) diblock copolymer, consisting of short anchor block and extended chain block; c) comblike copolymer, consisting of extended segments attached to anchored backbone; and d) functional, short-chain dispersant, consisting of anchoring head group and extended tail. Adapted from: [105]

By carefully selecting the type of polymer to provide steric stabilization, concentrated Li-ion electrode suspensions can be prepared, even in high ionic strength non-aqueous

electrolyte (i.e. 1M LiTFSI/PC). Because of its versatility, steric stabilization is used to prepare electrode inks in this dissertation.

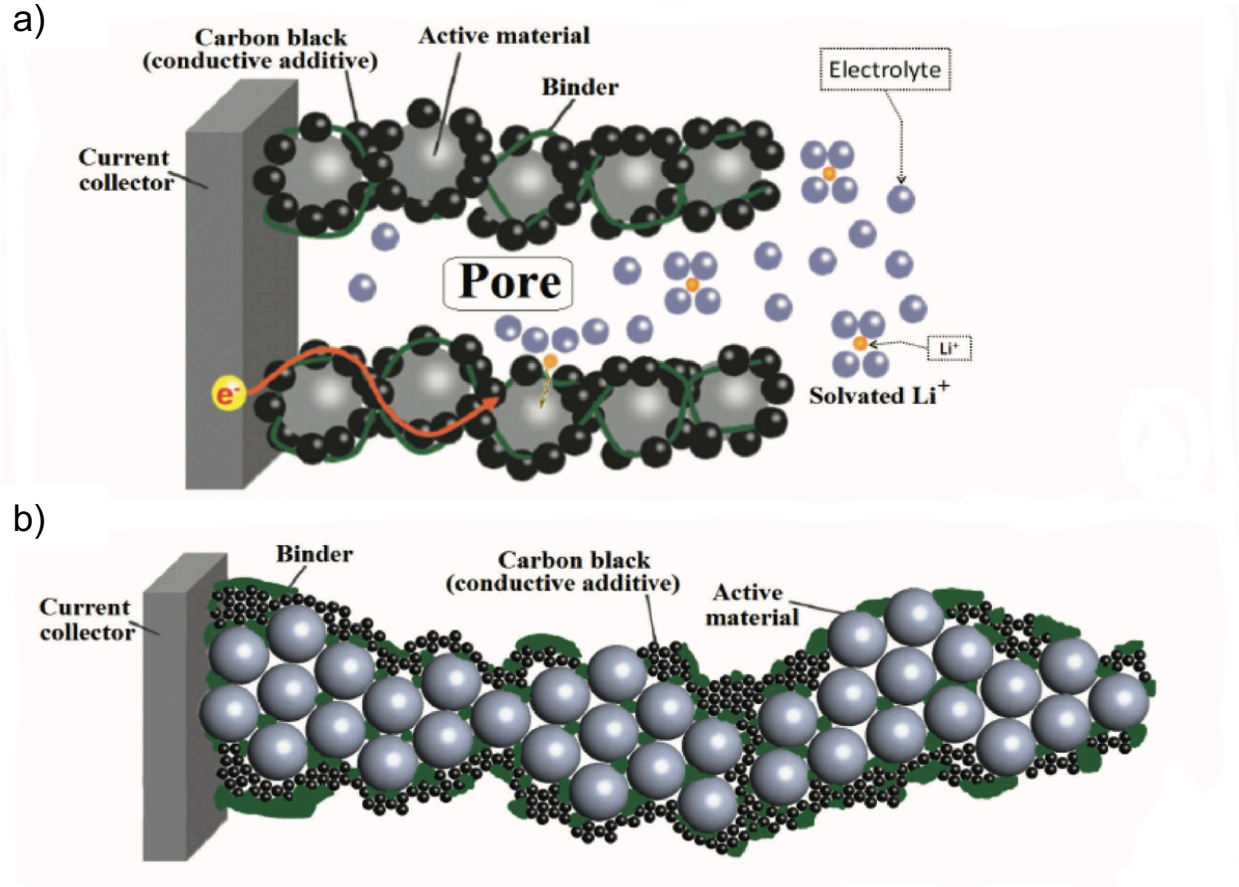

Figure 2.24: Schematics of LIB electrodes. a) The electrode with a favorable morphology, active material particles are dispersed, conductive carbon particles surrounding them as continuous electronic transport pathway, and the binder is adequately spreads across the material. b) A poorly prepared electrode, active material and conductive additive particles are agglomerated. Adapted from: [106]

Commercial Li-ion electrode suspensions consist of active material particles, conductive particles, binder, and electrolyte. **Figure 2.24a** nicely illustrates the highly preferable particle distribution, where the active material particles are well-dispersed and

are surrounded by a network of percolating conductive particles, enabling quick and efficient charge transport for improved electrochemical performance. While efficient morphology is key to creating high performing Li-ion batteries, it has been proven difficult to attain. [106] One promising strategy for creating tailored electrode suspensions is to develop biphasic systems. This concept is illustrated in **Figure 2.25**, in which two populations of silica, one stabilized with a cationic homopolymer, poly(trimethylammonium iodide ethyl methacrylate) (PTMAM), and the otherstabilized with PTMAM comb-polymer with uncharged poly(ethylene glycol) (PEG) teeth are suspended in DMSO/water [107] . Since the comb-polymer stabilized silica particles are non-ionic, they remain stable even when ionic strength is increased, whereas the silica particles stabilized with cationic homopolymer become attractive and undergo rapid flocculation [107].

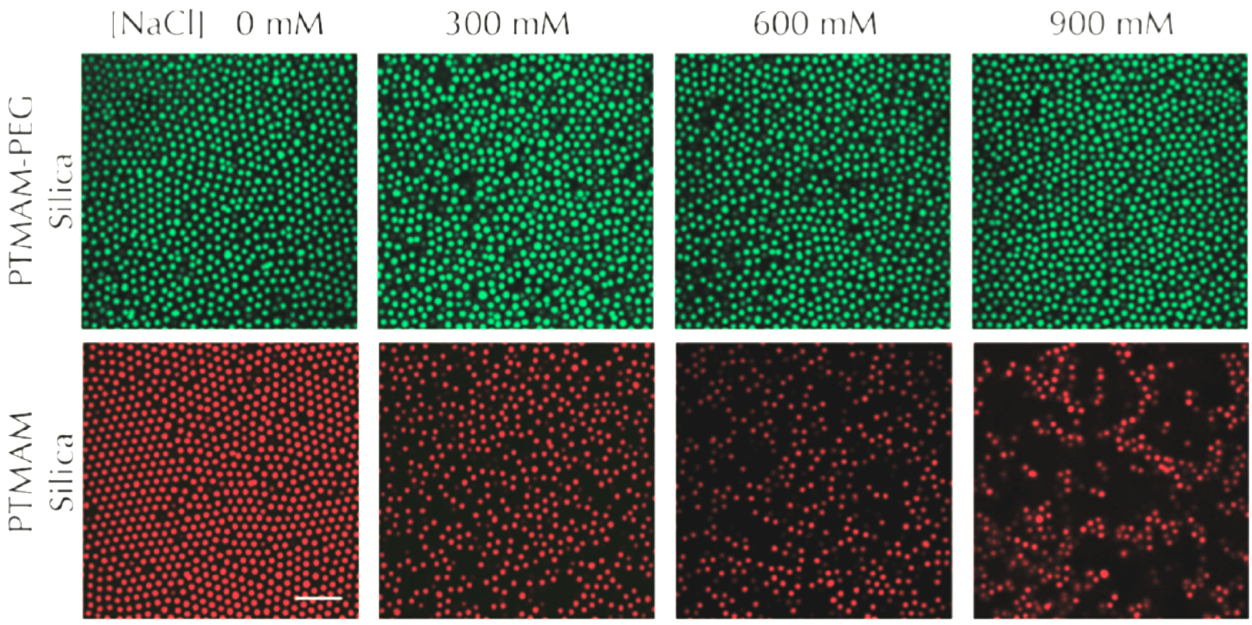

Figure 2.25: Confocal images of PTMAM-PEG (green) and PTMAM (red) stabilized silica particles showing a repulsive and an attractive particle interactions as ionic strength is increased. (scale bar = 5 μm for all images) Adapted from: [107]

Using biphasic mixtures of repulsive and attractive particles, Rhodes et. al. [108] investigated their microstructural evolution as a function of the ratio of the two particle population. Importantly, they found that an attractive particle network forms, whose interconnectivity can be tuned with increasing repulsive colloid volume fraction (**Figure 2.26**). [109] This critical finding is relevant for the biphasic Li-ion electrode suspensions, since we desire high active material loading (repulsive phase) with an interconnected network of electronically conductive particles (attractive phase), see Chapter 4. Notably, this same biphasic electrode design is also relevant for grid-scale battery applications, as reported in Chapter 5.

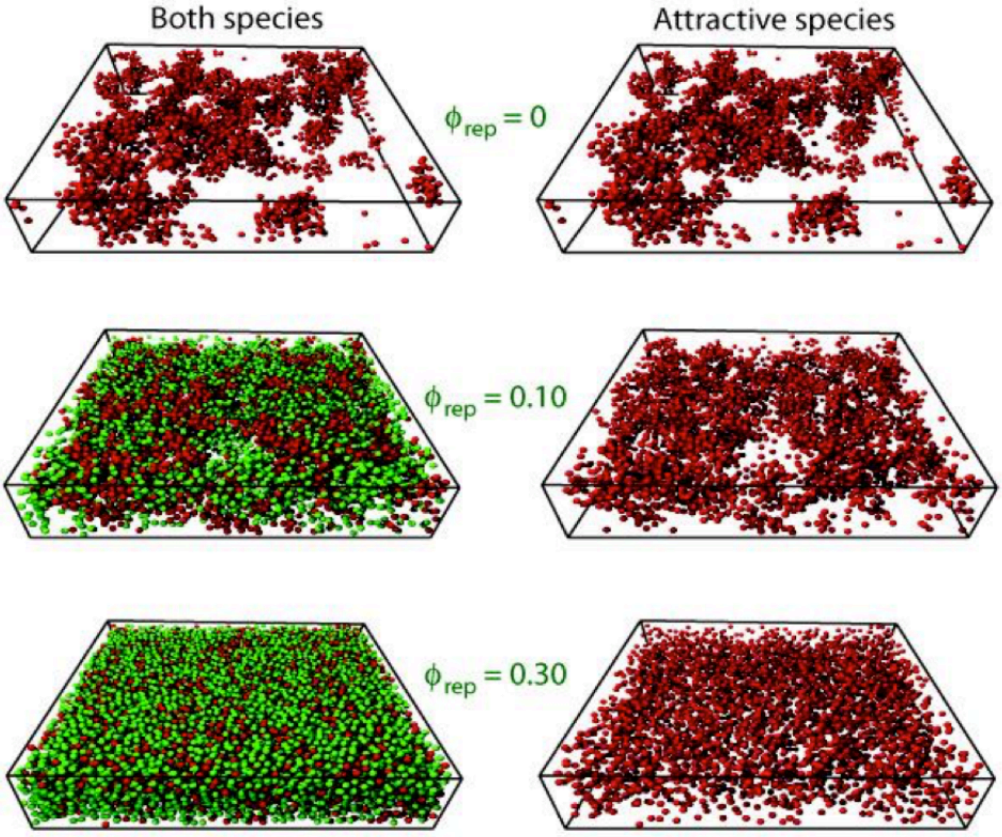

Figure 2.26: 3D reconstructions of PTMAM-PEG (green) and PTMAM (red) stabilized silica particles within biphasic mixtures with increasing repulsive particle content at fixed attractive particle content. Adapted from: [108]

2.4 Semisolid Flow Cells for Gird-Scale Energy Storage

Flow batteries are of particular interest for grid-scale storage applications due to their decoupled energy and power densities.[110-112] However, many flow battery chemistries suffer from limited solubility and low nominal voltage, resulting in low energy densities.[113] The previously mentioned SSFCs [7] replace traditional liquid catholytes by flowing energy dense Li-ion battery electrode suspensions instead. This design combines the scalability of flow battery with the high performance of Li-ion batteries, making SSFCs a strong candidate for large-scale energy storage applications.

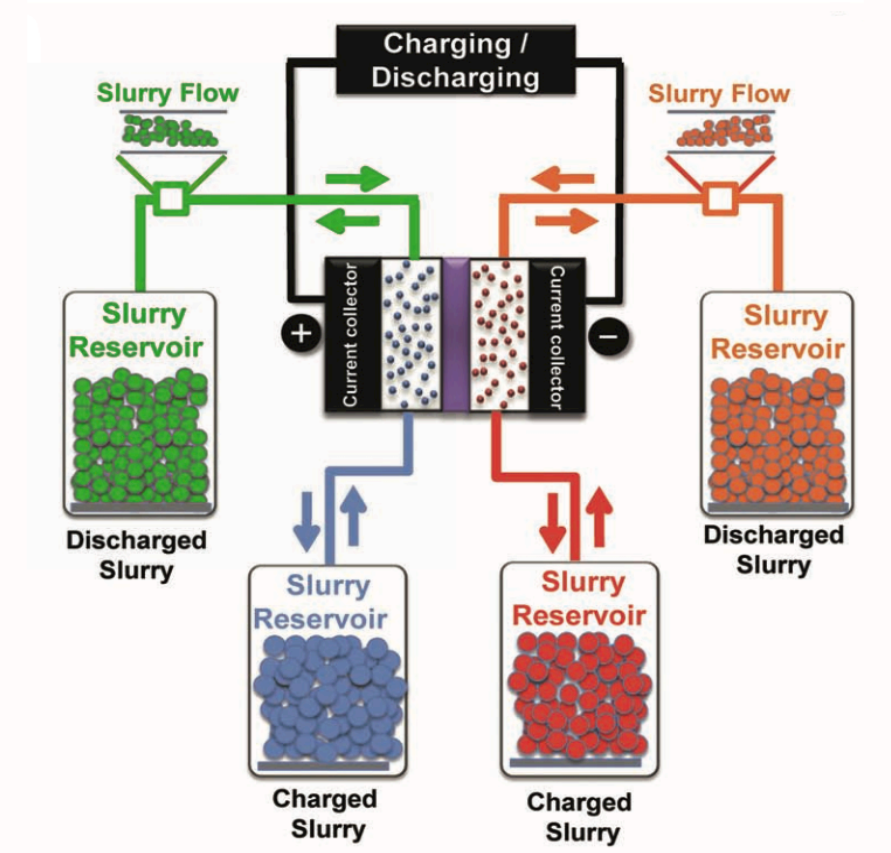

Figure 2.27: Schematic of a semisolid flow cell (SSFC) with the charged and discharged cathode and anode electrode suspensions stored in separate storage tanks. The suspensions are pumped through a reaction zone where electrochemical reactions undergo to store or supply energy. Adapted and modified from: [114]

Figure 2.27 shows how a typical SSFC operates, with four storage tanks that house charged and discharged cathode and anode suspensions, and a reaction zone where electrochemical reactions occur. The energy density of a SSFC scale with tank size, whereas the power density of a SSFC can be increased by stacking multiple reaction chambers together.

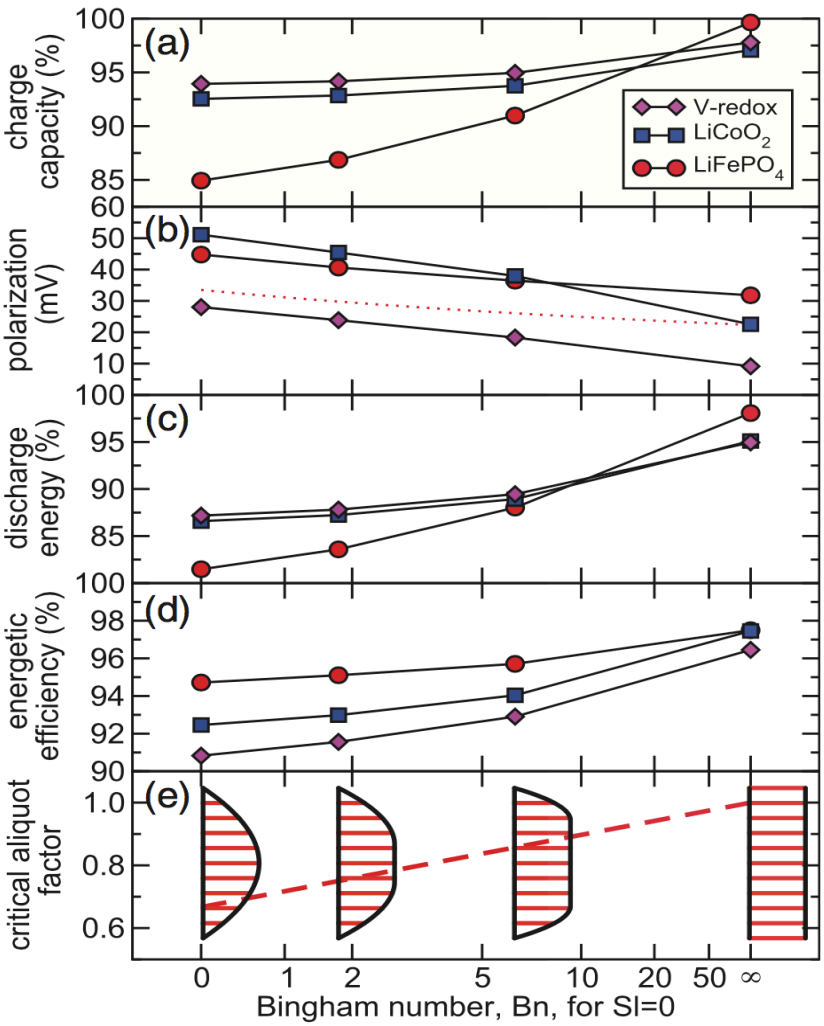

Figure 2.28: Flow battery performance as a function of Bingham number showing the corresponding flow velocity, showing the plug-flow scenario delivers the best performance regardless of the battery chemistry. a) charge capacity, b) average polarization, c) discharge energy, d) energetic efficiency and e) critical aliquot factor. Adapted from: [115]

To realize the full potential of SSFCs, flowing electrodes must have high active material content coupled with an adequate conductive filler network to overcome the resistive nature inherent to most electrochemically active Li-ion compounds. The simultaneous need for high solids content, efficiently distributed conductive fillers, and good flowability point to use of biphasic electrode suspensions for SSFCs. Additionally, the viscoelastic nature of biphasic electrode suspensions leads to nearly plug-flow behavior during operation, which is very desirable for achieving high capacity utilization, low voltage polarization, high energy density, and high energy efficiency [115] (**Figure 2.28**). The improved performance of plug-flow electrodes is associated with the more defined charge and discharge aliquots, with suspensions in different SOC or DOD well separated.

In summary, as the need for better energy storage increases across multiple scales, high areal capacity Li-ion batteries will be in ever greater demand. By combining novel electrode designs with additive manufacturing and flow cell architecture, further advances in performance and customizability can be achieved.

Chapter 3

3D Printing of Interdigitated Li-Ion Microbattery Architectures

This chapter has been adapted from the publication:

K. Sun, T.-S. Wei, B. Y. Ahn, J. Y. Seo, S. J. Dillon, J. A. Lewis, "3D Printing of Interdigitated Li-Ion Microbattery Architectures" Adv. Mater. 25, 4539 (2013).

3.1 Introduction

The proliferation of microscale devices, such as micro electromechanical systems (MEMS), [10] biomedical sensors, [11,12] wireless sensors, [13] and actuators [14] drives demand for power sources with commensurate form factors. 3D micro-battery designs based on micro- and nanostructured architectures [116-120] could potentially double the energy density by fully utilizing the limited space available. To date, such architectures have been produced in planar and 3D motifs by conventional lithography, [121-123] and colloidal templating methods, [124] respectively.

In this chapter, we will report the first demonstration of 3D printed Li-ion microbattery composed of high-aspect ratio anode and cathode micro-arrays that are interdigitated on a sub-millimeter scale, which exhibit amongst the highest areal energy and power densities in its class. The facile 3D printing technique allows functional inks to be precisely patterned in filamentary form over areas ranging from 100's μm^2 to 1 m^2 with minimum feature sizes as small as 1 μm. [105,125-128] We harness these capabilities to fabricate 3D interdigitated microbattery architectures (3D-IMA) composed of $Li_4Ti_5O_{12}$ (LTO) and $LiFePO_4$ (LFP), which serve as the anode and cathode materials, respectively

(**Figure 3.1**). These active materials exhibit minimal volumetric expansion, i.e., LTO (ε_{linear} ~ 0%) [129] and LFP (ε_{linear} 2.2%), [42] thereby reducing the requirement for compliance in the electrode to accommodate strain that accompanies charge and discharge processes. To create 3D-IMA, we first designed and optimized concentrated cathode and anode inks. We then printed interdigitated electrodes, packaged, and electrochemically characterized the 3D Li-ion microbattery.

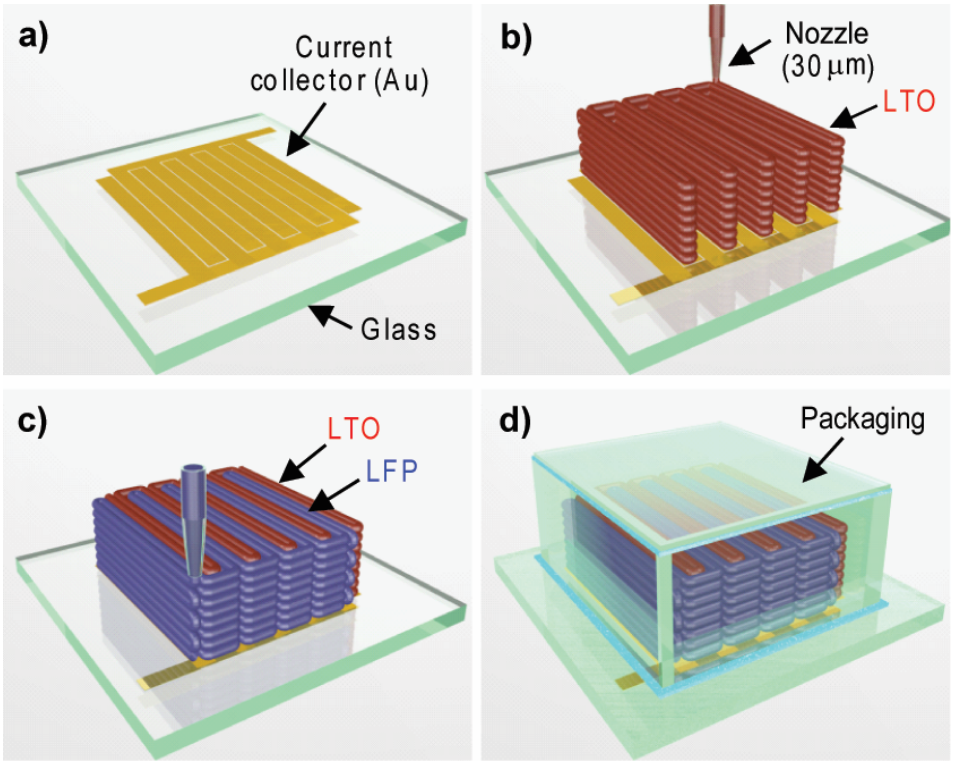

Figure 3.1 Schematic illustration of 3D interdigitated microbattery architectures (3D-IMA) fabricated on (a) gold current collector by printing (b) $Li_4Ti_5O_{12}$ (LTO) and (c) $LiFePO_4$ (LFP) inks through 30 µm nozzles, followed by sintering and (d) packaging.

3.2 Experimental Methods

3.2.1 Ink Synthesis

To syntheisze the 3D Printable cathode and anode inks, we purchased $Li_4Ti_5O_{12}$ (LTO, anode) powder (mean diameter = 50 nm, specific surface area = 32.6 $m^2 g^{-1}$, density = 3.539 g cm^{-3}) from Sigma Aldrich and synthezied $LiFePO_4$ (LFP, cathode) powder (particle size < 300 nm, density = 2.947 g cm^{-3}) with a solid-state reaction as described by Kang et al. [46] Highly concentrated LTO (57 wt% solids) and LFP (60 wt% solids) inks were prepared by first dispersing 4.5 g of LTO nanoparticles in 110 ml of deionized (DI) water and 40 ml of ethylene glycol (EG, Fisher Scientific) and 3.0 g of LFP nanoparticles in 80 ml of DI water and 40 ml of EG. These suspensions were ball milled for 24 h at room temperature and then classified by a two-step centrifugation process. The suspensions were first centrifuged at 4000 rpm for 5 min to eliminate large agglomerates, followed by centrifugation at 3500 rpm for 2 h to collect fine particles (mean diameter of 180 nm). The collected nanoparticles were re-dispersed with appropriate addition of glycerol (Fisher Scientific), 3.5 wt% aqueous hydroxypropyl cellulose (HPC, Sigma Aldrich, Mw~100,000) solution, and 3 wt% aqueous hydroxyethyl cellulose (HEC, Sigma Aldrich, binder) solution.

The resultant homogenized LTO mixture is composed of (relative to their solids content) 27 wt% Glycerol, 20~30 wt% EG, 9 wt% HPC, 1 wt% HEC, and DI water; whereas the LFP contained 20 wt% glycerol, 20~30 wt% EG, 8 wt% HPC, 2 wt% HEC, and DI water. Through solvent evaporation at room temperature, their final solids loading (nanoparticles and cellulose) was optimized to be 55 - 65 wt%.

3.2.2 Ink Rheology Characterization

Ink rheology was measured in both shear viscometry and oscillatory modes using a controlled-stress rheometer (C-VOR, Malvern Instruments, Malvern, UK) equipped with C14 cup and bob at 25°C in the presence of a solvent trap to prevent evaporation. The apparent viscosity (η) was acquired as a function of shear rate (0.01 - 500 s^{-1}) in a logarithmically ascending series. The shear storage (G') and viscous loss (G'') moduli were measured in an oscillatory mode as a function of controlled shear stress (10 - 10,000 Pa) at a frequency of 1 Hz with increasing amplitude sweep.

3.2.3 Battery Fabrication: 3D Printing

Before printing, interdigitated gold current collector patterns (960 × 800 μm^2, digit width = 70 μm, digit spacing = 50 μm) were patterned on glass substrates by a combination of lithographic patterning and e-beam deposition. The LFP and LTO inks were then printed sequencially using a 3-axis micropositioning stage (ABL 900010, Aerotech Inc., Pittsburgh, PA), whose motion was controlled by computer-aided design software (RoboCAD, 3D Inks, Stillwater, OK). The LFP and LTO inks were housed in separate syringes (3 mL barrel, EFD Inc., East Providence, RI), which were attached by luer-lok to a borosilicate micronozzle (30 μm in diameter produced using a P-2000 micropipette puller, Sutter Instrument Co., Novato, CA). An air-powered fluid dispenser (800 ultra dispensing system, EFD Inc.) was used to pressurize the barrel and control the ink flow rate. The typical printing speed for both LTO and LFP inks by a 30-μm nozzle was ~ 250 μm s^{-1} at 600 psi.

After printing, the structures were annealed at 600°C for 2 h in argon gas using a tube furnace. Their microstructures were characterized using SEM (Hitach S-4700). The calculated active mass of the printed LFP and LTO electrodes are 15 and 16 μg per layer, respectively, based on their filament geometry and the measured solids loading of each ink. To package the battery, a thin-walled poly(methyl methacrylate) (PMMA) preform was laser cut and placed around the microbattery and sealed with PDMS gel (Sylgard 184, Dow Corning, Inc.), cured at 150°C. The assembly was filled with liquid electrolyte and sealed with small glass cover using additional PDMS.

3.2.4 Battery Performance Characterization

All electrochemical characterization measurements were carried out in an argon-filled glovebox (Mbraun labstar), and electrochemical data was collected with a commercial potentiostat (SP200, Biologic Co.). For the half-cell test, the 3D printed LFP and LTO electrodes were immersed in a highly conductive nonaqueous electrolyte (1M $LiClO_4$ in 1:1 ratio of ethylene carbonate:dimethyl carbonate by volume). [130] A piece of lithium metal served as both the counter and reference electrodes. Cyclic voltammetry and galvanic charge/discharge were performed to check the electrochemical reactivity and rate capability. For the rate test, the charge rate was maintained at C/2, and discharge rates were varied from 1 C to 10 C. The cycling life was also measured in constant current, and both the charge and discharge rates were fixed at 1 C. For the full cell tests in liquid electrolyte, the same tests were performed again, where LFP and LTO served as the cathode and anode, respectively.

3.3 Results & Discussions

3.3.1 3D Printable LFP & LTO Inks

To print high aspect ratio electrode architectures, the composition and rheology of each ink must be optimized to ensure reliable flow through fine deposition nozzles, promote adhesion between the printed features, and provide the structural integrity needed to withstand drying and sintering without delamination or distortion. Concentrated anode and cathode inks are prepared by suspending LFP and LTO nanoparticles in a solution composed of deionized water (environmentally friendly), humectants (ethylene glycol, glycerol), and cellulose-based viscosifier via multi-step process that involves particle dispersion, centrifugation, and homogenization (experimental methods). The nanoparticles were selected as they excel in high power applications compared to larger microparticles. [57] This is due to the higher specific surface area and shortened diffusion length from the surface to the core of the active particles. This ties in well with the interdigitated electrode architecture aimed to improve power performance with the 2-sided diffusion direction from each tooth. Each ink was centrifuged to remove particulates above 300 nm in diameter to minimize ink clogging during printing. This filtration step ensures uniformly small active particles, not only critical to reliable 3D printing [126] but also for superior electrochemical performance. [131] We produced LTO and LFP inks of varying solids loading and found that those with respective solids loadings of 57 wt% and 60 wt% exhibited the desired rheological and printing behavior (**Figures 3.2a**).

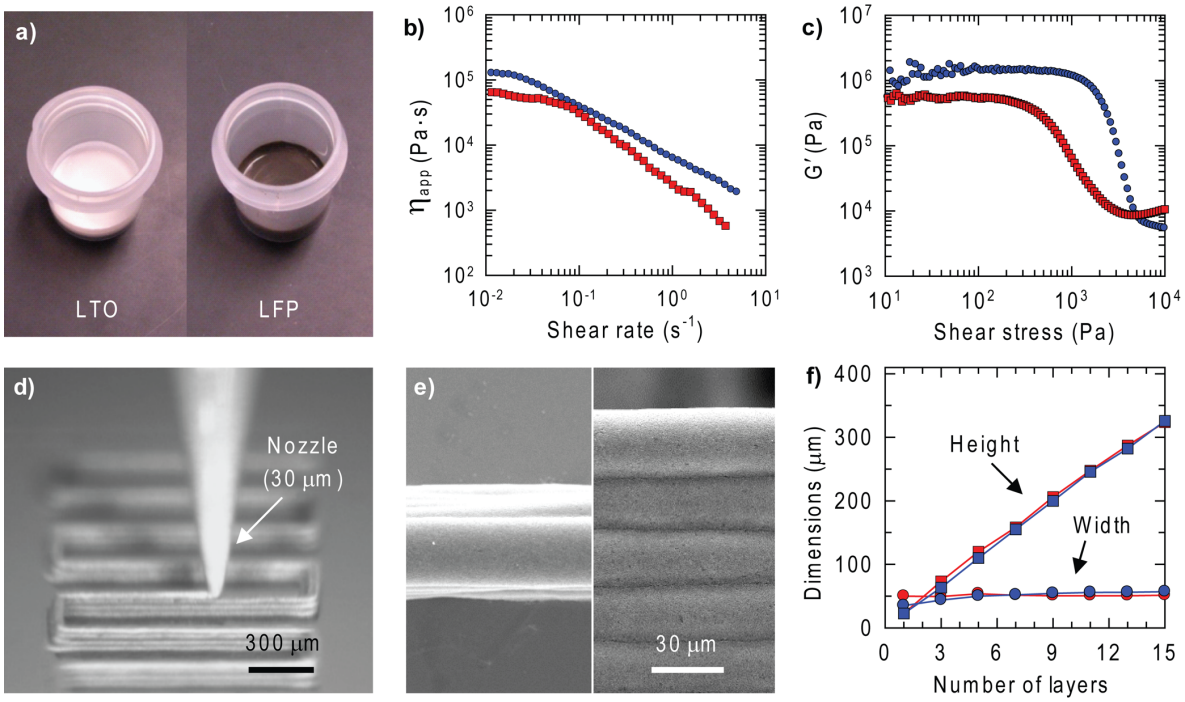

Figure 3.2 (a) Optical images of LTO and LFP inks. (b) Apparent ink viscosity as a function of shear rate. (c) Storage modulus as a function of shear stress for each ink. (d) Optical image of LFP ink (60 wt% solids) deposition through a 30 μm nozzle to yield multilayer structure. (e) SEM images, top (left) and side views (right), of the printed and dried multilayer LFP structure. (f) Height and width of printed features as a function of the number of printed layers (30 μm nozzle diameter). [Note: Red and blue symbols correspond to data obtained on LTO and LFP inks, respectively.]

Figure 3.2b shows their apparent viscosity as a function of shear rate. Each ink exhibits highly shear thinning behavior with respective apparent viscosities ranging from 10^3 – 10^4 Pa·s at 1 s^{-1}. **Figure 3.2c** shows their storage modulus (G') as a function of shear stress. The plateau modulus of each ink is ~10^6 Pa, while their shear yield stress (τ_y) ranges from 10^2 – 10^3 Pa, respectively. The magnitude of these key rheological parameters are in good agreement with those reported for other colloidal inks designed for 3D filamentary printing. [105,127,128] Shear thinning is a favorable property for ink-based 3DP since it allows super-linear flow rate increase with increasing applied pressure. Viscoelasticity is another highly desired coveted property as it enables 3D features to be

printed by shearing such ink beyond their yield stress to transition into a liquid-like (G″>G′), flowable state but return back to a solid-like (G′>G″), self-supporting state once exited from the printhead (zero shear).

3.3.2 3D Printing of Interdigitated Li-Ion Microbattery Architectures

We printed high aspect ratio, multilayer electrodes onto a glass substrate by depositing these inks through 30 μm tapered nozzles for reduced pressure drop (**Figure 3.2d**). To control ink solidification and adhesion during patterning, a graded volatility solvent system is used in which water (boiling point, b.p. 100°C) evaporation during printing induces partial solidification of the printed features ensuring their structural integrity, while ethylene glycol (b.p. 197.3°C) and glycerol (b.p. 290°C) serve as humectants that promote bonding between individual layers (**Figure 3.2e**). The presence of humectants also prevents inks from drying out at the nozzle tip, thus avoiding clogging of the nozzles. Printed features with aspect ratios (h/w, where h is height and w is width) of ~ 0.8 are obtained in a single pass with a minimum width of ~ 30 μm and high-aspect ratio features are readily obtained through a layer-by-layer printing sequence (Figure 3.2e). The 0.8 aspect ratio of the filament was selected for its balanced inter-layer adhesion and build-time. This is supported by the SEM images which reveal the interfaces of the printed layers are well bonded to one another. **Figure 3.2f** shows the height and width of LTO and LFP structures as a function of the number of printed layers. Notably, their height increases linearly with layer number, while their width is nearly constant. The aspect ratios of the patterned microelectrodes range from ~ 0.8 to 11 for single to 16-layer high aspect ratio walls. This is only possible with our rheologically engineered viscoelastic

inks with high yield stresses and elastic modulus sufficient to support its own weight without collapsing.

After printing, the dried LTO and LFP microelectrode arrays are heated to 600°C in inert gas for 4 h to remove the organic additives and promote nanoparticle sintering. Thermal gravimetric analysis (TGA) reveals that the organic species are largely removed by ~ 300°C (**Figure 3.3**).

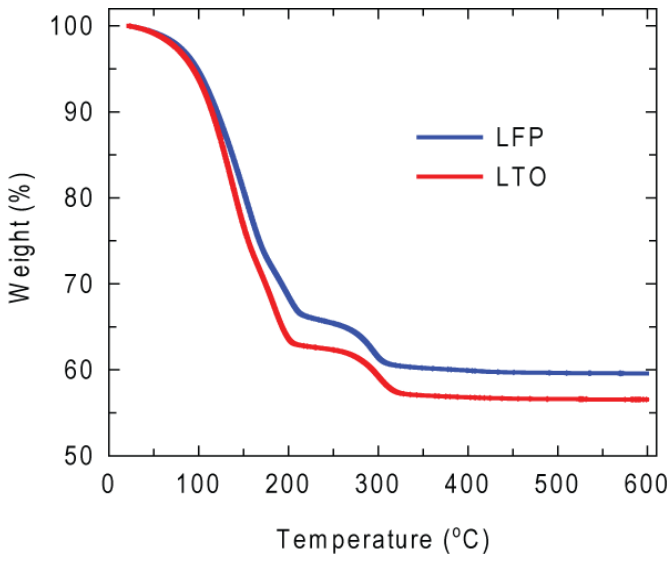

Figure 3.3 Thermal gravimetric analysis (TGA) of LFP and LTO inks heated at a ramp of 2°C min^{-1} in N_2

The electrical resistivities of the annealed LTO and LFP films measured by four-point probe are 2.1×10^5 Ω•cm, 2.3×10^3 Ω•cm, respectively. These values are significantly lower than their intrinsic electrical resistivities (~10^9 Ω•cm). [45,132] We speculate that such differences may arise from residual conductive amorphous carbon formed by decomposing the polymeric additives in an inert atmosphere (**Figure 3.4**). [48] The carbon layer at the particle surface forms a continuous electronic conductive pathway that is enabling for our high aspect ratio electrodes to work. [49] At higher temperatures, the

LTO and LFP particles undergo initial stage sintering leading to neck formation at particle-particle contacts. This annealed structures help connect the diffusion pathway along the particle surfaces, but remain desirably porous for better electrolyte penetration to ensure electrochemical reations can take place without suffering local electrolyte depletion (**Figure 3.5**). [69]

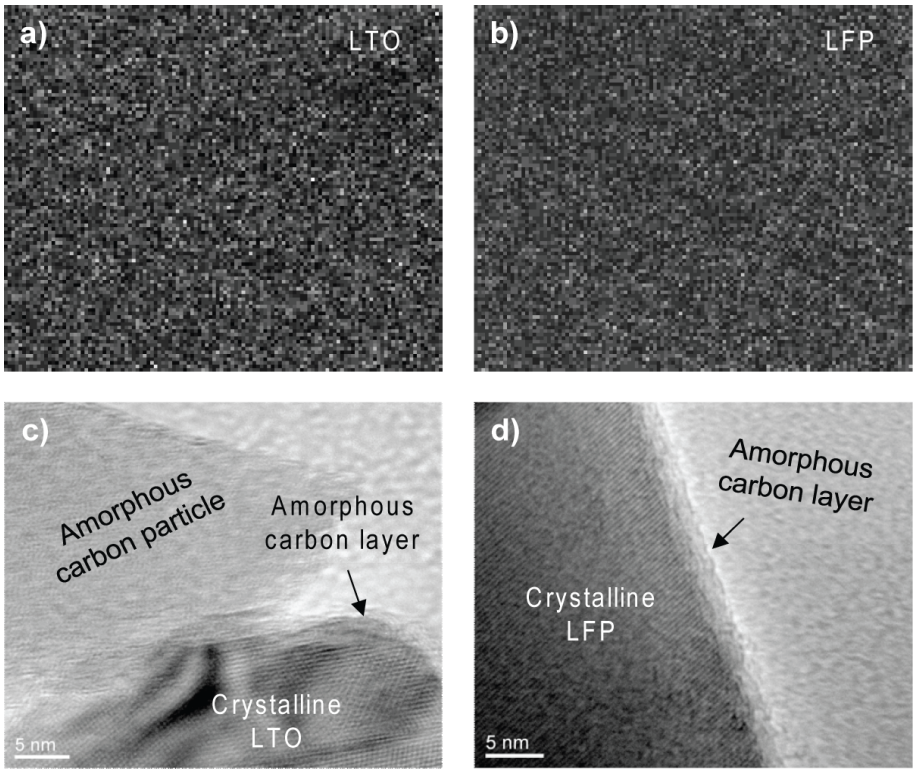

Figure 3.4 Carbon mapping of annealed (a) LTO and (b) LFP electrode structures. The bright contrast indicates regions with higher carbon distribution. TEM images of annealed (c) LTO and (d) LFP electrode structures.

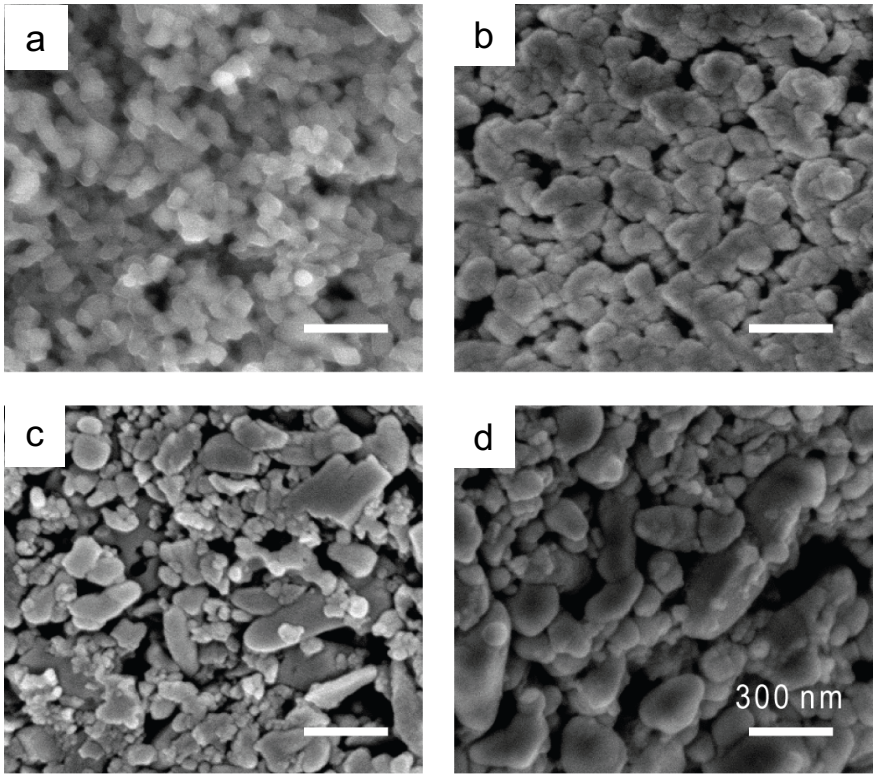

Figure 3.5 SEM images of (a) printed and (b) annealed LTO structures. SEM images of (c) printed and (d) annealed LFP structures. [Annealed at 600°C for 2 h in Ar gas]

3.3.3 Electrochemical Characterization of 3D-IMA

To investigate their electrochemical performance, we printed 8-layer and 16-layer 3D-IMA (960 × 800 μm^2, electrode width = 60 μm, spacing = 50 μm) on glass substrates (**Figure 3.6a**) followed by drying and annealing at 600°C for 2h in an inert atmosphere (**Figure 3.6b**). The final test structures exhibited minor distortion, but no sign of shorting via contact between adjacent electrodes or delamination from the substrate. We first measured discharge properties for half-cells composed of LFP (**Figure 3.6c**) and LTO (**Figure 3.6d**) electrodes at varying C rates. The specific capacities for these 8-layer structures at 1 C are calculated to be 160 and 131 mAh g^{-1}, respectively, in good agreement with their respective theoretical values of 170 [45] and 175 [58] mAh g^{-1}. A common feature of both data is the non-monotonic variation in discharge capacity with electrode volume

between the 8-layer structures and the 16-layers structures at the lowest rate (1 C). The results indicate that the height of the structure will constrain the kinetics of the reaction. Electronic transport is the only height dependent property in the system, and likely limits the functional height of the 3D-IMA in its current incarnation. At 5 C and 10 C, the 16-layer and 8-layer LFP electrodes exhibit the same current density of 8.33 mA cm^{-2}. The complete overlap in these data supports the hypothesis that electronic conduction limits their rate capability, as the total contribution to the capacity results from the same depletion region in both electrodes. Strategies to enhance electronic transport, e.g., through the inclusion of conductive fillers, to overcome the longer diffusion length of the thicker electrodes will be explored in Chapter 4.

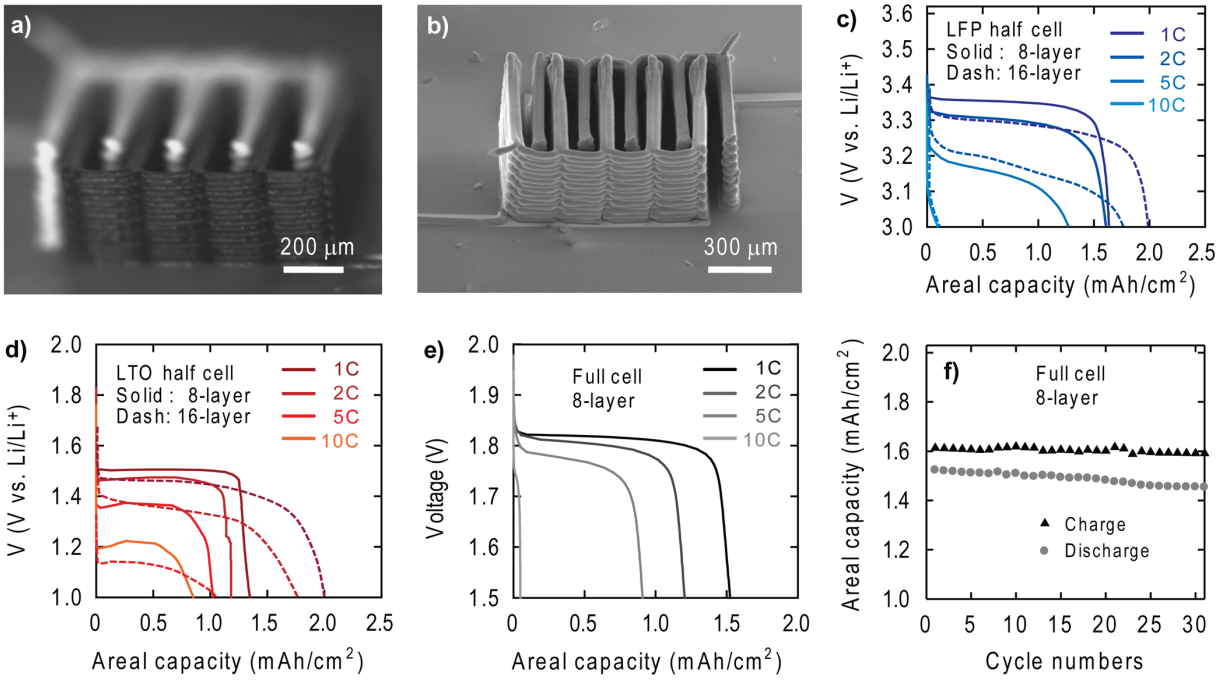

Figure 3.6 (a) Optical and (b) SEM images of printed and annealed 16-layer interdigitated LTO-LFP electrode architectures, respectively. Half-cell voltage as a function of areal capacity for (c) LFP and (d) LTO electrodes. (e) Full-cell voltage as a function of areal capacity for an 8-layer electrode structure. (f) Areal capacity of full cell composed of an 8-layer electrode structure measured over 30 cycles.

Figure 3.6e depicts the areal capacity of an 8-layer LTO-LFP 3D-IMA as a function of C rate. The battery delivers ~1.5 mAh cm^{-2} at a desirable stable working voltage of 1.8 V when discharged below 5C. The result corresponds well with the LFP and LTO half-cell results. **Figure 3.6f** demonstrates the cycle life of the 3D-IMA. Minimum decay in capacity occurs up to 30 cycles. LFP and LTO both exhibit good cycle life due to their low-strain topotactic reactions that take place at relatively low and high voltages, respectively.

3.3.4 Electrochemical Characterization of Packaged 3D-IMA

Figure 3.7 shows a packaged 3D-IMA. A small plastic case (inner dimensions: 2.1 mm × 2.1 mm × 1.5 mm) fabricated by laser machining contains the microbattery and liquid electrolyte (Figure 3.7a). The case dimensions far exceed those needed, and may be reduced by directly printing the polymeric case and liquid (or gel) electrolyte. Cyclic voltammetry performed on the packaged 3D-IMA between 1.0 and 2.5 V at a scan rate of 5 mV s^{-1} is shown in Figure 3.7b. Stable oxidation and reduction peaks occur at 1.3 V and 2.4 V. After cyclic voltammetry, galvanostatic charge and discharge was conducted at a rate of 0.5 C (Figure 3.7c). The capacity of the packaged 3D-IMA is 1.2 mAh cm^{-2}, normalized to the area of the current collector. The packaged battery does not exhibit long-term cyclability due to lack of hermeticity. Effectively packaging microbatteries (<1 mm^3) that contain liquid (or gel) electrolyte is quite challenging and few examples of stable packaged microbatteries have been reported to date. [76] Further optimization of microbattery packaging is explored in Chapter 4.

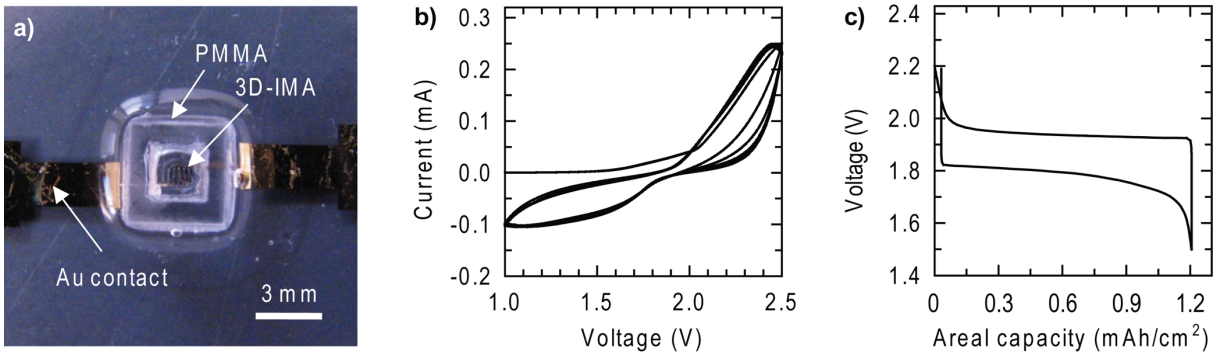

Figure 3.7 (a) Optical image of 3D-IMA composed of LTO-LFP electrodes after packaging. (b) Cyclic voltammetry of the packaged 3D-IMA. (c) Charge and discharge curve of the packaged 3D-IMA.

3.3.5 Battery Performance Comparison

The Ragone plot in **Figure 3.8a** compares the areal energy and power densities of our 3D-IMA with other relevant data recently reported in the literature.[76,120,123,133-143] As a power source storing energy, the best rechareable battery will be desirably positioned at the upper right corner of the Ragone plot. This indicates high energy density that translates into minimal battery size and longer single-charge battery life, and high power density which corresponds to being a high wattage power source. A Ragone plot that compares their performance in terms of volumetric energy and power density is provided in **Figure 3.8b**. We do not include data for the fully packaged 3D-IMA in either plot due to the excessively large, non-optimized package dimensions. The printed 3D-IMA compares favorably against its rechargeable counterparts in terms of both areal energy and power density. The excellent performance results from the fabrication of high-aspect structures that occupy a small areal footprint, while maintaining reasonably small transport length scales to facilitate facile ion and electron transport during charging and discharging processes. While the low voltage electrochemical couple demonstrated here limits the volumetric energy density, our approach can readily be extended to other

commercial lithium ion chemistries, such as $LiCoO_2$/graphite, to yield volumetric energy densities competitive with those reported elsewhere. [76,143]

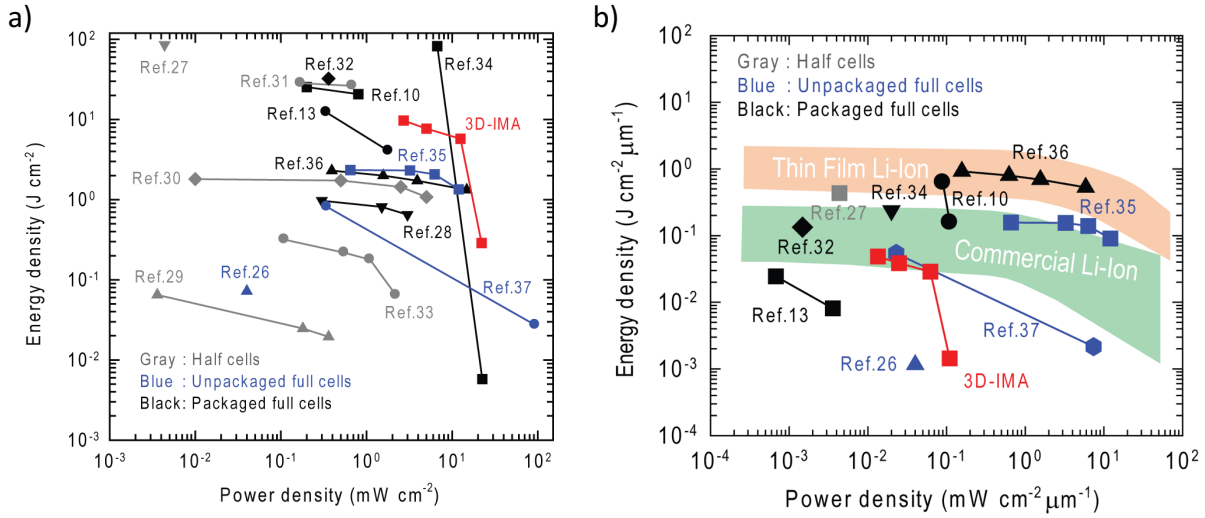

Figure 3.8 Ragone plots comparison of the areal (a) and volumetric (b) energy and power densities of our printed, unpackaged 3D interdigitated microbattery architectures (3D-IMA) to reported literature values.

Since 3D printing is an additive manufacturing technique, one could envision fabricating Li-ion batteries directly on top of an electronic device. As a proof of concept, **Figure 3.9a** and **Figure 3.9b** show a 2D-array of 3D printed LTO electrodes and one printed directed on the side of a pencil, respectively.

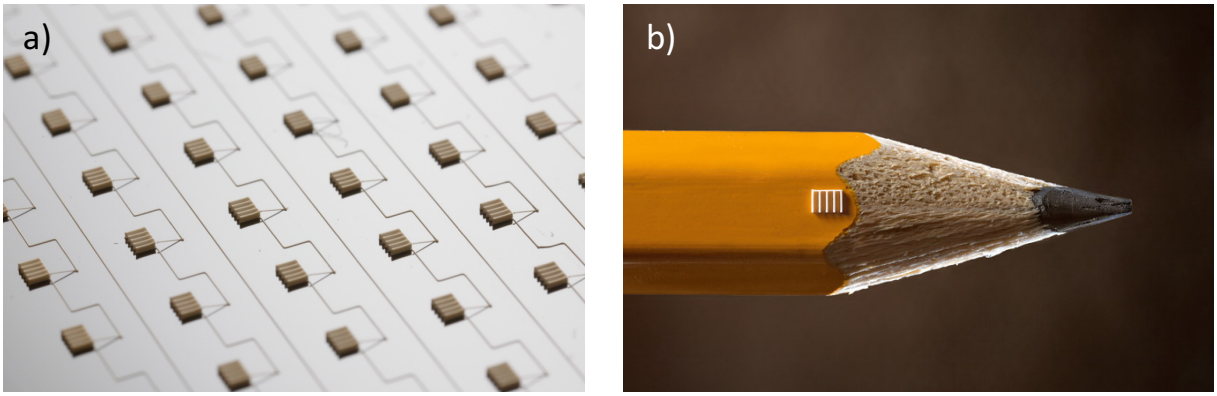

Figure 3.9 (a) A 2D-array of 3D printed LTO electrodes and (b) one fabricated directly on the side of a pencil are shown to demonstrate the versatility of 3D printing

To realize the full potential of 3DP Li-ion batteries, several issues must be addressed (see Chapter 4). First, the packaging process must be improved to enable better hermetic sealing. Second, the inactive area, volume and weight of the packaged battery must be minimized to enhance the energy and power densities. Third, in the current approach, the overall yield is low due to electrode drying and sintering defects [66] such as cracking and delamination. Finally, conductive fillers must be incorporated into the electrode inks to enhance electronic transport and overcome the longer diffusion length of the thicker electrodes. This advance will further improve areal energy and power densities, while also voltage polarization and increase energy efficiency.

3.4 Conclusion

In summary, we have printed novel 3D microbatteries composed of high-aspect ratio electrodes in interdigited architectures. Careful design of concentrated LFP and LTO viscoelastic inks enabled printing of these thin-walled anode and cathode structures. Using this LFP-LTO chemistry, we have demonstrated 3D-IMA with a high areal energy density of 9.7 J cm^{-2} at a power density of 2.7 mW cm^{-2}. These devices may find potential application in autonomously powered microelectronics and medical micro-implants. By further leveraging the versatility of 3D printing, one could envision Li-ion batteries be fabricated in parallel or series arrays to tailor the battery's performance to the current or voltage requirements.

Chapter 4

3D Printed Li-ion Batteries with Ultrathick Electrodes

This chapter has been adapted from the publication:

T.-S. Wei, B. Y. Ahn, J. Grotto, J. A. Lewis, " 3D Printed Li-ion Batteries with Ultrathick Electrodes" in preparation (2017).

4.1 Introduction

Rechargeable Li-ion batteries (LIBs) are widely used in applications ranging from portable electronics[1] to electric vehicles[4]. Commercial LIBs are limited to simple shapes (e.g., coin, cylinder, prismatic and pouch cells) composed of repeating electrode stacks of relatively thin electrodes (20 μm - 100 μm thick) separated by a polymer or polymer-ceramic film and sandwiched between two current collecting (metal) foils.[2] However, the growing demand for LIBs with higher capacity, faster charge-discharge rates, and lower cost underscores the need for new electrode materials, battery architectures, and fabrication methods [8,20,75,104,143,144]. For example, high capacity anodes based on silicon[145] have been studied extensively, yet challenges remain in controlling their pronounced volumetric changes during lithiation/delithiation cycles. More recently, 3D battery architectures templated from colloidal crystals or holographically defined polymer lattices have been reported, which exhibit high charge/discharge rates [124,143]. However, their energy capacity is limited by both the

interconnected porosity required for electrolysis deposition as well as the resulting thin conformal electrodes deposited onto these 3D structured current collectors.

A promising alternative approach is to create 3D LIBs with thick electrode architectures. [8,63,73,76,146] The volumetric ratio of active/inactive materials within LIBs, and, hence their energy density, scales linearly with electrode thickness for a given areal footprint. However, ion and electronic transport through thick electrodes is more difficult, which limits their power density [68-70]. To enhance ion transport, researchers have recently focused on fabricating Li-based cathodes with internal open channels oriented orthogonally to current collector surfaces [75]. Using magnetic-field induced alignment of anisotropic porogens composed of either magnetic particle-coated polymer rods or particle-stabilized emulsion droplets, sintered $LiCoO_2$ (LCO) cathodes (310 μm thick) were created with an impressive areal capacity of ~12 mAh cm^{-2} at a 0.1 C rate[75] To enhance electronic transport, highly porous metal foams were employed as 3D current collectors to create high performance $LiFePO_4$ (LFP) cathodes (540 μm thick) with an areal capacity of 8.8 mAh cm^{-2} at a current density of 1 mA cm^{-2}.[8] The use of thicker electrodes also lead to inherent processing challenges, including binder migration, cracking and delamination during drying [62] and incomplete electrolyte infiltration [72], which lead to microstructural inhomogeneity.

We recently demonstrated the fabrication of LIBs microbatteries by 3D printing cathode, $LiFePO_4$ (LFP), and anode, $Li_4Ti_5O_{12}$ (LTO), inks in the form of interdigitated electrodes [104]. Specifically, high aspect ratio LFP and LTO electrodes were printed with a wall thickness of ~ 60 μm and height between ~ 200-400 μm onto a glass substrate patterned with gold current collectors. These micro-LIBs (total volume < 1 mm^3)

delivered an areal capacity of ~1.5 mAh cm^{-2} when discharged at a rate below 5C. However, due to electronic transport limitations, LFP electrodes at 8 layers (~ 240 μm thick) exhibited the same current density as those with 16 layers (~ 480 μm thick). It was also difficult to hermetically package these microbatteries.

Here, we report the design, fabrication, and electrochemical performance of 3D printed LIBs composed of ultrathick, biphasic semisolid electrodes with ten-fold higher areal capacity compared our prior microbattery design. Specifically, [38] by mixing well dispersed, active electrode particles (LFP or LTO) with attractive conductive carbon particles that form a percolative network in an lithium-based electrolyte solution, we create biphasic electrodes with tailored rheological, printing, and electronic/ionic transport behavior. We also produced packaging and separator inks composed of ceramic-filled polymer composites that can be UV cured upon 3D printing. Together, these four inks are used to create fully 3D printed LIBs with ultrathick electrodes patterned in arbitrary geometries that are encased between two glassy carbon current collectors (**Figure 4.1**). Our additive manufacturing appoach eliminates the need for drying, electrolyte-infilling, calendering, clamping, and heat-sealing processes typically associated with conventional LIB manufacturing.

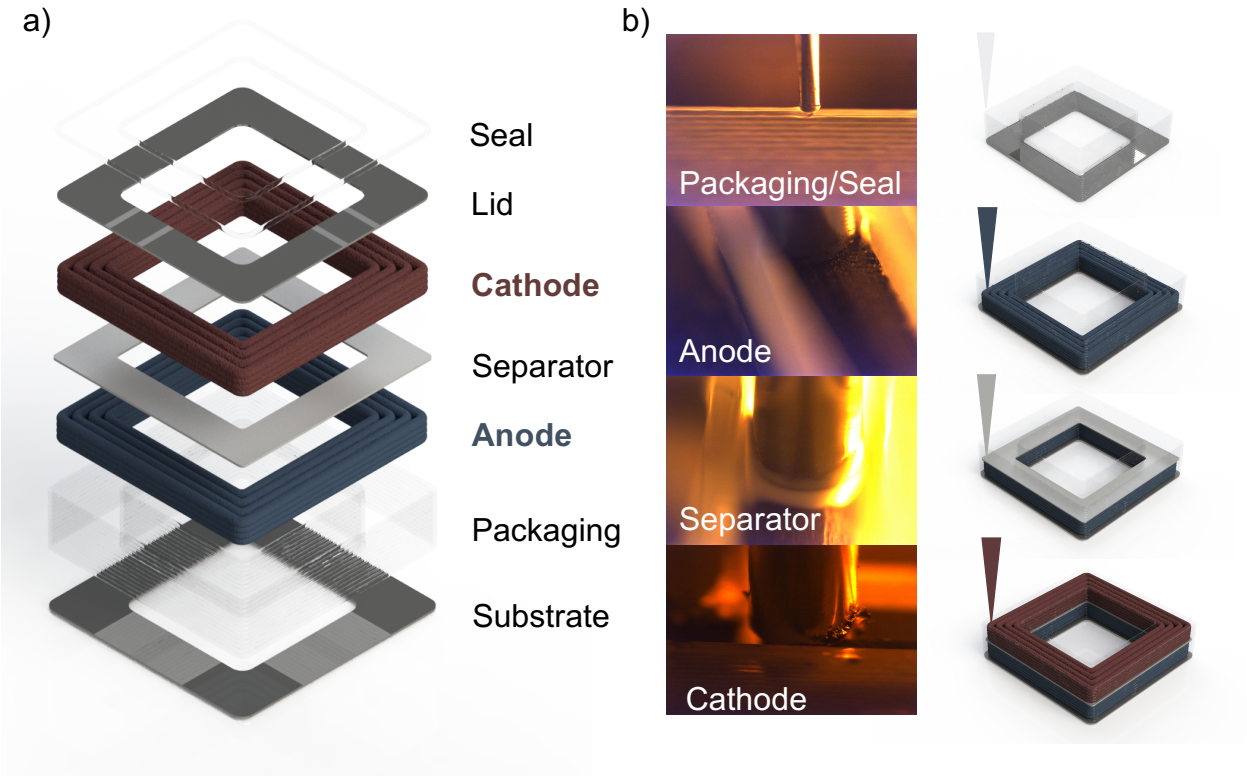

Figure 4.1. a) Schematic representation (exploded view) of the fully 3D printed Li-ion battery demonstrated in this work. The cell size is 1 cm × 1 cm × 2.5 mm with a 6 mm × 6 mm through hole at the center. b) Digital photographs and schematics showing the extrusion of the four functional inks. The substrate, anode, separator, cathode, lid, seal, and packaging are 0.18 mm, 1 mm, 0.1~0.15 mm, 1 mm, 0.18 mm, 0.1 mm, and 2.4 mm thick, respectively.

4.2 Experimental Methods

4.2.1 Ink Synthesis

The materials used to synthesis the four functional inks include carbon-coated $LiFePO_4$ (LFP) (M121, Advanced Lithium Electrochemistry Co., Ltd., Taoyuan, Taiwan) and carbon-coated $Li_4Ti_5O_{12}$ (LTO) (LTO-1, BTR NanoTech Co., Shenzhen, China) active particles, and Ketjenblack (KB) (EC-600JD, Azko Nobel Polymer Chemicals LLC, Chicago, USA) conductive particles. Propylene carbonate (PC) (anhydrous, 99.7%), polyvinylpyrrolidone (PVP) (Mw = 40kg mol^{-1}), Triton X-100 (TX-100) (laboratory grade), ETPTA (M_w = 428, trivalent acrylate monomer), HMPP (2-hydroxy-2-methyl-1-phenyl-1-propanon, photo-initiator) are acquired from Sigma-Aldrich. The Lithium bis(trifluoromethane)sulfonamide (LiTFSI) is provided by BASF. The fumed SiO_2 used in the packaging ink is supplied by Cabot (CAB-O-SIL TS-720). The Al_2O_3 used in the separator ink is provided by Sumitomo Chemical (AKP-30). The UV-curing epoxy is obtained from Electronics Materials Inc. (Optocast 3553-40k).

Biphasic electrode suspensions are prepared in an argon-filled glovebox with moisture and oxygen content maintained under 0.5 ppm. All dry materials are heated at 120°C overnight under vacuum to remove moisture. First, 250 mL HDPE bottles are filled with 5 mm (250 g) and 0.5 mm (150 g) yttrium stabilized zirconia (YSZ) milling beads. Next, PC (50 g), PVP (0.1 g), and LFP or LTO powder (10 g) are added. The bottles are sealed and the suspensions are ball-milled (US Stoneware) under ambient conditions for 24 h. The suspensions are then filtered through 20 μm stainless steel sieves in the argon-filled glovebox. The filtered suspensions are sealed in the glovebox and centrifuged (Beckman Avanti J-25 I) at 12,500 g for 30 min to collect the dispersed particles. After

removing the supernatant, the dense sediment (typically 65 wt% solids content) is collected and homogenized using a planetary mixer (Thinky AR-100). Additional PC is then added and mixed, followed by LiTFSI to achieve 1 M electrolyte concentration. Finally, KB powder is added and homogenized. The final ink compositions are 30 vol% LFP with 1.25 vol% KB for the cathode and 30 vol% LTO with 1.35 vol% KB for the anode in 1M LiTFSI/PC with 1 wt% PVP% (with respect to LFP or LTO) to transition LFP and LTO into repulsive particles.

The separator ink is prepared by ball milling, filtering, and centrifuging a Al_2O_3 suspension the same way as with the biphasic electrode suspensions, but using starting materials composed of PC (50 g), TX-100 (1 g), and Al_2O_3 powder (20 g). Once the dense sediment (typically 78 wt% solids) is collected in a UV-protected scintillation vial and homogenized, appropriate amount of 2% HMMP solution (ETPTA:HMMP = 100:1) and 1M LiTFSI/PC are added and Thinky-mixed. Finally, ETPTA is added and the vial is sealed and vortex-mixed for 30 min at 1500 rpm followed by 1min Thinky-mix to avoid partial curing from overheating. Packaging ink is prepared by mixing 4 vol% of fumed SiO2 into UV-curing epoxy through multiple cycles of Thinky-homogenization in a UV-protected scintillation vial.

4.2.2 Rheology & Microscopy Characterization

Rheology is performed at 22°C on a TA Instrument AR-2000EX rheometer using smooth surface finish stainless steel parallel plates or cone & plate geometries with the appropriate diameter (20, 40, or 60 mm) at the appropriate gap heights (0.5 to 1.5 mm)

gap height. Small diameter parallel plates are used for high viscosity samples with larger gap heights to prevent the wall-slip effects. Solvent trap is added not only to prevent evaporation, but to block UV-light when testing separator and packaging inks. Oscillatory measurements (G´, G˝) were done at fixed frequency (10 rad/s). All samples are pre-sheared at 1 s^{-1} for 60 s prior to measurement and left to equilibrate until the normal force relaxes (~60 s).

Micrographs of KB suspensions are taken using an inverted optical microscope (OLYMPUS IX71). The repulsive SiO_2 particles are dispersed with PVP and imaged using index-matched water-glycerol solution. Suspensions are sandwiched between two cover slides for imaging.

4.2.3 Electrochemical & Conductivity Characterization

All electrochemical experiments are performed using the Biologic VMP-3 potentiostat. A standard galvanostatic cycling setup includes a two-electrode Swagelok cell [38] with a porous polymer separator film (Celgard) soaked in electrolyte (1M LiTFSI/PC), stainless steel current collectors, and PTFE spacers to define the electrode thickness (area = 0.5 cm^2). Glassy carbon and composite separator characterization are performed with circular cutout of them placed appropriately to replace the Celgard separator or stainless steel current collectors.

Electronic conductivities of the biphasic electrode inks are measured by the DC method, where the voltage is swept from 0 to 100 mV (Biologic VMP-3). The test cell used

is a modified Swagelok cell with a cylindrical volume for the material of interest, sandwiched by two stainless steel electrodes [38].

AC Impedance study is performed with fully assembled Swagelok LFP/LTO cells at amplitude of 10 mV and frequency range of 0.1 Hz to 0.3 MHz for the 1.0 mm electrodes, and 1 Hz to 0.2 MHz for the 0.1 mm electrodes. CV study is also performed with fully assembled Swagelok cells from 0.5 to 3.0 V at various scan rates.

Self-discharge test is done by first fully charging a LFP/LTO battery to 2.5 V at 0.2 mA cm^{-2}, then holding it at 2.5 V for 24 h prior to recording the open circuit voltage (OCV) over 20 days.

4.2.4 3D printed LIBs with Ultrathick Electrodes

LIBs are fabricated using a custom-made 3D printer that was assembled and operated inside of an Ar-filled glovebox consisting of a 3-axis micropositioning stage (Sherline 5400) motorized by stepper motors (CNC4PC, CS4EA4-1Rev1), controlled by computer-aided milling software (Mach3). The cathode, anode, separator, and packaging inks are housed in separate 3ml syringes (UV-protected ones for separator and packaging) and attached by luer-loks to appropriately sized (as small as 100 μm) metal tips (EFD Inc.). An Ar-powered fluid dispenser (HP3cc, EFD Inc.) is used to pressurize the barrel up to 700 psi to control the flow rate. The pressure is analog-controlled and its Mach3-macro (written by Mr. Koseki Kobayashi) enabled control over pressure change and stage movement via g-code.

First, the packaging ink is printed onto the laser-cut (Photonics Industries, DC150H-355) glassy carbon substrate (Goodfellow, Vitreous 1000C, thickness = 0.18 mm) to 2.5 mm tall followed by 60 min of UV-curing (UVL-21, 365 nm, 4W, by UVP). Next, the anode ink is next printed onto the glassy carbon substrate within the packaging walls to 1 mm tall. The separator is then printed onto the anode to form a thin separator film, followed by 30 min of UV-curing. The cathode ink is then printed onto the separator with a thickness of 1.0 mm. The glassy carbon lid is then carefully placed on top of the cathode. Lastly, packaging ink is printed on top of the lid to seal/bond it to the UV-cured packaging walls. A final UV-curing step (~30 min) is carried out to finish the battery fabrication. We would like to note the UV curing steps could be shortened significantly if a higher wattage UV lamp is used. The substrate, anode, separator, cathode, lid, seal, and packaging are 0.18 mm, 1 mm, 0.1~0.15 mm, 1 mm, 0.18 mm, 0.1 mm, and 2.4 mm thick, respectively.

4.2.5 Electrochemical Characterization of 3D Printed LIBs

The 3D printed LIBs are tested by attaching copper leads to the glassy carbon current collectors with conductive silver paste (kindly provided by Mr. Alex Valentine) to avoid excessive clamping force with the usual alligator clamps. The cycling tests were performed at a current density of 0.14 mA cm^{-2}, with the entire area occupied of the battery properly considered.

4.3 Results & Discussions

4.3.1 Biphasic Electrode, Packaging, and Separator Inks

We first created biphasic, semisolid electrode inks based on LFP (cathode) and LTO (anode), respectively. The LFP/LTO electrochemical couple is chosen due to its low volumetric change [42,53] upon cycling and exceptional thermal stability, [45,54] which are especially important for fabricating ultrathick electrodes. [68] Ketjenblack (KB) carbon particles are incorporated as a second phase due to their high electronic conductivity and low percolation threshold. [147] To create biphasic electrode inks, these two particle populations are suspended and mixed sequentially in a 1M lithium bis(trifluoromethane) sulfonamide (LiTFSI)/ propylene carbonate (PC) solution, which has an ionic conductivity of 5 mS cm^{-1}. [148] Without additives, each particle population rapidly flocculates due to van der Waals interactions under such high ionic strength conditions. [149] To selectively stabilize electrode inks composed of 30 volume % LFP (or LTO) particles, we added a non-ionic dispersant, polyvinylpyrrolidone (PVP), at a concentration of 1 wt% with respect to the active material content (**Figure 4.2**). Notably, PVP-coated LFP and LTO particles remain stable at high (1M) salt concentrations during electrochemical charging and discharging. [38] However, under these conditions, the KB carbon particles (1.25 - 1.30 vol%) present in suspension remain attractive and form a percolative network. [150-153]

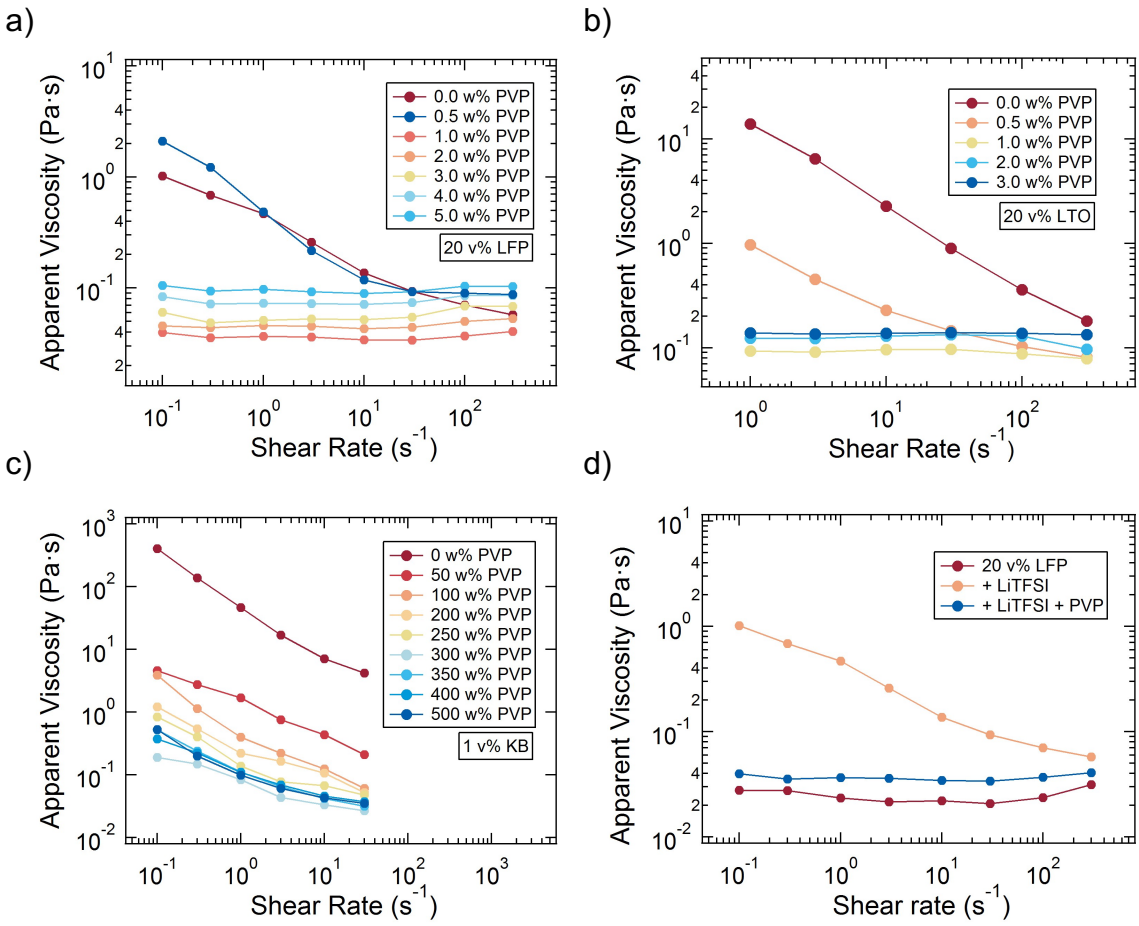

Figure 4.2: Attractive-to-repulsive transition PVP% for a) LFP (1%), b) LTO (1%), and c) KB (300%) in 1M LiTFSI/PC. d) Apparent viscosity vs. shear rate highlighting the effectiveness of PVP in sterically stabilizing LFP particles at high ionic strength (1M LiTFSI)

The effectiveness of PVP's steric stabilization is shown in **Figure 4.3**, where 2 vol% of KB carbon particles gradually transition from attractive (flocculated) to repulsive (dispersed) with increasing addition of PVP. The corresponding viscosity data (Figure 4.3f) shows the transition PVP% recorded the lowest viscosity values, matching the onset of dispersed KB carbon particles (Figure 4.3c).

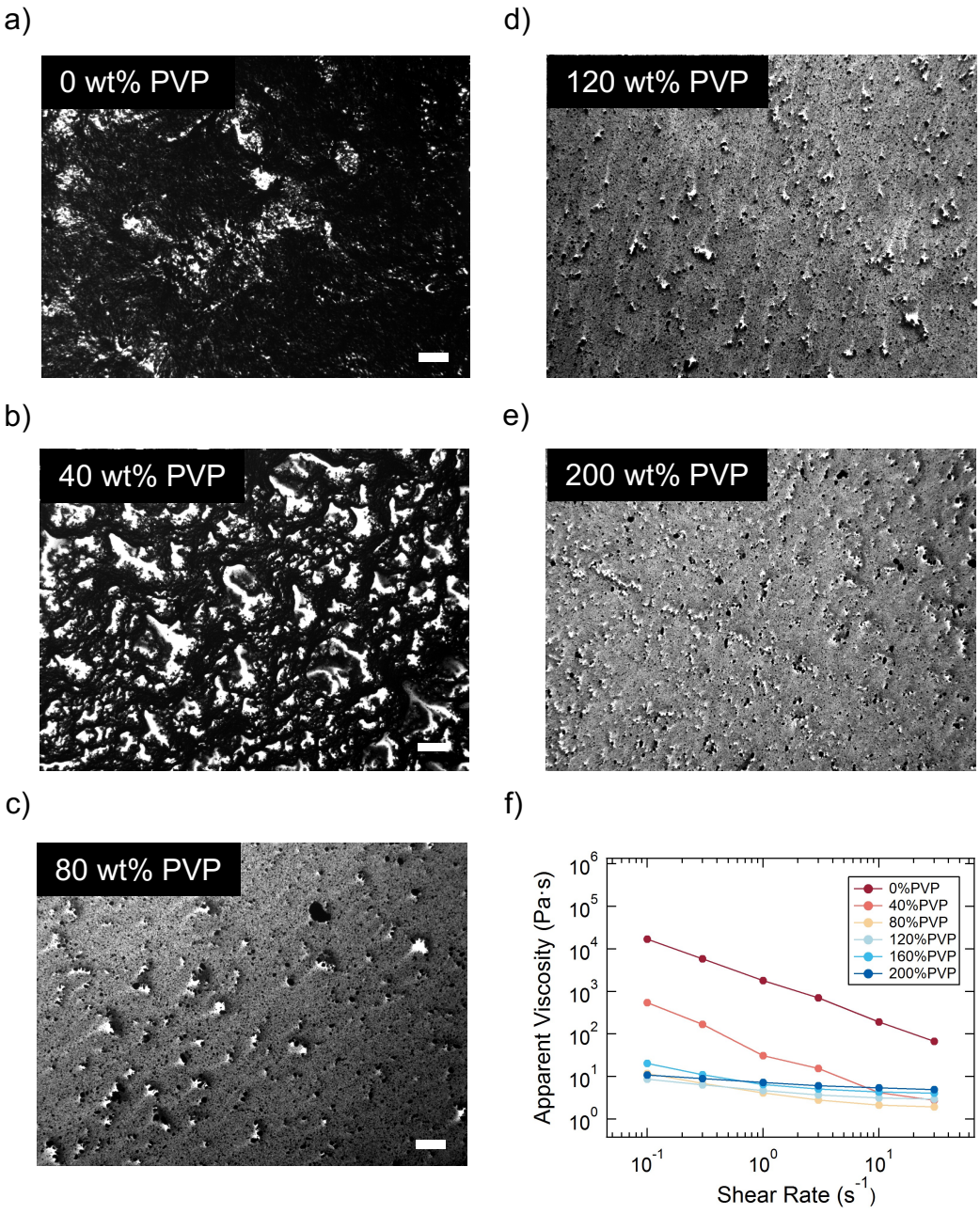

Figure 4.3: Micrographs of 2 vol% of KB nanoparticles in water showing the effectiveness of PVP steric stabilization at a) 0 wt% b) 40 wt% c) 80 wt% d) 120 wt% and e) 200 wt% (M_{PVP}/M_{KB}) with 80% identified as the attractive-to-repulsive transition PVP%. f) Apparent viscosity vs. shear rate of the respective KB suspensions showing supporting 80 wt% PVP as the transition concentration, leading to the lowest viscosity measured. [scale bars: 20 μm]

To optimize their performance, biphasic electrode inks must contain a high active material content coupled with an adequate conductive filler network to overcome the resistive nature of most electrochemically active Li-ion compounds. These electrode inks must also be tailored to exhibit the viscoelastic response required for direct ink writing. Their measured flow curves along with their shear elastic and loss moduli are shown in **Figure 4.4a-b**, respectively. These electrode inks are strongly shear thinning, which facilitates their flow through fine deposition nozzles (≥ 100 μm in diameter). At a characteristic (printing) shear rate of 1 sec^{-1}, the apparent viscosity for LFP and LTO are 6.27 kPa·s and 1.75 kPa·s, respectively. The corresponding viscoelastic storage (G') and loss moduli (G'') are provided in Figure 4.3b. We find that both electrode inks behave predominantly as elastic solids ($G' >> G''$) with respective G' values of 1.59 MPa and 1.25 MPa, and shear yield stress (τ_y) values of 3.96 kPa and 1.33 kPa for LFP and LTO inks indicating that a percolated network of carbon particles exists within each system. Hence, once these inks exit the nozzle and return to a zero-shear condition, they rapidly solidify and retain their filamentary shape.

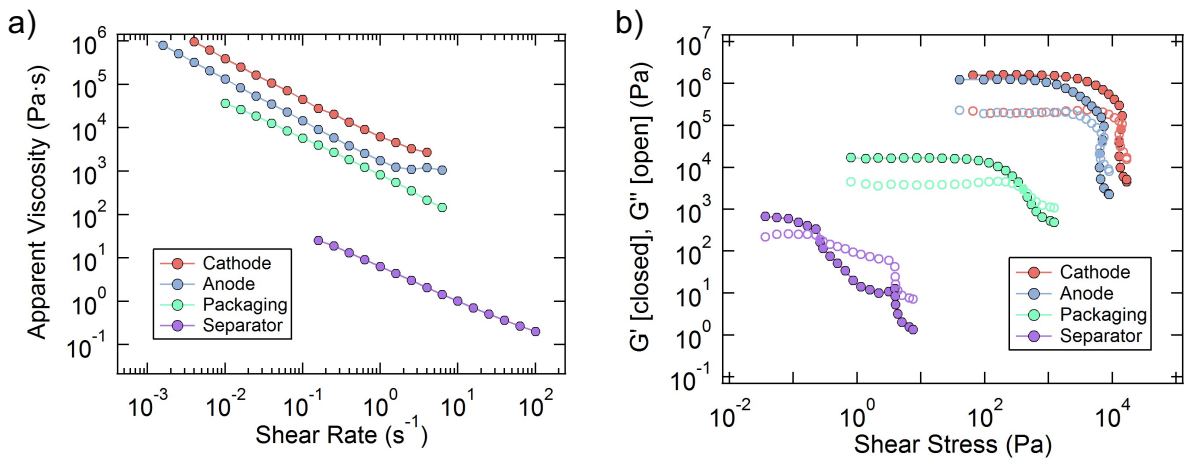

Figure 4.4: a) Apparent viscosity as a function of shear rate and b) elastic (G') and loss (G'') moduli of the four functional inks: cathode, anode, packaging, and separator.

Next, we explored the effects of active material content on the electrical conductivity and microstructure of these biphasic electrode inks. To facilitate imaging, a model biphasic ink is created with varying volume fraction of repulsive silica particles, $\phi_{repulsive}$ of 0 to 0.3, at a fixed volume fraction of attractive conductive carbon particles, $\phi_{attractive}$ of 0.015. As observed in **Figures 4.5,** the presence of repulsive particles alters the structure of the attractive carbon particle network. In the absence of repulsive particles, the attractive network consists of large, dense clusters that surround open regions filled with solvent and salt species. Upon adding repulsive particles, the attractive carbon particle network becomes more homogenous, favoring the formation of more tenuous, linear chains with fewer bonds between carbon particles. Essentially, the repulsive particles frustrate the formation of attractive particle bonds thereby yielding aggregated systems that are kinetically trapped in a more structurally uniform state.[107,109,154] The concomitant rise in electronic conductivity with increasing $\phi_{repulsive}$ reflects the observed microstructural evolution within these biphasic inks (Fig. 4.5a). As the conductive network becomes more

homogeneous at a fixed $\phi_{attractive}$, there are more pathways for transporting electronic current within the biphasic electrode suspensions.

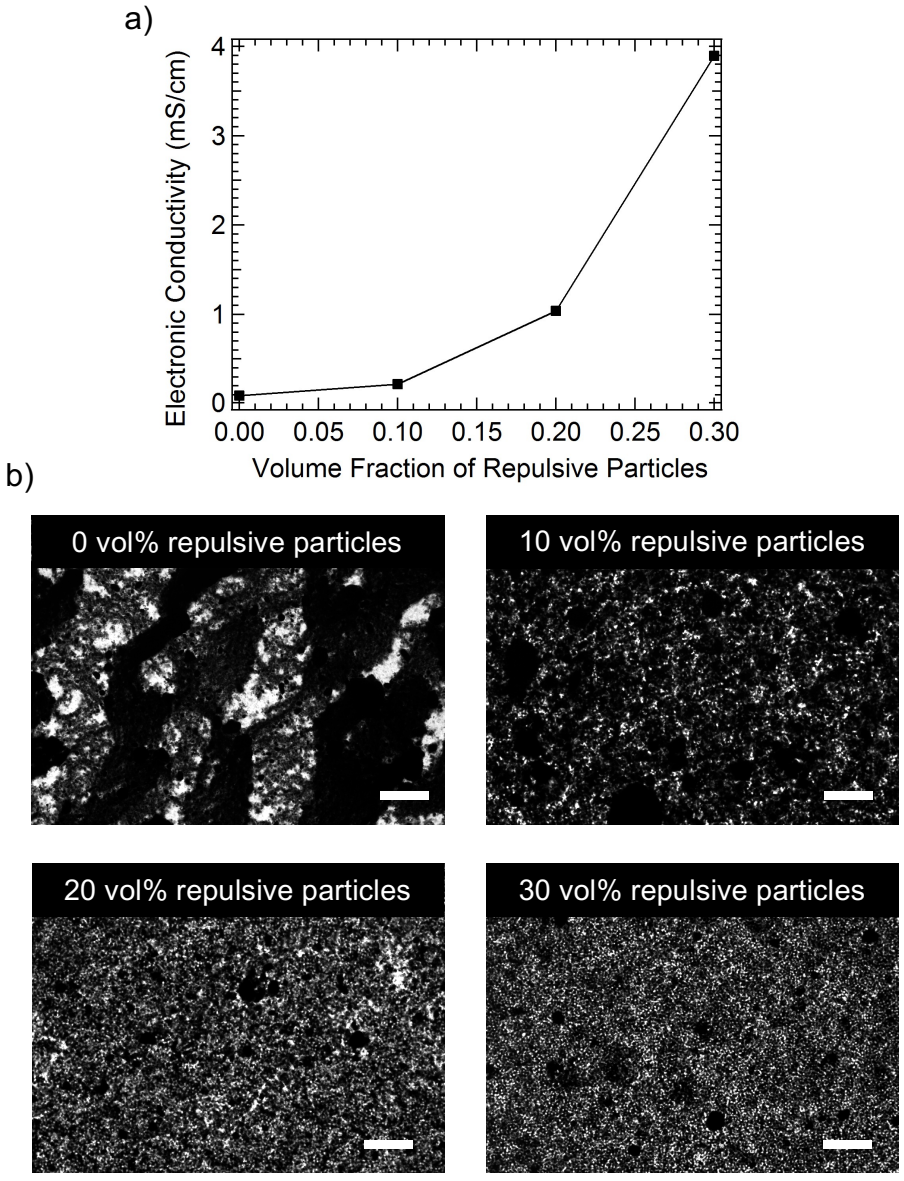

Figure 4.5: a) Electronic conductivity data [inset: proposed aggregation phase diagram for the attractive particles in a biphasic system] and b) micrographs of attractive KB (1.5 vol% in water-glycerol solution) suspension as a function of increasing vol% (0 →30) of repulsive, PVP-stabilized SiO_2 particles (index-matched) [scale bars: 20 μm]

To facilitate the fabrication of fully 3D printed LIBs, we produced UV-curable composite inks that serves as the packaging and separator materials.[155] Both of these inks are tailored to exhibit the desired shear thinning and viscoelastic responses required for direct writing (Fig. 4.4a-b). The packaging ink is composed of a UV-curable epoxy-SiO_2 (4 vol%), which must bond to the current collector and itself during the printing process. After UV curing, it must provide a protective shield to the active electrodes within printed LIBs. The separator ink is composed of UV-curable ethoxylated trimethylolpropane triacrylate (ETPTA), Al_2O_3 particles, electrolyte (1M LiTFSI/PC) and photo-initiator.[155] The Al_2O_3 nanoparticles are dispersed using a nonionic dispersant, Triton X-100 (TX-100). Since a thin separator layer is desired, this ink possesses an apparent viscosity and shear elastic modulus that is several orders of magnitude lower than the electrode inks.

4.3.2 Electrochemical Performance of Ultrathick Electrodes

To investigate electrode thickness effects, we carried out AC impedance measurements on LFP/LTO Swagelok cells with thin (0.1 mm) and ultrathick (1 mm) electrodes. As expected, their bulk (x-intercept) and charge transfer (semi-circle size) resistances are higher for the thick electrodes (**Figure 4.6a**). [8] At low frequencies, the ultrathick electrodes also exhibit a lower slope, where diffusion is limited by mass-transfer. Based on DC ohmic measurements, the cathode and anode electrodes exhibit an electronic conductivity of 13 and 12 mS cm^{-1}, respectively (**Figure 4.6**), which is more than two-fold higher [156] than the ionic conductivity of the electrolyte (5 mS cm^{-1} for 1M

LiTFSI/PC) [148]. Their high electronic conductivities are achieved at low carbon particle volume fraction due to their efficient microstructural distribution (Figure 4.5).

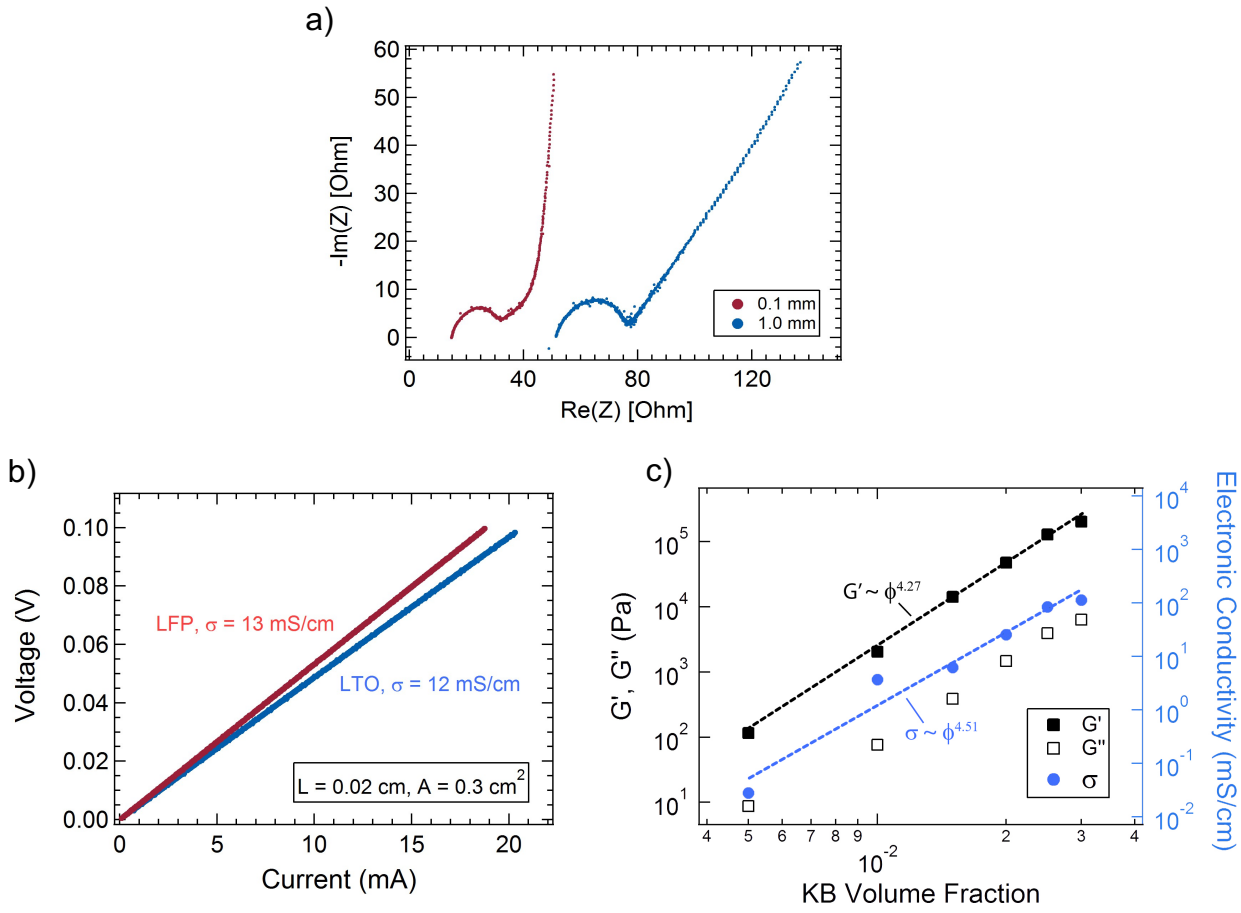

Figure 4.6: a) AC impedance data comparing LFP/LTO Swagelok cells with 0.1 and 1.0 mm electrodes showing thicker electrodes having higher impedance. Sufficiently high electronic conductivity of the 3D printable cathode (LFP) and anode (LTO) inks measured through DC characterization. b) Low KB percolation threshold showing power-law increase in elastic modulus and electronic conductivity from volume fraction as low as 0.005.

Cyclic voltammetry measurements reveal that these ultrathick electrodes exhibit a much higher (~10x at low scan rate) peak current, albeit with broader redox peaks and peak-to-peak potential-differences, owing to slower reaction kinetics (**Figure 4.7**). [157]

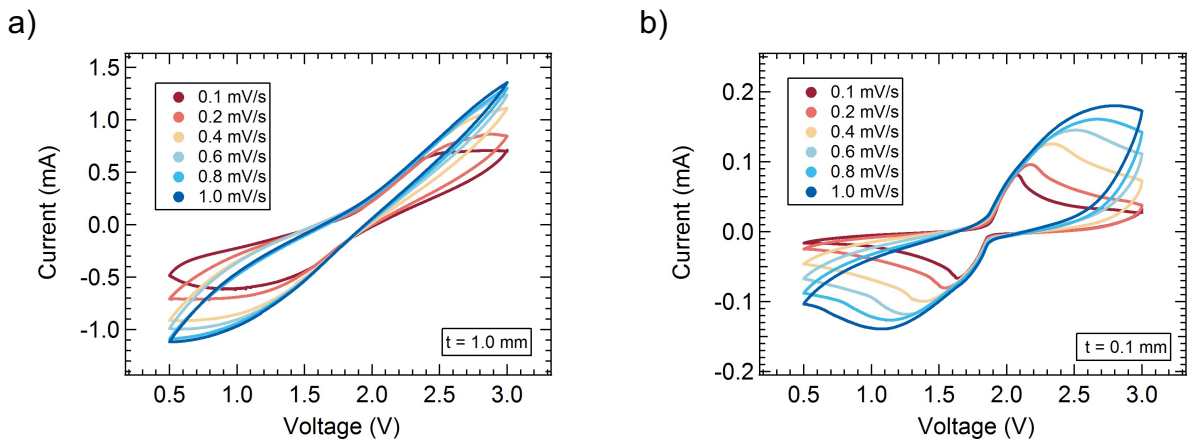

Figure 4.7: Cyclic voltammetry data of a) thick (1.0 mm) and b) thin (0.1 mm) electrodes at varying scan rates (0.1 mV s^{-1} → 1.0 mV s^{-1}) showing thicker electrodes having higher current responses.

Both thin and ultrathick electrodes exhibit excellent Coulombic efficiencies (near unity) and satisfactory areal capacities over several months of continuous cycling (**Figure 4.8a,b**). While the ultrathick electrodes delivered more than 10x the areal capacity compared to their thin counterparts, their energy efficiency falls off considerably with increasing cycle number, matching well to their increasing voltage polarization (Figure 4.8d). Hence, LIBs with ultrathick electrodes are better suited for applications that require less charge/discharge cycling.

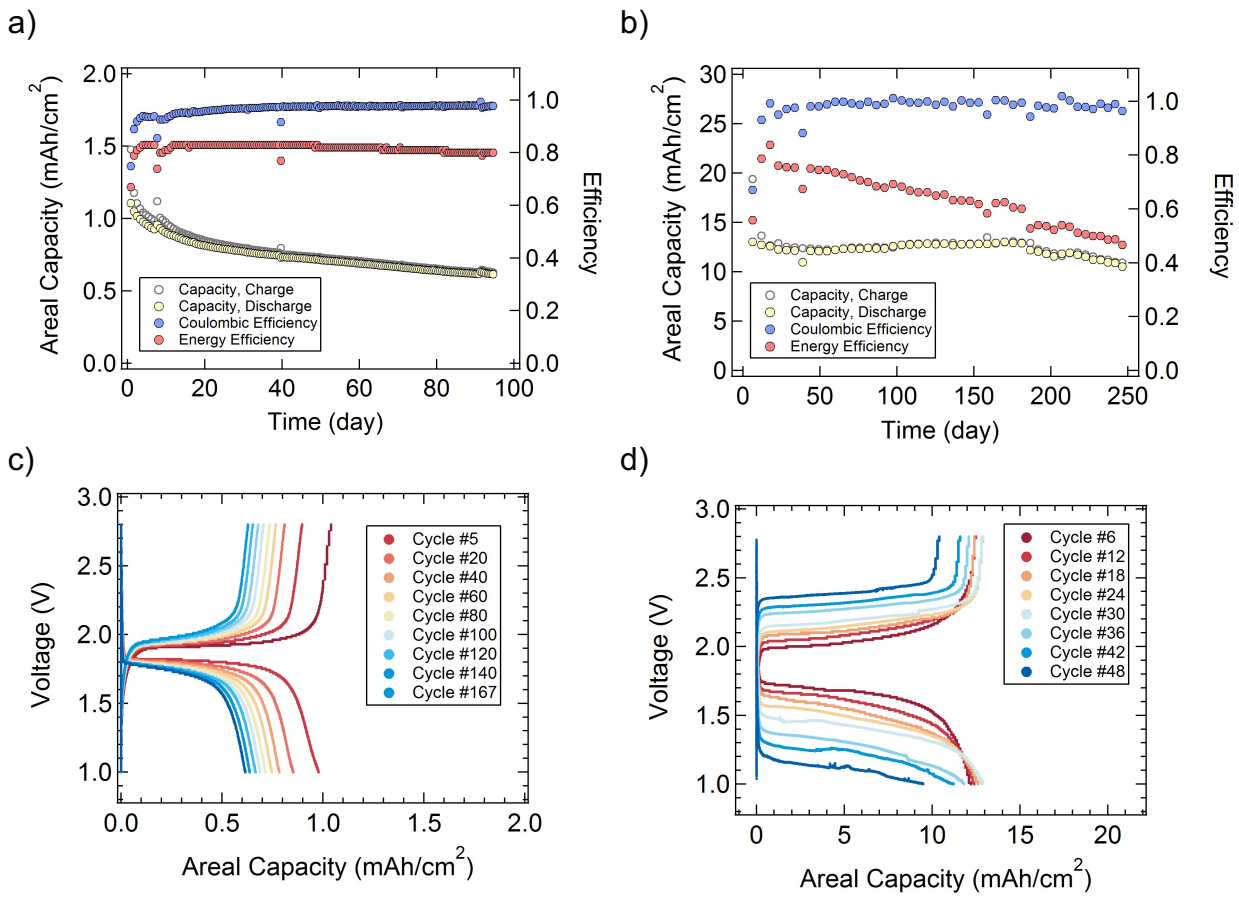

Figure 4.8: Cycle Life of LFP/LTO Swagelok cells at 0.2 mA cm^{-2} with a) thin (0.1 mm) and b) thick (1.0 mm) electrodes showing steadily high Coulombic efficiencies for both electrode thicknesses, but steadily declining energy efficiency for the thick electrode test cell. Cycling curves at selected cycles for c) 0.1 mm and d) 1.0 mm electrodes

Self-discharge characteristics are also important especially for intermittent, low power applications. The open circuit voltage for a full LFP/LTO cell with 1 mm electrodes is plotted as a function of extent of discharge at a current density of 0.2 mA cm^{-2} (**Figure 4.9**). After 20 days, we observed a 0.9% drop in capacity due to self-discharge, which suggests that these LIBs have a shelf life of roughly 6 years (100% capacity loss).

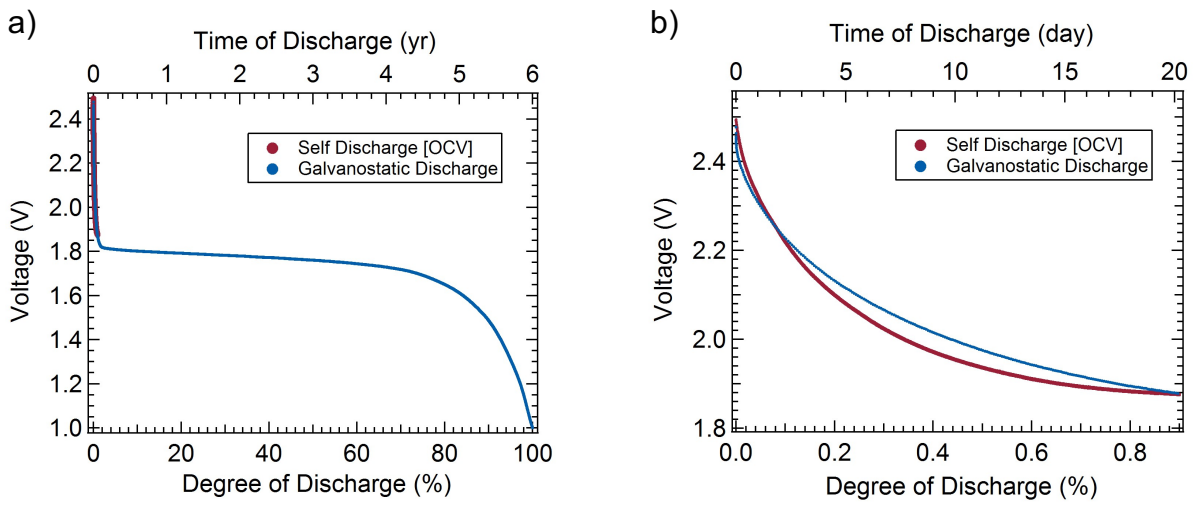

Figure 4.9: a) Self-discharge data measured over 20 days of a LFP/LTO Swagelok cell with 1.0 mm electrodes showing the battery would last 6 years before the battery completely die out. b) Zoomed-in version of the self-discharge curve for the recorded 20 days. [the galvanostatic discharge curve used for comparison in the self-discharge plot is 1 mm thick LFP/LTO Swagelok cell discharged at 0.2 mA cm^{-2}]

Next, we carried out rigorous galvanostatic cycling tests with Swagelok cells using standardized stainless steel current collectors with thin Celgard separator films (25 μm) to assess the impact of electrode thickness from 50 μm (represents commercial LIBs [63]) to 1 mm on cycling performance at current densities varying from 0.2 to 2.0 mA cm^{-2}. **Figure 4.10a** shows the expected trend of increasing areal capacity with increasing electrode thickness at 0.2 mA cm^{-2}, with the 50 μm and 1 mm cells (LFP loading of 108 mg/cm^2) delivering ~1 mAh cm^{-2} and ~14.5 mAh cm^{-2}, respectively. The superior areal capacity of ultrathick electrodes is also observed at 2.0 mA cm^{-2} (**Figure 4.10b**).

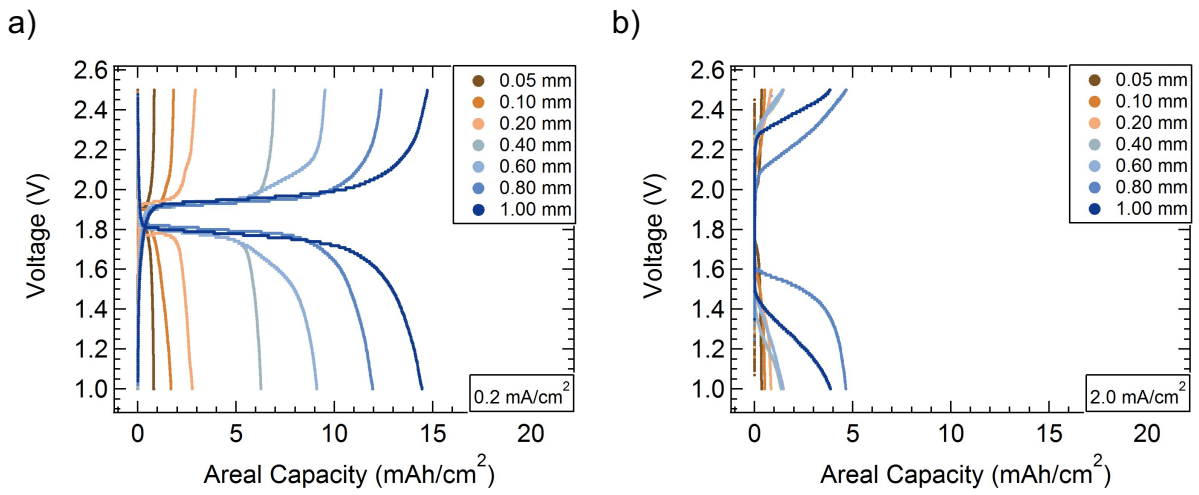

Figure 4.10: Areal capacity data of LFP/LTO Swagelok cells showing thicker electrodes delivering higher areal capacities at both a) low (0.2 mA cm^{-2}), and b) high (2.0 mA cm^{-2}) current densities.

Similar trends are observed at other current densities (**Figure 4.11**), suggesting 1 mm electrodes deliver the highest areal capacity over the thickness range investigated, except above 1.8 mA cm^{-2}, where 800 µm thick electrodes perform best.

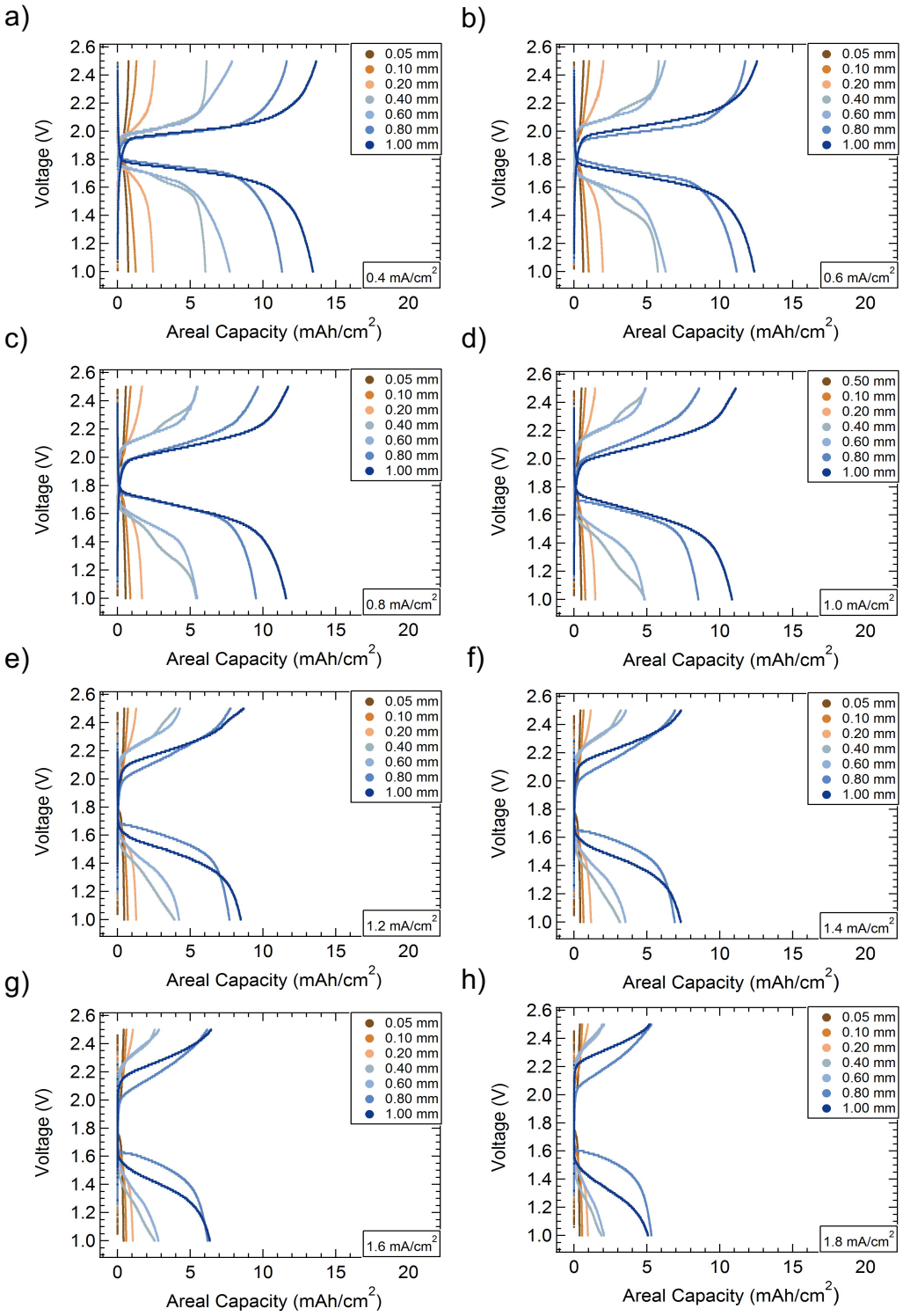

Figure 4.11: Areal capacity at varying electrode thicknesses (0.05 mm → 1.00 mm) at current densities a) 0.4 mA cm^{-2}, b) 0.6 mA cm^{-2}, c) 0.8 mA cm^{-2}, d) 1.0 mA cm^{-2}, e) 1.2 mA cm^{-2}, f) 1.4 mA cm^{-2}, g) 1.6 mA cm^{-2}, and h) 1.8 mA cm^{-2} showing thicker electrodes deliver higher areal capacity at all the current densities experimented.

The high-rate performance of thick electrodes [8,69] is notoriously poor due to longer ion diffusion distances and accelerated local depletion of Li ions at the electrolyte-active particle interfaces. However, we find that the normalized capacity ($Q_{discharge}/Q_{theoretical}$) as a function of current density exhibited nearly the same trend independent of electrode thickness (**Figure 4.12a**). We attribute this observation to both the efficient distribution of active and conductive particles within these electrodes[106,158,159] as well as their high electrolyte content. [63,69,71] From the cycling data, electrodes of varying thickness exhibit a Coulombic efficiency of nearly unity regardless of the cycling rate (**Figure 4.12b**). The observed energy loss (**Figure 4.12c**) is primarily due to the increased overpotential from chemical polarization and heat generation, [8,17,70] which is expected for ultrathick electrodes due to their inherently slower diffusion kinetics and increased bulk resistance. The Ragone plot, shown in **Figure 4.12d**, clearly indicates that full LFP/LTO cells ultrathick electrodes exhibit superior areal energy density, while largely retaining the areal power density of thin electrodes.

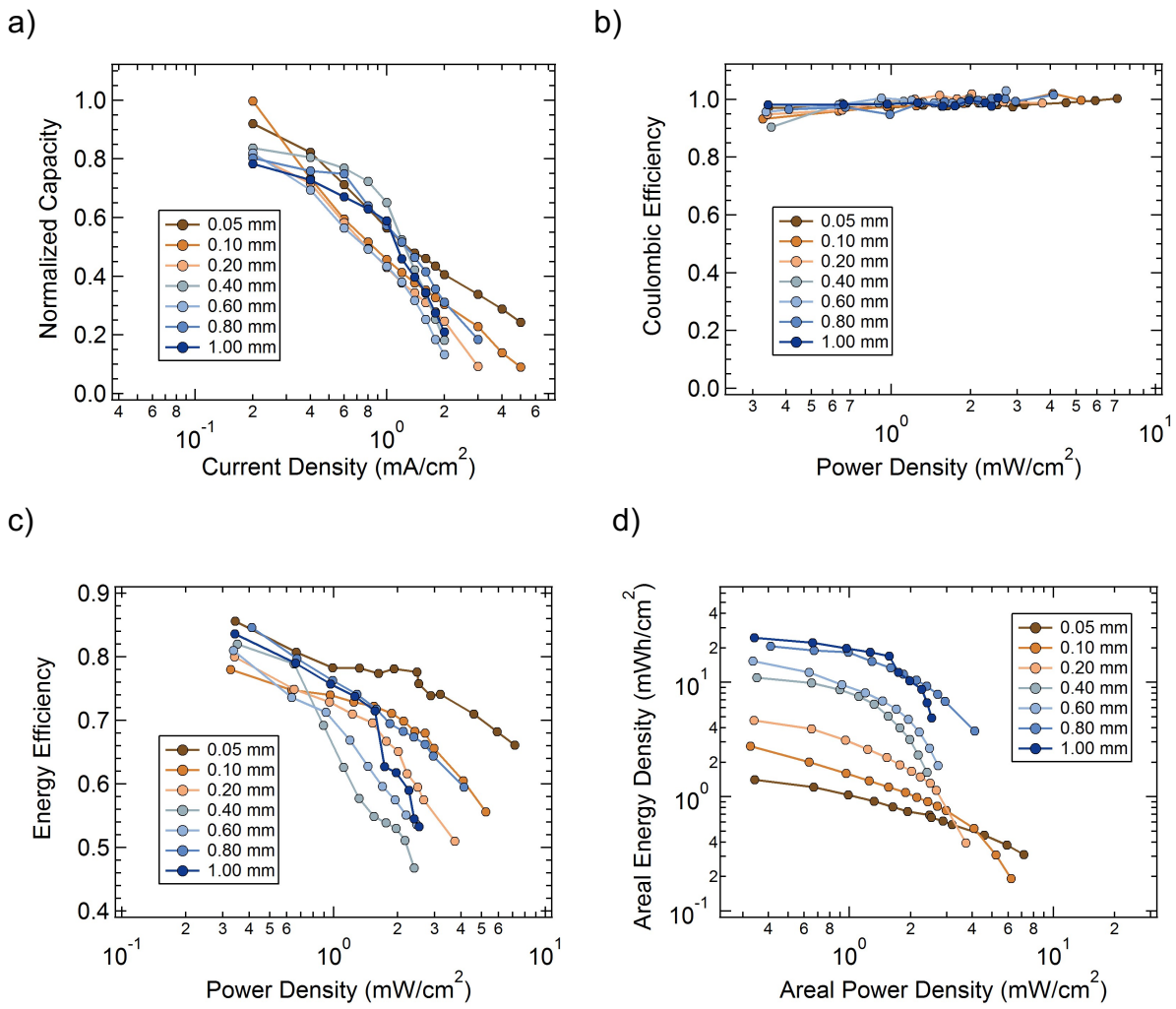

Figure 4.12: a) Normalized capacity vs. current density at varying electrode thicknesses (0.05 mm → 1.00 mm) showing similar rate of decay. b) Coulombic efficiency, c) energy efficiency, and d) energy density (Ragone plot) as a function of power density at varying electrode thicknesses (0.05 mm → 1.00 mm) showing consistently high Coulombic efficiency with all electrode thicknesses, more significant energy efficiency decay for the thicker electrodes, and higher areal energy density for the thicker electrodes.

4.3.3 Electrochemical Performance of Fully 3D Printed and Packaged LIBs

To further explore their electrochemical performance, we created fully 3D printed and packaged LIB with ultrathick electrodes (1 mm) in a customized design. Specifically, square donut cells were produced with an outer border (L = 10 mm, W = 10 mm, H = 2.5 mm) that surrounds an inner, open region (L = 6 mm, W = 6 mm, H = 2.5 mm) (**Figure 4.13a-b**). The volumetric and gravimetric electrode content within these printed LIBs are 54 vol% and 63 wt%, respectively (**Figure 4.13c-d**). They are capped on the top and bottom with current collectors that are laser-cut into the desired geometry from a thin glassy carbon sheet. To our knowledge, this is the first time that glassy carbon is used as current collector despite its high electrical ($3.5\times10^{-3}\ \Omega\bullet$cm) and thermal (~17.5 W m^{-1} k^{-1}) conductivity, lightweight and low gas permeability. [160] In addition, these laser-cut glassy carbon current collectors remain flat, ensuring uniform contact with the printed electrode inks.

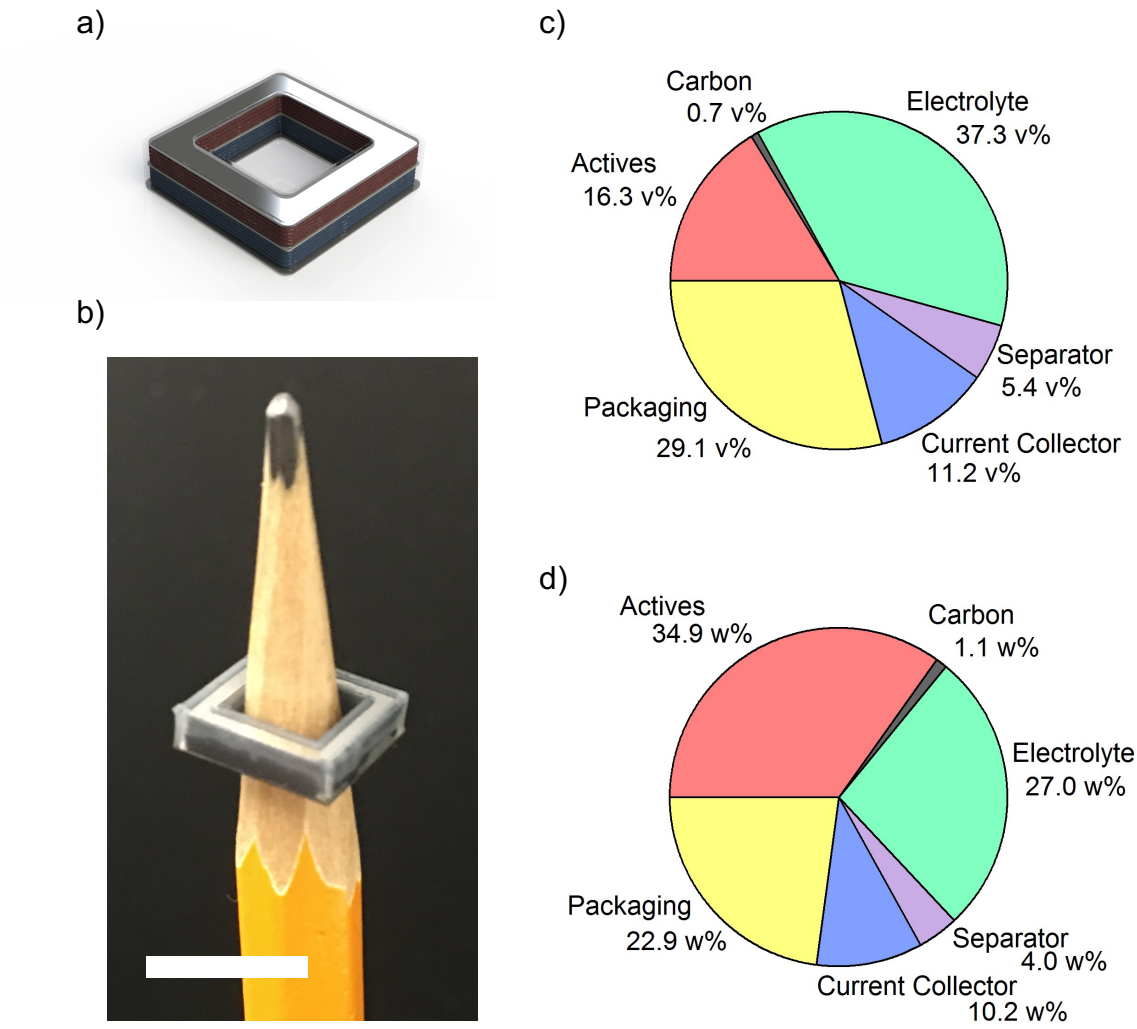

Figure 4.13: a) Schematic and b) digital photograph of the 3DP LIB (1 cm × 1 cm × 2.5 mm with a 6 mm × 6 mm through hole at the center). [scale bar = 1 cm] c) Volumetric and d) Gravimetric distribution of components of the 3DP LIB.

Prior to characterizing the performance of fully printed and packaged LIBs, we collected continuous cycling data for a LFP/LTO Swagelok cell with 0.1 mm electrodes using glassy carbon as the current collectors (**Figure 4.14**). This full LFP/LTO cell exhibited excellent cycle life with high Coulombic efficiency.

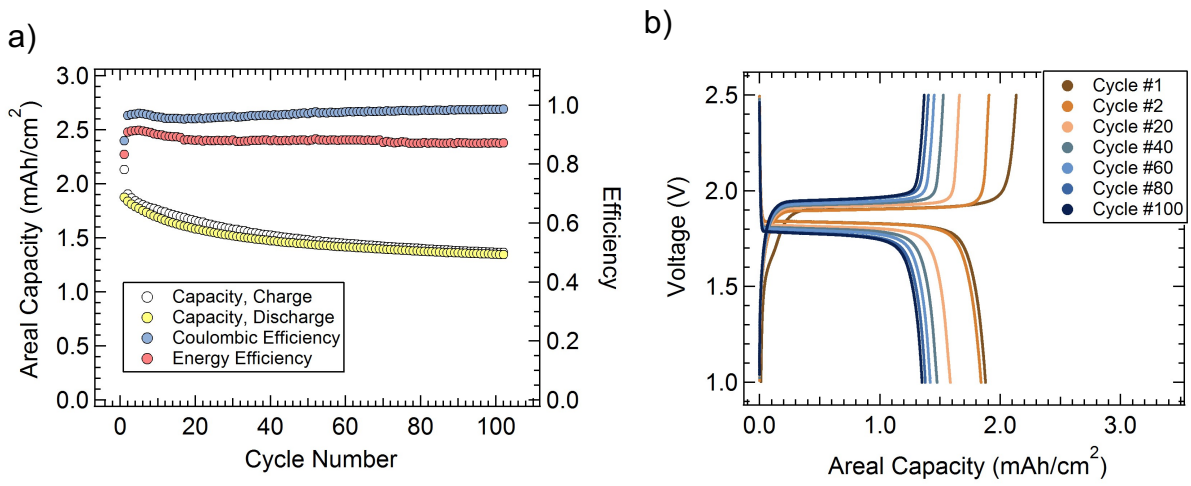

Figure 4.14: a) Areal capacity vs. cycle number and b) cycling curves of selected cycles of cycle life characterization of LFP/LTO Swagelok cell with glassy carbon current collectors with 0.1 mm electrodes cycled at 0.2 mA/cm².

Next, we cast and UV cured a 100 μm layer of the composite separator from which a circular disk is punched (**Figure 4.15a**). We then replaced the commercial Celgard separator used in all previous cycling experiments with our printable composite separator. Again, the cycling performance of a LFP/LTO Swagelok cell with 100 μm electrodes indicates that satisfactory capacity, Coulombic and energy efficiencies are achieved with minimal capacity fade over 20+ cycles (**Figure 4.15c-d**).

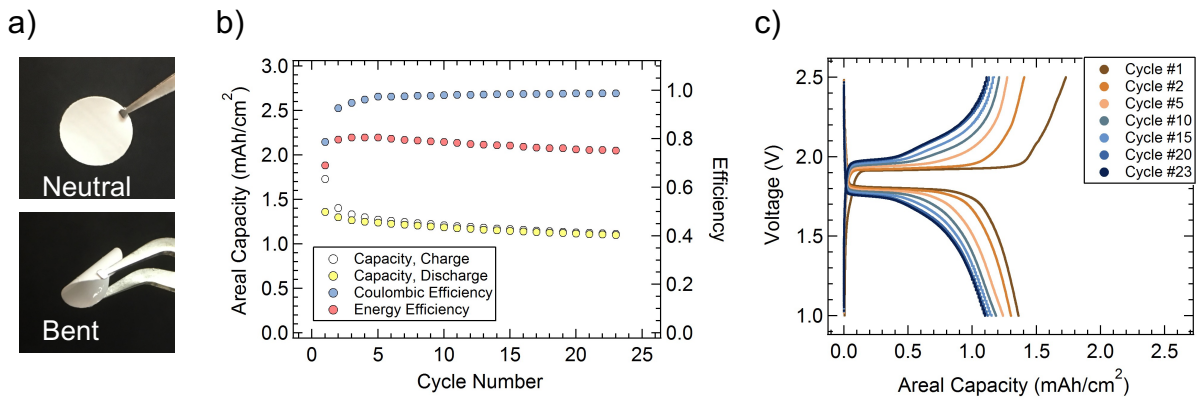

Figure 4.15: a) Digital photographs of a disk of UV-cured, casted separator film in neutral (top) and bent (bottom) configurations. b) Areal capacity vs. cycle number and c) cycling curves of selected cycles of cycle life characterization of LFP/LTO Swagelok cell with UV-cured composite separator with 0.1 mm electrodes cycled at 0.2 mA cm^{-2}.

As a final step, we characterized the electrochemical performance of fully 3D printed and packaged LIBs composed of ultrathick LFP/LTO electrodes, customized separator and packaging materials, and glassy carbon current collectors. These LIBs deliver an areal capacity of 4.45 mAh cm^{-2} at a current density of 0.14 mA cm^{-2}, with the entire area occupied of the battery properly considered. [161] (**Figure 4.16a**) The Ragone plot shows that our 3DP LIBs and 1 mm biphasic LFP/LTO Swagelok cell data compare favorably to values reported for other cell configurations (e.g., coin, Swagelok, and beaker cells) (**Figure 4.16b**).[8,37,73,75-78,104,146,162-166] Moreover, the fully 3DP and packaged LIB delivers impressive areal capacity, albeit lower than our unpackaged cell, which exceeds the values of several other (unpackaged) batteries. As one example, these LIBs exhibit a four-fold increase in performance over our unpackaged interdigitated electrode Li-ion microbattery reported previously[104]. **Figure 4.17** shows the 1.8V readout of a 3DP LIB in ambient conditions and a demonstration of it powering a red LED light. Given the lower

normalized capacity (43.35%), Coulombic efficiency (89%) and energy efficiency (67.7%) of these fully 3DP and packaged LIBs, further optimization is required to realize their full potential.

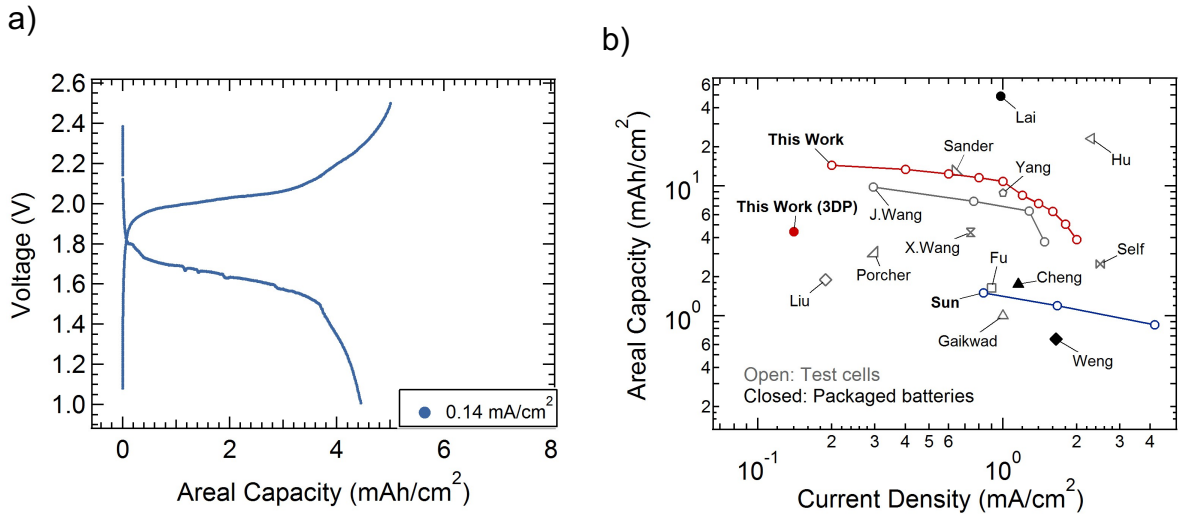

Figure 4.16: a) Cycling curves of the 2nd cycle at 0.14 mA cm^{-2} of the 3DP LIB with biphasic LFP and LTO electrodes, UV-cured composite separator, UV-cured composite packaging, and glassy carbon current collectors. b) Ragone plot comparing areal capacity vs current density of our LFP/LTO Swagelok cell with 1 mm electrodes and the fully packaged 3DP LIBs to reported literature values. [open symbol denotes reports demonstrated test cells with per-electrode areal capacity values; closed symbol denotes reports demonstrated fully packaged batteries with per battery areal capacity values]

a)

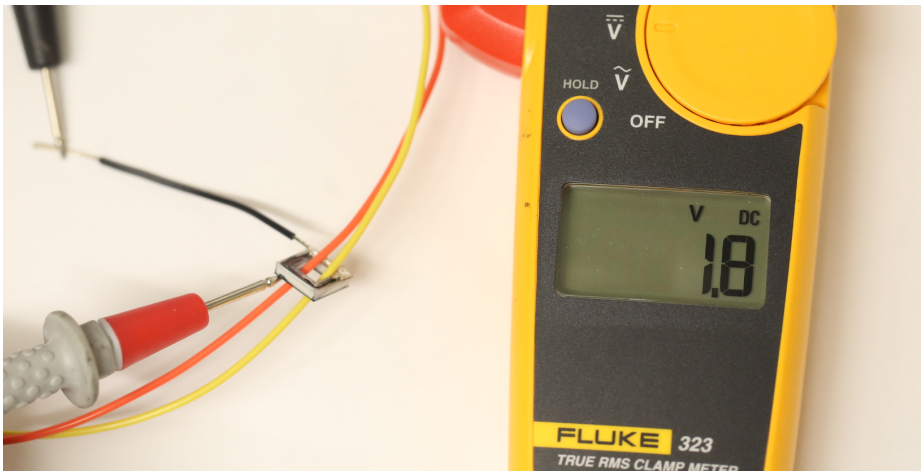

b)

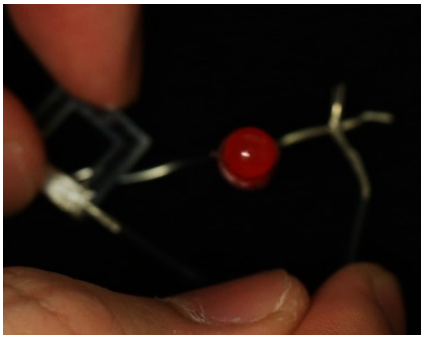

c)

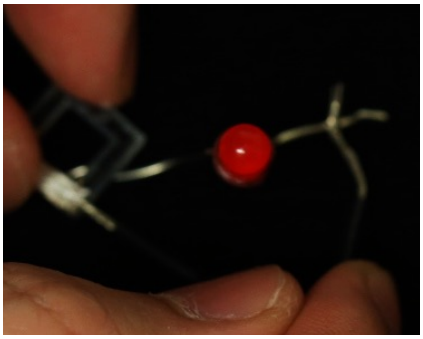

Figure 4.17: a) Voltage readout at 1.8V of a 3DP LIB in ambient condition. A red LED light b) disconnected (off) and c) connected (on) to a 3DP LIB.

4.4 Conclusions

In summary, we have demonstrated a new generation of 3D printed and packaged Li ion batteries with ultrathick, biphasic electrodes with high areal capacities in customized form factors. These packaged LIBs have areal capacities of 4.45 mAh cm^{-2} at 0.14 mA cm^{-2}, which corresponding full (unpackaged) cells can deliver 14.5 mAh cm^{-2} at 0.2 mA cm^{-2} (energy density ~20 mWh cm^{-2} at ~1 mW cm^{-2}). The ability to fabricate high performance LIBs in nearly arbitrary form factors opens up new avenues for designing wearable electronics, sensors, and other devices, in which batteries are directly integrated within functional elements, such as eyeglass frames, watch bands, or rings.

Chapter 5

Biphasic Electrode Suspensions for Li-Ion Semisolid Flow Batteries

This chapter has been adapted from the publication:

T.-S. Wei, F. Y. Fan, A. Helal, K. C. Smith, G. H. McKinley, Y.-M. Chiang, J. A. Lewis, "Biphasic Electrode Suspensions for Li-Ion Semi-Solid Flow Batteries with High Energy Density, Fast Charge Transport, and Low-Dissipation Flow" Adv. Energy Mater. 5, 1500535 (2015).

5.1 Introduction

The rapidly increasing deployment of wind and solar energy has resulted in an urgent need for a smarter, more efficient and reliable electric grid for load balancing.[15,16] Currently, the vast majority of energy storage occurs via pumped hydro installations,[3] a technology that is mature, cost effective, and efficient, but limited in applicability by geographic constraints.[3] Alternative modes of energy storage that can be deployed in a distributed manner include batteries, compressed air, thermochemical energy, and flywheels;[3] but today only a small fraction of the world's energy storage uses these technologies.

Flow batteries are of particular interest due to their decoupled energy and power, providing design flexibility especially at large scales.[110-112] Many flow battery chemistries, however, suffer from limited solubility and low nominal voltage, resulting in low energy

densities.[113] To overcome this, Duduta et al. developed the semisolid flow cell (SSFC),[7] in which traditional liquid catholytes and anolytes are replaced by attractive colloidal suspensions composed of Li-ion compounds. They also replaced traditional stationary current collectors with conductive carbon nanoparticle networks within the flowing suspensions. These suspensions, which take advantage of Li-ion battery's high energy density with flow battery's design flexibility, have been investigated both experimentally[7,40,167-169] and computationally.[40,115,170] Similar concepts have recently emerged for electrochemical flow capacitors[114] and polysulfide flow batteries.[39]

To fully optimize SSFCs, the flowing electrodes must have high active material content coupled with an adequate conductive filler network to overcome the resistive nature of most electrochemically active Li-ion compounds. However, as their solids content increases, their ability to flow readily dramatically decreases. The key to maximizing active material content while retaining satisfactory flowability and conductivity is to simultaneously tailor the respective interactions between all particle populations within these electrodes suspensions.[171]

In this chapter, we report the design and characterization of biphasic SSFC electrode suspensions with high energy density, fast charge transport, and low-dissipation flow. To create these biphasic mixtures[107,109] we specifically tailored the interactions between the active particles, $LiFePO_4$ (LFP), to be repulsive, the interactions between the conductive particles, Ketjenblack EC-600JD (KB), to be attractive, and the cross-interactions between LFP-KB to also be repulsive, similar to the procedures described in Chapter 4. These two particle populations are suspended and mixed sequentially in propylene carbonate (PC) with 1M of lithium bis(trifluoromethane)sulfonamide (LiTFSI). It is well known that colloidal particles will

rapidly aggregate when suspended in polar solvents under high ionic strength conditions due to van der Waals interactions.[149] Hence, we first introduce a non-ionic dispersant, polyvinylpyrrolidone (PVP), with appropriate amount to selectively stabilize the LFP particles fully, but not the KB particles. PVP has been shown to sterically stabilize colloidal particles in both aqueous[150-152] and non-aqueous[153] media leading to well dispersed suspensions. PVP is especially useful for SSFC electrodes as it confers stability even in systems with high (1M) salt concentrations that undergo electrochemical charging and discharging. We chose LFP due to its low volume expansion ($\square_{linear}$ ~ 2.2%)[42] when charged or discharged. We then added KB particles to the suspension, which form a conductive network at a low percolation threshold.[147,172]

We investigated the effects of biphasic suspension composition on the microstructure, flow behavior, and electrochemical performance of these SSFC electrodes. We show that well-dispersed (repulsive) LFP particles, surrounded by a percolating (attractive) KB network, enable quick and efficient charge transport that reduces overpotential during cell cycling. For comparison, we also create purely attractive LFP-KB suspensions in the absence of PVP and investigate their performance. Finally, we develop an analytical model that predicts the pressure drop needed for a given target current, based on these measured properties.

5.2 Experimental Methods

5.2.1 Biphasic Suspension Preparation

The active materials consist of a carbon-coated $LiFePO_4$ (LFP) powder (M121, Advanced Lithium Electrochemistry Co., Ltd., Taoyuan, Taiwan) with a mean particle size of 4 μm, a specific surface area of 13 $m^2\ g^{-1}$, and a density of 3.551 g cm^{-3} and carbon-

coated $Li_4Ti_5O_{12}$ (LTO) powder (LTO-1, BTR NanoTech Co., Shenzhen, China) with a mean particle size of 1.1μm, a specific surface area of 10.68 $m^2\ g^{-1}$, and a density of 3.539 g cm^{-3}. The conductive material consists of a Ketjenblack (KB) powder (EC-600JD, Azko Nobel Polymer Chemicals LLC (Chicago, USA) with a mean particle size ranging from 30 – 100 nm, a specific surface area of 1400 $m^2\ g^{-1}$, and a density of 2.479 g cm^{-3}. SEM images in **Figure 5.1** show the size and morphology of the LFP, LTO, and KB particles. Lithium bis(trifluoromethane)sulfonamide (LiTFSI), propylene carbonate (PC) and polyvinylpyrrolidone (M_W = 40,000 g mol^{-1}) are acquired from Sigma Aldrich.

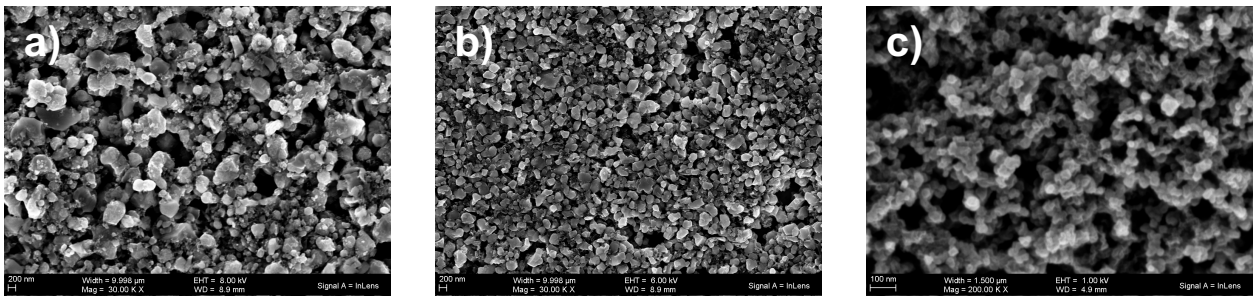

Figure 5.1 SEM images of (a) LFP (b) LTO and (c) KB particles

Electrode suspensions are prepared in argon-filled glovebox with moisture and oxygen content maintained under 0.5 ppm. All dry materials are heated at 120°C overnight under vacuum to remove moisture. First, 250 ml HDPE bottles are filled with 5 mm (200 g) and 0.5 mm (100 g) yttrium stabilized zirconia (YSZ) milling beads. Next, PC (50 g), PVP (0.3 g), and LFP or LTO powder (10 g) are added. The bottles are sealed and the suspensions are ball-milled under ambient conditions for 24 h. The suspensions are then filtered through 20 μm stainless steel sieve in the argon-filled glovebox. The filtered suspensions are then sealed and centrifuged at 12,500 g in the glove box for

approximately 1 h to collect the dispersed particles. After removing the supernatant, the dense sediment (typically 70 wt% solids) is collected and homogenized using a planetary mixer (Thinky AR-100). Additional PC and 1% PVP/PC solution are added, followed by ultra-sonication and homogenization. LiTFSI is then added to achieve a 1M electrolyte concentration. Finally, KB powder is added and homogenized. Suspensions containing either 0 or 0.1 PVP% are too flocculated to pass through a 20 μm sieve. Hence, those samples are prepared by planetary mixing of PC with PVP, followed by adding LiTFSI, then active material, and, finally KB.

5.2.2 Rheological Characterization

Rheological measurements are carried out on electrode suspensions of varying composition using a torsional rheometer (Malvern Kinexus Pro) enclosed in an argon-filled glove box. Both steady shear viscometry and oscillatory shear tests are performed using the smooth parallel plate geometry (diameter of 20 mm; mean roughness R_q of 0.36 μm). All tests are performed at 25 °C, as regulated by a Peltier plate system. All samples are pre-sheared at 100 s^{-1} for 5 s prior to measurement and left to equilibrate until the normal force relaxes (~15 min). Steady shear viscometry tests are performed with decreasing applied shear rates, as described by Ovarlez et al.,[173] to ensure the existence of a simple yield stress for the material and to avoid possible transient shear banding. Following Yoshimura and Prud'Homme,[174] the same sample is tested at three different gap heights to probe and correct for slip effects. If the flow curves at different gap distances superimpose, the material does not slip. If gap-dependent rheology is observed, a correction is applied to extract the true shear rate applied on the sample at each value

of the applied stress. Oscillatory strain amplitude sweep tests are performed at a fixed frequency $\omega =$ 1 rad s^{-1} and used to extract their plateau shear elastic modulus.

5.2.3 Electronic Conductivity Characterization

Electronic conductivity is measured by the DC method, where the voltage is swept from 0 V to 0.15 V (Biologic VMP-3). The test cell used is a modified Swagelok cell with a cylindrical test geometry (6.35 mm wide, 200 μm thick) sandwiched by two stainless steel electrodes. Contact resistance between suspension and current collector is neglected in these measurements.

5.2.4 Static Cell Characterization

Static galvanostatic cycling measurements are performed in two-electrode Swagelok-type cells, using lithium metal foil (Alfa Aesar) as a counter electrode. Electrode suspensions are placed in a stainless steel rod with a 0.5 mm deep well, which is sputter-coated with gold. A porous polymer separator (Celgard) soaked with electrolyte is sandwiched between the electrodes. All electrochemical tests are performed using a Biologic VMP-3 potentiostat.

5.2.5 Flow Cell Characterization

The electrode suspensions are tested in a lab-scale half flow cell, with both the positive and negative sides consisting of a 1.5 mm x 1.5 mm x 20 mm electroactive region machined into a PVDF body. This region is metallized by sputter-coating with gold on the positive side. A lithium metal negative electrode is inserted into the region on the negative side, and the two halves are bolted together with a Celgard separator wetted with

electrolyte in between. Pumping is performed using syringe pumps (Cetoni) with glass syringes (Hamilton Co.), at a flow rate of 30 μL s^{-1}. A syringe is connected to each end of the flow channel; during flow, the suspension is pushed from one syringe, while simultaneously pulled into the other. Flow cell tests are performed in "intermittent flow" mode[115] in which the material in the electroactive region is fully charged or discharged, before another suspension aliquot in pumped in.

5.3 Results & Discussions

5.3.1 Microstructure of Electrode Suspensions

We first characterized the microstructure of both biphasic and purely attractive LFP electrode suspensions using nanoscale-computed tomography (nano-CT). The 3D reconstructed images and 2D slices of both systems are provided in **Figure 5.2**. Their respective compositions are 20LFP/1.25KB/0.3PVP and 20LFP/1.25KB/0PVP, where the numbers denote the volume percent of LFP and KB particles and weight percent of PVP (in solution) in each suspension. In the biphasic mixtures, which contain PVP-stabilized LFP particles (white) and KB particles (grey), the two particle populations are clearly more homogeneously distributed than their purely attractive counterparts, which do not contain PVP. These observations are in excellent agreement with prior findings, in which the repulsive particle population within model biphasic mixtures led to a more homogeneous attractive particle network composed of smaller clusters and voids.[107,109]

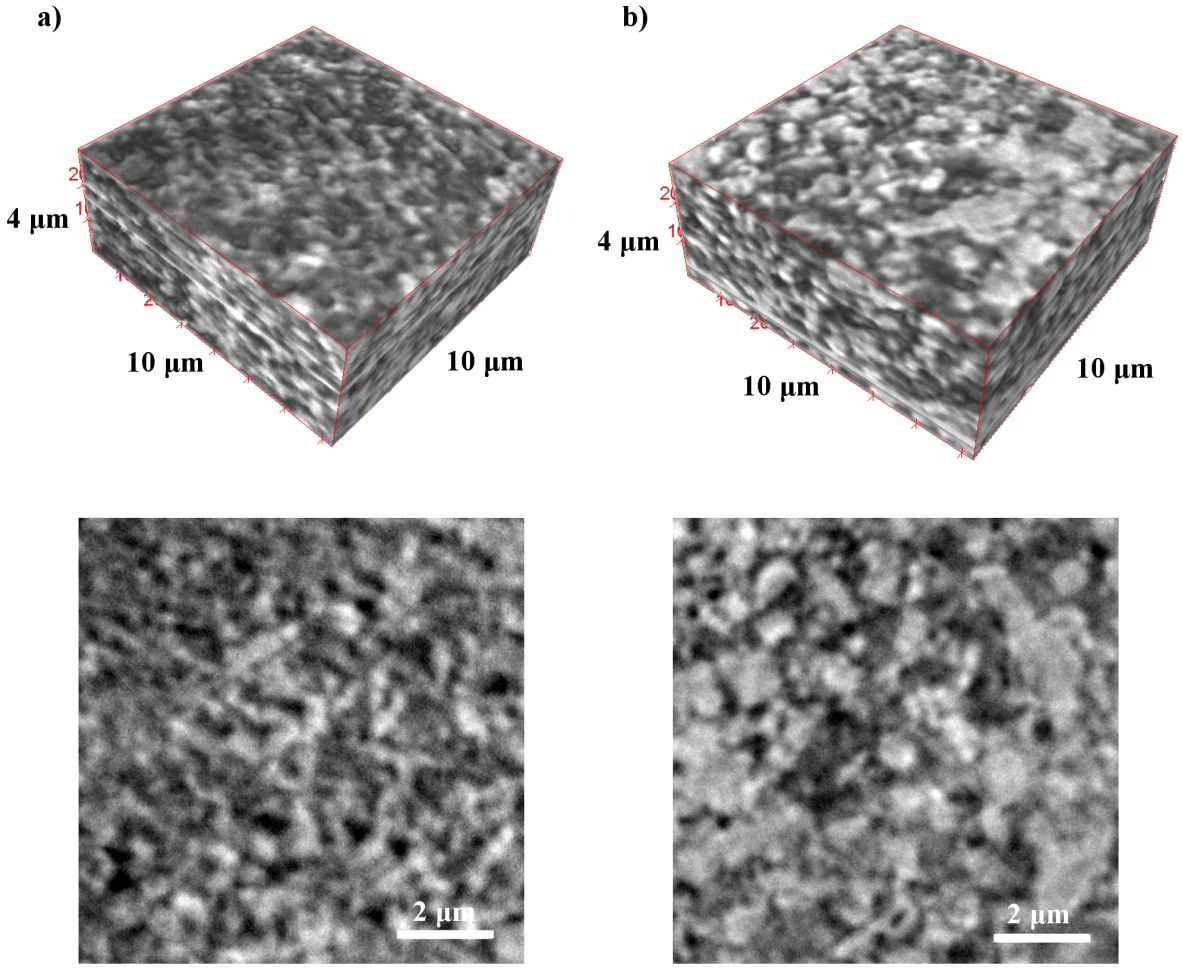

Figure 5.2 3D reconstructions (top) and 2D (x-y) slices (bottom) of nano-CT scans acquired on (a) biphasic (0.3wt% PVP) and (b) purely attractive (0 wt% PVP) electrode suspensions composed of 20 vol% LFP and 1.25 vol% KB.

5.3.2 Flow Behavior of Electrode Suspensions

To explore dispersant effects on flow behavior, we carried out both shear viscometry and oscillatory measurements on biphasic and purely attractive LFP electrode suspensions with the same compositions described above. Their measured flow curves and shear elastic and loss moduli are shown in **Figure 5.3a-b**, respectively.

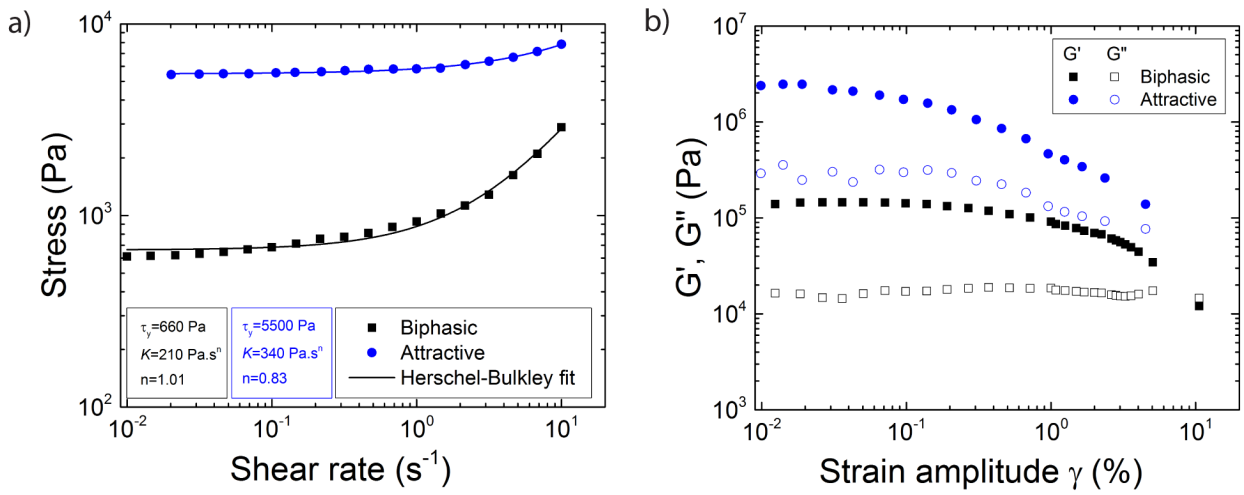

Figure 5.3 (a) Log-log plot of shear stress as a function of shear rate and (b) shear elastic storage (G´) and loss (G˝) moduli for biphasic (0.3 wt% PVP) and purely attractive (0 wt% PVP) electrode suspensions composed of 20 vol% LFP and 1.25 vol% KB. [Note: The lines in (a) represent fits of the Herschel-Bulkley model to the experimental data.]

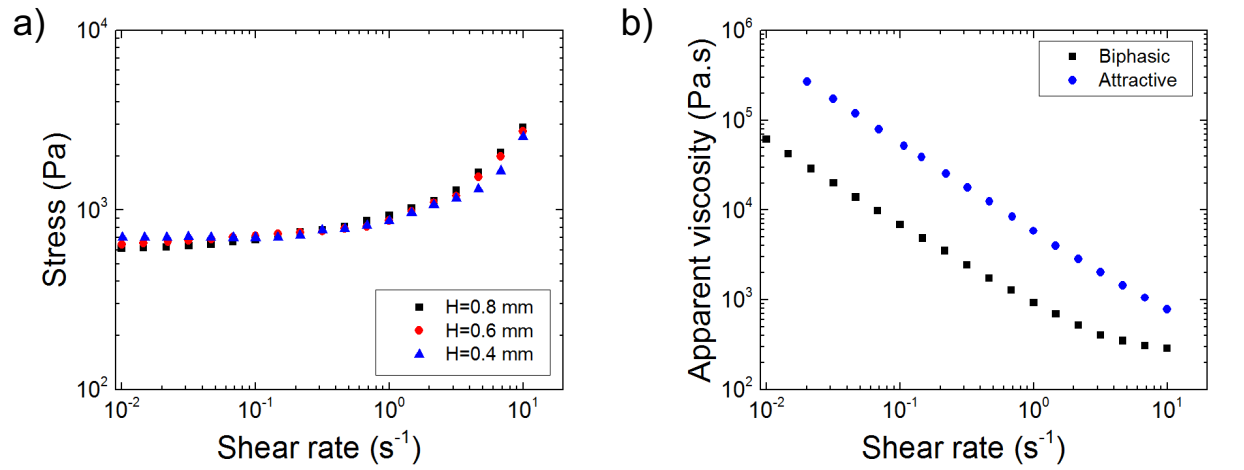

Figure 5.4 (a) Flow curves for the (a) biphasic LFP suspension (20LFP/1.25KB/ 0.3PVP) measured at 25 °C using different rheometer plate gaps (H = 0.8, 0.6 and 0.4 mm) against a smooth stainless steel surface. The overlapping results indicate no-slip boundary conditions at the surface. (b) Apparent viscosity as a function of shear rate for the biphasic (20LFP/1.25KB/ 0.3PVP) and purely attractive (20LFP/1.25KB/0PVP) LFP suspensions and [Note: The flow curves for the biphasic suspensions are slip-corrected, while those reported for the purely attractive suspensions are acquired at a rheometer plate gap of 0.8 mm. The latter data provide a lower bound on the true flow curves for these suspensions].

Concentrated colloidal suspensions are prone to wall slip effects during measurements.[174-177] The flow curves for biphasic LFP suspensions, which are slip-corrected[174], exhibit nearly identical behavior over multiple gap heights (**Figure 5.4a**). The inhomogeneity of the purely attractive electrode suspensions makes slip correction difficult. Their flow curve, which represents a lower bound, is acquired at the gap height of 0.8 mm. Both the biphasic and purely attractive suspensions exhibit a shearing thinning response (**Figure 5.4b**) and a shear yield stress (**Figure 5.3a**). However, the apparent viscosity of the biphasic system is nearly an order of magnitude lower than its purely attractive counterpart at a given shear rate. The same trend is observed for shear yield stress, which is an order of magnitude lower for the biphasic LFP suspension. Fits to the Herschel-Bulkley model[178]:

$$\tau = \tau_y + K\dot{\gamma}^n \quad (1)$$

where τ is the shear stress, τ_y is the shear yield stress, K is the consistency, $\dot{\gamma}$ is the shear rate, and n is the power law index, are shown in **Figure 3a** and regression to the experimental data gives an extrapolated yield stress of 0.6 kPa and 5.5 kPa for the biphasic and purely attractive LFP suspensions, respectively.

The corresponding storage (G') and loss moduli (G'') are provided in **Figure 5.3b** for the same biphasic and purely attractive LFP electrode suspensions. We find that both suspensions behave predominantly as elastic solids $\left(G' >> G''\right)$, indicating percolated network of attractive KB particles exist within each system. However, once again, we find that the biphasic suspensions exhibit an order of magnitude lower stiffness (0.145 MPa) than the purely attractive counterparts (2.46 MPa). We note that the design of electrolyte suspensions that exhibit a shear thinning response, a shear yield stress, and viscoelastic

behavior is advantageous for SSFC applications, because it reduces particle sedimentation, phase segregation, and unwanted mixing of charged and discharged regions.

This strategy can be readily applied to other active materials, such as lithium titanate (LTO). To demonstrate this, we created both biphasic and purely attractive LTO electrode suspensions with compositions of 20LTO/1.5KB/0.3PVP and 20LTO/1.5KB/0PVP, respectively. The slip-corrected flow curves for the biphasic LTO suspension **(Figure 5.5a)** exhibit nearly identical behavior over multiple gap heights. Both LTO suspensions exhibit a shear thinning response **(Figure 5.5b)**, a shear yield stress, and viscoelastic behavior (**Figure 5.6**). However, akin to the biphasic LFP suspensions, the apparent viscosity (at a given shear rate), shear yield stress and shear elastic modulus of the biphasic LTO suspensions are nearly an order of magnitude lower than their purely attractive counterparts. Moreover, Herschel-Bulkley fits give extrapolated shear yield stress values of 360 Pa and 4,100 Pa for the biphasic and purely attractive LTO suspensions, respectively.

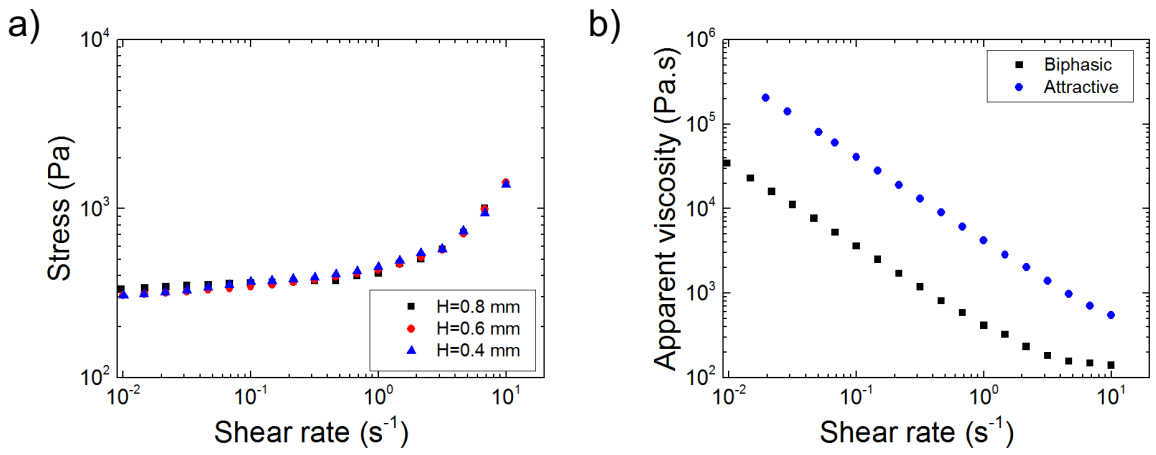

Figure 5.5 (a) Flow curves for the (a) biphasic LTO suspension (20LTO/1.5KB/0.3PVP) measured at 25 °C using different rheometer plate gaps (H = 0.8, 0.6 and 0.4 mm) against a smooth stainless steel surface. The overlapping results indicate no-slip boundary conditions at the surface. (b) Apparent viscosity as a function of shear rate for the biphasic (20LTO/1.5KB/0.3PVP) and purely attractive (20LTO/1.5KB/0.3PVP) LTO suspensions and [Note: The flow curves for the biphasic suspensions are slip-corrected, while those reported for the purely attractive suspensions are acquired at a rheometer plate gap of 0.8 mm. The latter data provide a lower bound on the true flow curves for these suspensions].

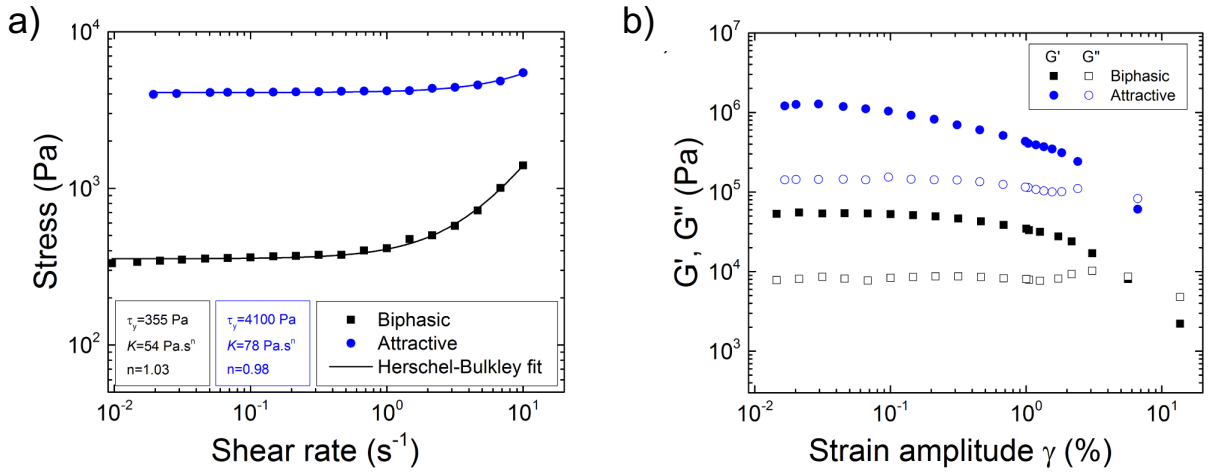

Figure 5.6 (a) Log-log plot of shear stress as a function of shear rate and (b) shear elastic storage (G´) and loss (G˝) moduli for biphasic (0.3 wt% PVP) and purely attractive (0 wt% PVP) electrode suspensions composed of 20 vol% LTO and 1.5 vol% KB. [Note: The lines in (a) represent fits of the Herschel-Bulkley model to the experimental data.]

5.3.3 Electronic Conductivity Measurements

To broadly explore the effects of suspension composition, we carried out electronic conductivity and oscillatory measurements on biphasic electrode suspensions of varying LFP, KB, and PVP content (**Figure 5.7**).

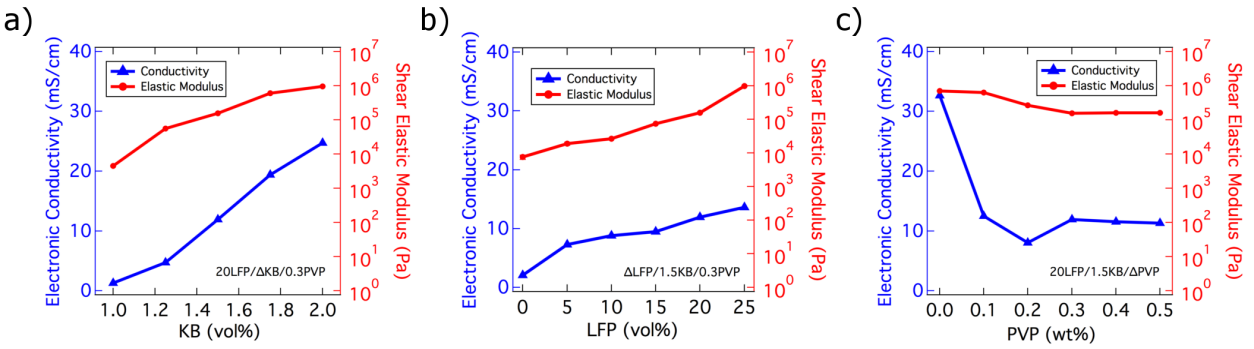

Figure 5.7 Plots of shear elastic modulus and electronic conductivity as a function of varying (a) KB (at 20 vol% LFP, 0.3 wt% PVP), (b) LFP (at 1.5 vol% KB, 0.3 wt% PVP), and (c) PVP (at 20 vol% LFP, 1.5 vol% KB) contents showing positive correlation between the two properties.

We first characterized biphasic suspensions with varying KB vol% composed of LFP (20 vol%) and PVP (0.3 wt%) (**Figure 5.7a**). We consistently observed a positive correlation between their electronic conductivity, shear elastic modulus, and KB content. Even at the lowest KB content (1 vol%) explored, these particles form a percolating network that gives rise to a measurable electronic conductivity and shear elastic modulus. However, upon increasing to 2 vol% KB, there is a power law growth in both electronic conductivity and shear elastic modulus (**Figure 5.7a**), indicating that that the interparticle bonds within this percolating particle network has dramatically increased. Next, we fixed the KB (1.5 vol%) and PVP (0.3 wt%) contents and explored the effects of

LFP (from 0 vol% to 25 vol%) on the electronic conductivity and shear elastic modulus of these biphasic electrode suspensions (**Figure 5.7b**). As observed in **Figure 5.2** as well as reported previously for model biphasic suspensions,[107,109] the presence of repulsive LFP particles alters both the long-range and local structure of the attractive KB network. In the absence of LFP particle, the attractive KB particle network consists of large, dense clusters that surround open regions filled with solvent and salt species. Upon adding repulsive LFP particles, the attractive KB particle network becomes more homogenous, favoring the formation of more tenuous, linear chains with fewer bonds between KB particles. The repulsive particles have significantly slower mobility than solvent molecules or ionic species. When randomly distributed amongst a population of attractive particles, the repulsive particles inhibit the formation of attractive particle bonds thereby yielding aggregated systems that are kinetically trapped in a more structurally uniform state.[107,109,154] The concomitant rise in both electronic conductivity and shear elastic modulus with increasing LFP content reflects this microstructural evolution within these biphasic suspensions (**Figure 5.7b**). Simply put, as the conductive network becomes more homogeneous at a fixed number density of attractive KB particles, there are more pathways for transporting electronic current within the electrode suspensions and the shear elastic modulus increases. We note that in the absence of attractive KB particles, the shear elastic modulus is indeed quite small (1.2 Pa), indicative of a structure-less liquid state expected for well-dispersed LFP suspension (20 vol% LFP, 0.3 wt% PVP). Finally, we fixed both the LFP (20 vol%) and KB (1.5 vol%) contents and varied the amount of PVP from 0 to 0.5 wt% to determine its effects on performance. Results show that once a critical amount of PVP (0.3 wt%) is introduced to the suspension to stabilize the particles, both electronic conductivity and shear elastic

modulus vary minimally with further addition of PVP (**Figure 5.7c**). The above data reveal that optimizing biphasic electrode suspensions for use in semisolid flow cell batteries is not straightforward. Both their ability to charge/discharge efficiently and flow readily through the flow cell is important. These criteria are often in conflict, since the KB network gives rise to both the desired electronic conductivity (which facilitates charge transfer) and a yield stress (which increases pumping pressure).[147,172]

5.3.4 Analytical Model

To identify suitable SSFC suspension compositions, we developed an electrode-scale model that incorporates efficiency and flowability criteria. To impose a constant electrochemical performance criterion, we require that all suspensions have the same round-trip voltage efficiency between charge and discharge. In all cases, the modeled cell is subjected to a current density i of 10 mA cm^{-2} with a current-collector length L_{cc} of 20 mm. For each suspension, the electrode thickness w is treated as an adjustable parameter that produces a voltage efficiency η_V of 90%, where η_V is defined as:

$$\eta_V = \left(\bar{\phi}_{eq} - \Delta\Phi\right) \Big/ \left(\bar{\phi}_{eq} + \Delta\Phi\right) \qquad (2)$$

where $\bar{\phi}_{eq}$ is the average open-circuit voltage of the cell, and $\Delta\Phi$ is the average polarization. We assume that the electrochemical reactions propagate via a planar front through the electrode's thickness, producing an average polarization that decreases as the effective electronic conductivity σ_{eff} and effective ionic conductivity κ_{eff} increase:

$$\Delta\Phi = iw\left(\kappa_{eff} + \sigma_{eff}\right) \Big/ \left(2\kappa_{eff}\sigma_{eff}\right) \qquad (3)$$

This model for polarization accounts for the series arrangement of ionic and electronic resistance in porous electrodes (see schematic in **Figure 5.8a**), and we have shown previously[13] that similar models approximate the time-averaged polarization incurred during the intermittent-flow mode (and provide a lower bound on polarization incurred during the continuous-flow mode), as predicted by more accurate flowing, porous-electrode models in the same work. This trend is shown in **Figure 5.8b** for suspensions with various loading levels of LFP.

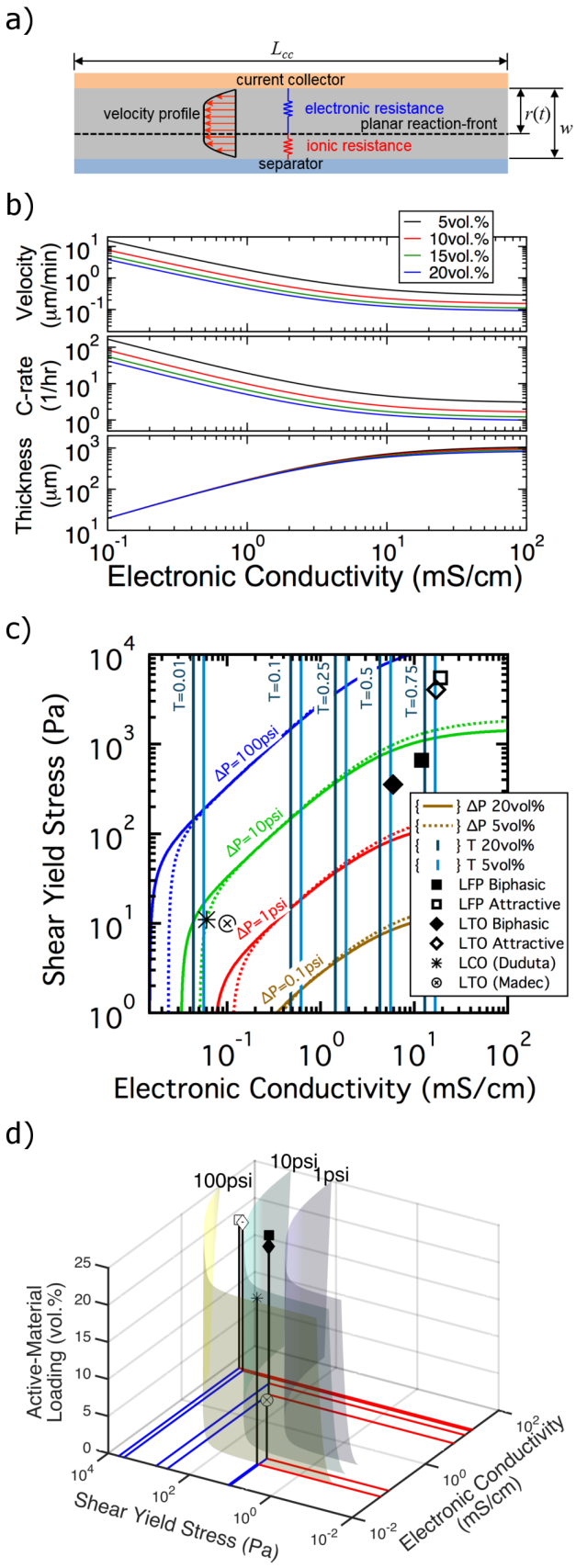

Figure 5.8 (a) A schematic showing the series arrangement of ionic and electronic resistance in porous electrodes used in the model (b) Analytical predictions of the electrode thickness, C-rate, and mean velocity as a function of electronic conductivity for biphasic and purely attractive LFP suspensions of varying composition, under the constraint of constant 90% voltage efficiency between charge and discharge (c) predicted pressure drop contours for suspensions with 20 vol% (solid lines) and 5 vol% LFP (dotted lines). [Note: The effective ionic conductivity is calculated for 1 mol L^{-1} LiTFSI in PC solvent, which has a viscosity of 8 mPa-s.[148] Contours of electronic transference number, defined as $T = \sigma_{eff} / \left(\sigma_{eff} + \kappa_{eff} \right)$, where σ_{eff} and κ_{eff} are effective electronic and ionic conductivity of the suspension, are also shown. (d) Surfaces of constant pressure-drop in the three-dimensional space of active-material loading, shear yield-stress, and electronic conductivity. The six data points represent the biphasic LFP suspension (20LFP/1.25KB/0.3PVP), the purely attractive LFP suspension (20LFP/1.25KB/0PVP), the biphasic LTO suspension (20LTO/1.5KB/0.3PVP), and the purely attractive LTO suspension (20LTO/1.5KB/0PVP) along with two reference samples reported by Duduta et al. (22.4LCO/0.6KB)[7] and by Madec et al. (7.9LTO/2.2KB).[167]

The model couples charge-transfer and rheology properties by accounting for the high flow velocities required to cycle thin electrodes at a given current density. The mean flow-velocity required to maintain stoichiometric conditions (where state-of-charge is consumed in one flow pass) increases as the electrode thickness decreases:

$$\bar{u} = iL_{cc}/(qw) \tag{4}$$

q is the volumetric charge-capacity of the suspension, which depends on the type and loading of electroactive material used. Because electrode thickness decreases with decreasing electronic conductivity, the mean velocity increases as electronic conductivity decreases. A Bingham-plastic rheology[179]:

$$\tau = \tau_y + \mu_p \dot{\gamma} \tag{5}$$

where μ_p is the plastic viscosity, is assumed to estimate the corresponding pressure drop ΔP, which increases with the flow's dimensionless Bingham number:

$$\frac{\Delta P w}{2\tau_0 L_{cc}} = 2Bn \Big/ \left(\sqrt{24Bn + 9Bn^2 + 144} - Bn - 12\right) \tag{6}$$

The Bingham number (a characteristic ratio of elastic-to-viscous stresses in the flow) is defined in terms of the fluid's yield stress τ_y and plastic viscosity μ_P:

$$Bn = \tau_y w \Big/ \left(2\mu_P \bar{u}\right) \tag{7}$$

With the variables defined, the model provides a contour plot as shown in **Figure 5.8c**, where the pressure drops can be estimated for suspensions according to their charge-transfer and rheology properties. By inserting in the measured electronic conductivity and shear yield stress values for our biphasic and attractive suspensions, it is found that the attractive suspensions require roughly ten-times the pressure drop. The predicted pressure drops for the biphasic suspensions (~1-10 psi) are similar to those

reported previously by Duduta et al.[7] and Madec et al.,[167] for suspension compositions of 22.4LCO/0.6KB and 7.9LTO/2.2KB, respectively. However, our biphasic LFP and LTO electrode suspensions exhibit electronic conductivities that are nearly two orders of magnitude higher, which allows for roughly 25 times thicker electrodes according to **Figure 5.8b**, greatly reducing the time-average pumping rate. Our biphasic suspensions also lead to higher areal capacities compared to suspensions with lower electronic conductivity or active material content, enabling longer discharge time at the same current density. Furthermore, the biphasic suspensions possess nearly optimal electronic transference numbers (**Figure 5.8c**), where electronic and ionic conductivities are of similar magnitude. These properties are ideal for maximizing cell cycling rates, while minimizing the shunt currents between multiple cells in a stack. [39,180] By contrast, the low electronic conductivities measured by Duduta et al.[7] and Madec et al.[167] would give rise to dramatic ionic shunt currents owing to their low transference numbers as show in **Figure 5.8c**, if electrodes of moderate thickness are employed (e.g. 100 μm ~ 1 mm). **Figure 5.8d** shows the surfaces of constant pressure-drop in the three-dimensional material-selection space defined active-material loading, shear yield-stress, and electronic conductivity; data points on the plot show the properties of materials developed in the present and previous works. Because volumetric charge-storage capacity is proportional to the loading of active material in semisolid suspensions, the vertical axis is a surrogate scale for energy-density. The plot reveals that biphasic suspensions are the only electrodes reported to date that simultaneously exhibit high energy density (i.e., high active-material loading), fast charge transfer (i.e., high electronic conductivity), and low-dissipation flow (i.e., low pressure drop).

5.3.5 Electrochemical Performance of Static Cells

To test electrochemical performance, a biphasic LFP suspension (20LFP/1.5KB/0.3PVP) is first cycled in non-flowing configuration in a modified Swagelok cell (**Figure 5.9**).

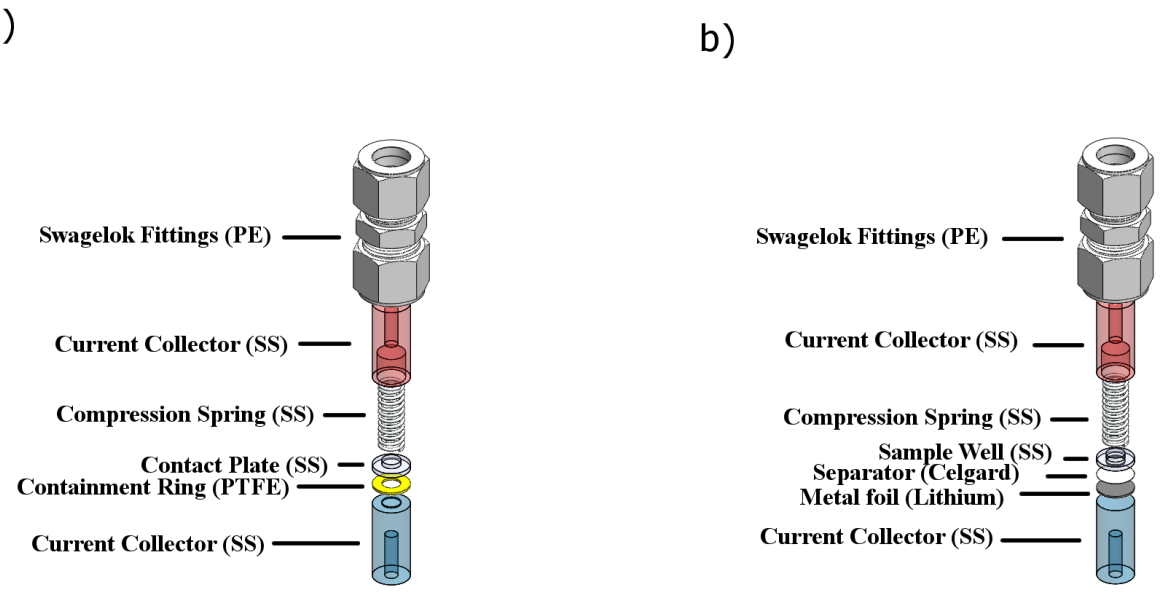

Figure 5.9 3D CAD images of the electrochemical measurement cells used for (a) electronic conductivity testing, (b) static galvanostatic cycling cell

The initial specific capacity of 129 mAh g^{-1} is obtained at a rate of C/8 (i.e. one complete charge or discharge in 8 hours), which is similar to prior results for semisolid flow electrodes.[7,40,181] Their capacity is stable for 100 cycles, with a capacity of 115 mAh g^{-1} on the 100th cycle, or a loss of 0.1% per cycle (**Figure 5.10a**). Capacity is roughly the same at a rate of C/4, but drops significantly at C/2. Notably, the biphasic suspensions have a two-fold higher LFP content compared to prior reported systems (typically ~10 vol%[40,168]). Hence, a C-rate of C/4 for a 20 vol% suspension represents a current

equivalent to C/2 with a 10 vol% suspension, or 1C with a 5 vol% suspension. **Figure 5.10b** reveals that polarization increases with cycle number, as given by the voltage differences between the galvanostatic charge and discharge curves, indicating that the capacity loss is due to impedance growth, rather than true capacity fading. Coulombic efficiency is consistently over 99% for the biphasic LFP suspension (20LFP/1.5KB/0.3PVP). We carried out similar measurements for a biphasic LTO electrode suspension (25LTO/2KB/0.8PVP) and measured a capacity up to 170 mAh g^{-1} at a rate of C/8, with Coulombic efficiencies exceeding 99% (**Figure 5.10c,d**). We would like to point out the performance of those biphasic electrode suspensions are not fully realized in this flow battery application since their solids loadings (20 vol% LFP, 25 vol% LTO) are intentionally held low to limit the pressure drop under 10 psi during flow operation (**Figure 5.8d**). In Chapter 4, biphasic electrode inks with solids loading as high as 30 vol% are developed for 3D printing of Li-ion battery electrodes with superior electrochemical performance.

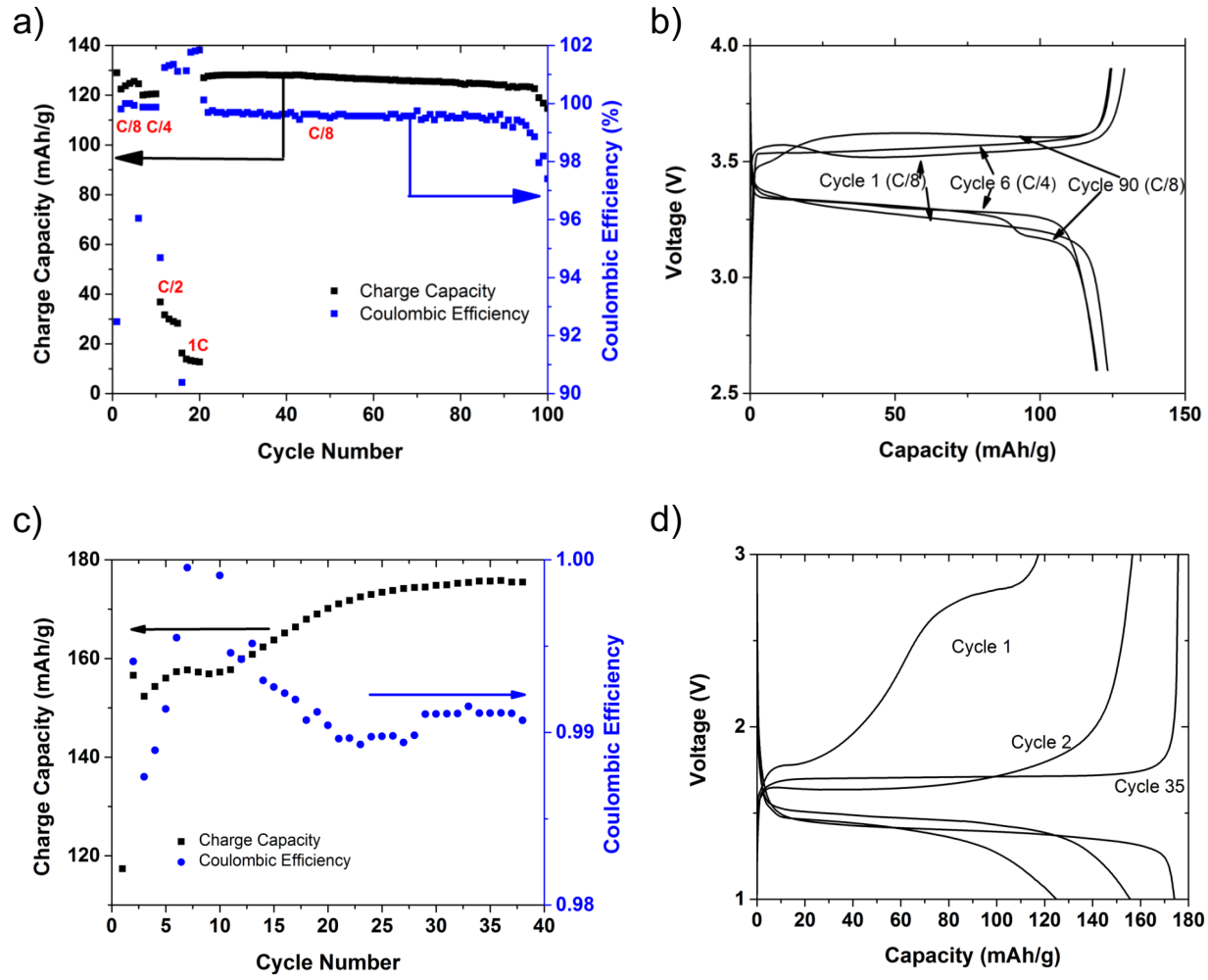

Figure 5.10 (a) Capacity and Coulombic efficiency as a function of cycle number for a biphasic LFP suspension (20LFP/1.5KB/0.3PVP) galvanostatically cycled vs. Li metal anode in a non-flowing Swagelok cell. (b) Selected cycles obtained for the same LFP. Cycles 1 and 90 are performed at C/8; Cycle 6 is performed at C/4. (c) A biphasic LTO suspension (25LTO/2KB/ 0.8PVP) cycled galvanostatically between 2.5 V and 1.0 V, with the first cycle at C/5 and subsequent cycles at C/8 rate and (d) Selected cycles for galvanostatic cycling of the same suspension: cycle 1 is performed at C/5, while the other cycles are performed at C/8.

5.3.6 Electrochemical Performance of Flow Cells

To further investigate their performance, the optimized biphasic LFP suspensions are tested in a lab-scale half-flow cell (**Figure 5.11a**) against a Li metal negative electrode, using the intermittent flow mode. In this approach, the volume of material inside the

electroactive region, referred to as an aliquot,[115] is fully charged or discharged under non-flowing condition, and then the aliquot is quickly replaced with a fresh one using computer-controlled syringe pumps. This protocol is known to reduce inefficiency due to pumping[170] and electrochemical[115] losses. In this test, an amount of suspension equal to twice the channel volume is charged and discharged (**Figure 5.11b**).

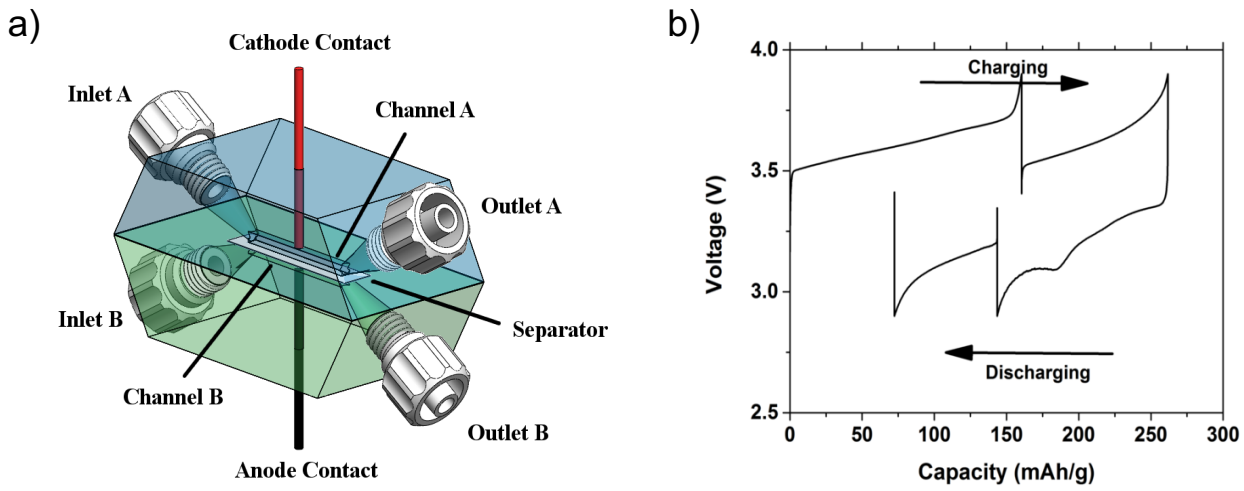

Figure 5.11 (a) Intermittent-flow cycling of the biphasic LFP suspension (20LFP/1.25KB/0.3PVP) in a lab-scale flow cell. Two consecutive aliquots are first charged, then the second one is discharged, and finally the first aliquot is discharged. The flow channel is 20mm long and has a 1.5 mm x 1.5 mm square cross-section. (b) 3D CAD image of the flow galvanostatic cycling cell.

An overall Coulombic efficiency of 72.3% and energetic efficiency of 63.1% are obtained, as compared to first cycle Coulombic efficiency of 91% in the static cell. To our knowledge, this is the highest LFP concentration used in a semisolid flow battery electrodes, and additional performance improvements are expected upon further optimizing flow conditions.[115] The overall capacity of LFP in the suspension is 131 mAh g^{-1} (equivalent to 93 Wh L^{-1}), at a current density of 1.67 mA cm^{-2}, or a rate of C/9 per

aliquot. During the charge and discharge processes, the capacity of the first aliquot is larger than that of the second one, which may be due to electroactive zone extension,[115,180] in which the catholyte's high electronic conductivity allows material slightly outside the channel to be cycled.

To further improve the performance of SSFCs, we suggest replacing the non-ionic surfactant PVP with Triton X-100 (TX100)[167] for better long term cyclability. We suspect PVP degrades and is consumed during cycling, as suggested by the 3-electrode cyclic voltammetry experiments performed **(Figure 5.12)** on pure 1M LiTFSI/PC electrolyte, one with 10 wt% PVP added, and one with 10 wt% TX-100 added.

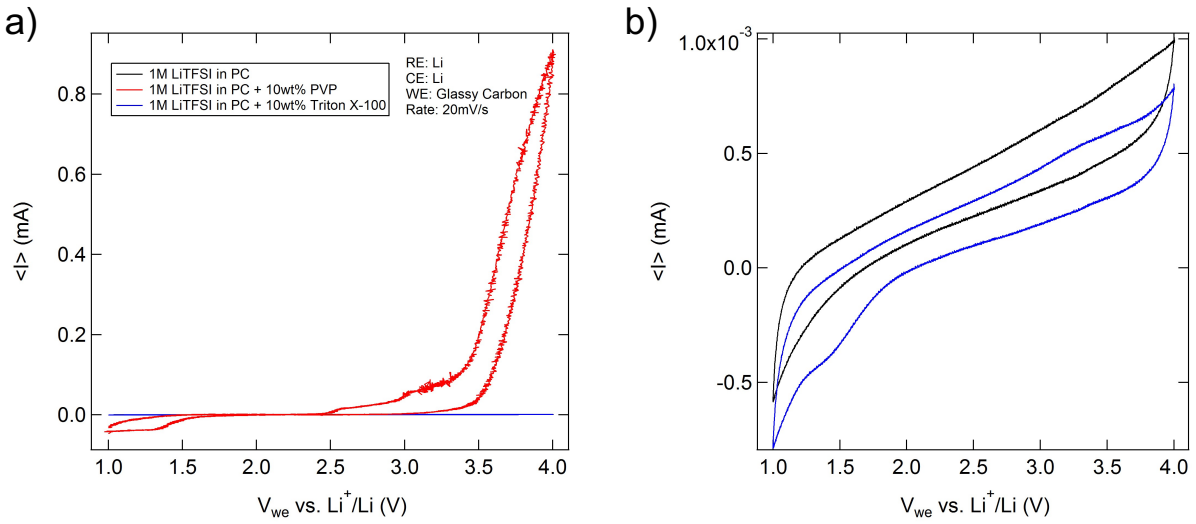

Figure 5.12 (a) 3-electrode cyclic voltammetry data of pure 1M LiTFISI in PC electrolyte compared to one with 10 wt% PVP added and one with 10 wt% TX-100 added. (b) a zoomed in view comparing the pure electrolyte and the one with TX-100 added.

Within the relevant voltage range (1 ~ 4V vs. Li^+/Li), PVP degradation translates into excess current as shown in **Figure 5.12a**, whereas the electrolyte with TX-100 added showed a nearly identical CV curve to the pure electrolyte sample (**Figure 5.12b**). Since

the presence of finely tuned addition of surfactant is critically responsible to biphasic suspensions, PVP degradation can be detrimental to the suspension's flowability and homogeneity, potentially rendering the flow battery non-operational.

Quite recently, Hopkins et. al. have reported a cost and performance model that compares static and flow batteries. [182] They find the cost advantage of SSFC versus static Li-ion batteries diminishes from ~25% to ~10% when suspension loading increases from ~10 vol% to 40 vol%. Since SSFCs require high solids loading to provide superior energy density compared to traditional flow batteries, there is less incentive to deploy scalable flow battery infrastructure over commercial Li-ion batteries. Moreover, Li-ion batteries are becoming less expensive every year due to their growing use renewable energy storage[1], electric vehicles[4], and portable electronic devices.

Further challenges associated with SSFCs include state of charge (SOC)-dependent rheological and electrochemical properties, since the ionic strength , hence, flowability are expected to change with SOC, as will the electronic conductivity of LTO.[183] Looking ahead, rheo-electrical studies[147,184] coupled with real-time tomography [185-188] would allow one to better understand how shear-induced disruption of the attractive KB particle network[189] influences electrical conductivity.

5.4 Conclusion

In summary, we have created a new class of biphasic electrode suspensions for semisolid flow cell batteries that possess high active material content, yet simultaneously exhibit improved flow behavior and electronic conductivity. The ability to independently tune the stability of two (or more) particle populations enables one to engineer concentrated suspensions that exhibit flow behavior akin to that observed for purely attractive electrode systems, while achieving far higher electronic conductivities. Given their enhanced performance, thicker electrodes can be used leading to more desirable transference numbers and higher theoretical areal energy densities. Our approach, which has been demonstrated for both LFP and LTO suspensions, opens news avenues for tailoring composite suspensions, including other mixtures of electrochemically active and electronically conductive species.

Chapter 6

Conclusions

My Ph.D. dissertation describes the design, fabrication and characterization of high energy density Li-ion batteries with ultrathick electrodes (up to 1.5 mm) for use in applications ranging from customized microbatteries to semisolid flow cells. Specifically, we developed concentrated electrode suspensions based on $LiFePO_4$ (cathode) and $Li_4Ti_5O_{12}$ (anode) in the absence and presence of a conductive carbon particle network. We carefully tailored flow behavior and electrochemical performance of the semisolid electrodes for both 3D printed LIBs and flow cell batteries. By controlling interparticle interactions, we created high areal capacity Li-ion batteries (LIBs) for applications across multiple scales. The ability to fabricate 3D-printed LIBs in arbitrary form factors opens new avenues for electronic device design. In addition, the efficient and scalable biphasic semisolid flow cells offer a promising approach for grid-scale energy storage.

The principal findings of my Ph.D. research are summarized below:

I. Li-ion Microbatteries

- **LFP and LTO Inks**

  We developed concentrated (~20 vol%) LFP and LTO inks that readily flow through fine nozzles (30 μm). The inks are prepared by suspending LFP and LTO nanoparticles in a solution composed of deionized water, humectants, and cellulose-based viscosifier via multi-step process that involves particle dispersion, centrifugation, and homogenization. In addition to their shear thinning and yield-stress behavior required for DIW, these viscoelastic inks show excellent shape

retention in their printed features, owing to rapid (re)solidification, high yield stress and shear elastic modulus.

- **3D Printed Interdigitated Electrode Architectures**

  We created Li-ion microbatteries by direct writing of concentrated LFP and LTO inks in the form of interdigitated, high aspect ratio electrodes on patterned gold current collectors. The printed electrodes (width ~ 60 μm and height ≤ 400 μm), whose total volume is below 1 mm^3, were slightly sintered to form amorphous carbon to improve electronic conductivity. To demonstrate the versatility of 3DP, we printed a 2D-array of LTO electrodes and one directed on the side of a pencil.

- **Electrochemical Performance**

  The printed microbatteries delivered amongst the highest areal energy density (9.7 J cm^{-2}) and power density (2.7 mW cm^{-2}) reported to date. Half-cells with printed LFP or LTO electrodes showed specific discharge capacities of 160 and 131 mAh/g (1 C), whereas the full-cell delivered areal capacity of ~1.5 mAh cm^{-2} at a stable working voltage of 1.8 V when discharged below 5C. Cycle life study (30 cycles) also showed minimal capacity decay. Packaged full-cell recorded stable oxidation and reduction peaks at 1.3 V and 2.4 V, and delivered 1.2 mAh cm^{-2} at 0.5 C, but did not exhibit long-term cyclability.

- **Limitations and Future Directions**

  Several issues must be addressed to further improve the performance of Li-ion microbatteries. First, the packaging process must enable better hermetic sealing. Second, the inactive area, volume and weight of the packaged battery must be minimized to enhance the energy and power densities. Third, the overall yield must be improved by overcoming electrode drying and sintering defects such as cracking

and delamination. Finally, conductive fillers must be incorporated into the electrode inks to enhance electronic transport and overcome the longer diffusion length of the thicker electrodes.

II. Li-ion Batteries with Ultrathick Electrodes

- **Biphasic LFP and LTO Ink Design and Flow Behavior**

  We created biphasic semisolid electrode inks that are electrolyte-infused (1M LiTFSI/PC) for direct writing of LIBs with ultrathick electrodes (~ 1 mm). Specifically, the interactions between the active particles, LFP or LTO, are rendered repulsive by sterically stabilizing them with a non-ionic dispersant, PVP while those between negligibly-coated conductive carbon particles are attractive. Notably, their cross-interactions (LFP-carbon or LTO-carbon) are also repulsive. We found both electronic conductivity and suspension homogeneity improve with increasing content of repulsive active particles. The biphasic inks also exhibit shear thinning and yield stress flow behavior required for DIW, and rapid (re)solidification for shape-retention. Our biphasic ink design enables high solids loading of active materials within a percolative network of conductive carbon particles, which gives rise to electrodes that simultaneously exhibit good flowability, fast charge transport (12 mS/cm), and high energy density (30 vol%).

- **Packaging and Separator Ink Design and Flow Behavior**

  We synthesized UV-curable packaging and separator inks to fully 3D print customizable Li-ion batteries. The packaging ink is a composite of hermetic-sealing UV-curing epoxy with fumed SiO_2 nanoparticles added as strengthening fillers. The separator ink is a composite of UV-curable ETPTA matrix with stabilized Al_2O_3 microparticles, infused with electrolyte (1M LiTFSI/PC). While

both inks exhibit shear-thinning and yield-stress behaviors, the packaging ink was designed to be mechanically strong for creating high aspect-ratio (width~0.250 mm, height~2.3 mm) casing, whereas the separator was tailored to be a soft gel for creating robust separators (100 μm) with high electrolyte content (50 vol%).

- **Electrochemical Performance of Biphasic Electrode Inks**

  We performed rigorous cycling tests at various electrode thicknesses (0.05~1 mm) and current densities (0.2 ~ 2 mA cm^{-2}) which show that our biphasic electrodes are capable of delivering areal capacities up to 14.5 mAh/cm^2 at 0.2 mA/cm^2 with 1 mm thick electrodes. Self-discharge study of a LFP/LTO full battery with 1 mm thick electrodes revealed 0.9% loss in capacity over 20 days, translating into a shelf life of 6 years. Repeated cycling (up to 250 days) revealed while Coulombic efficiency of thicker electrodes remain nominally 1 with only slight capacity decay, their energy and voltage efficiencies were found inferior to thinner electrodes. With 1 mm LFP/LTO electrodes, high areal energy density (~20 mWh/cm^2) at ~1 mW/cm^2 was achieved.

- **Glassy Carbon Current Collectors & Composite Separator**

  We utilized glassy carbon as current collectors to achieve excellent cycling performance with boosted energy efficiency (~90%), improved capacity retention over 160 cycles, while delivering areal capacity of 1.8 mAh/cm^2 at 0.2 mA/cm^2 with thin 100 μm thick electrodes. Coulombic efficiency is nominally one. Repeated cycling data (20+ cycles) using UV-cured composite separator film (thickness~100 μm) showed satisfactory performance albeit poorer energy efficiency (~80%) and

areal capacity (~1.2 mAh/cm2) at 0.2 mA/cm² compared to using a commercially available Celgard separator (thickness~20 μm).

- **Fully 3D Printed Open Square LIBs**

  We created 1 cm² open square LIBs (center through-hole: 0.36 cm²) with high active electrode content (54 vol%, 63 wt%) and low inactive packaging content (29 vol%, 23 wt%). This battery is fully 3D printed by first depositing packaging ink onto glassy carbon substrate (0.18 mm), followed by sequential printing of anode (1 mm), separator (0.1 mm), and cathode (1 mm) inks. A current collector lid (0.18 mm) capped off the printed structure and sealed with a thin layer of packaging ink (0.1 mm). The packaging and separator materials are UV-cured directly on the print platform.

- **Packaged Cell Performance & Future Directions**

  The fully 3D printed packaged open square LIBs delivered areal capacity of 4.45 mAh/cm² at a current density of 0.14 mA/cm², which is ~3 times higher than the previous unpackaged Li-ion microbattery. The low normalized capacity (43.35%), Coulombic efficiency (89%) and energy efficiency (67.7%) of the 3DP LIBs suggest improvements are required, including viscosifying the separator ink to improve film flatness, adopting a scraping mechanism for cleaner ink interfaces, and employing a pressure foot system to ensure firm interlayer contact.

III. Li-ion Semisolid Flow Batteries

- **Biphasic vs. Attractive LFP and LTO inks**

  We compared biphasic electrode suspensions (PVP-stabilized) with purely attractive electrode suspensions (without PVP) and found the former exhibit more homogenized particle distribution, lower yield-stress, and lower apparent viscosity.

The improved flowability of the biphasic electrode suspensions along with adequate active material loading (20 vol%) and uniformly distributed conductive carbon network (>10 mS/cm) make them highly suitable for semisolid flow cells.

- **Analytical Model Predictions**

  We developed an analytical model with a target current density of 10 mA cm^{-2} and voltage efficiency of 90% to find biphasic suspensions the only electrodes reported to date that simultaneously exhibit high energy density (i.e., high active-material loading), fast charge transfer (i.e., high electronic conductivity), and low-dissipation flow (i.e., low pressure drop). The model predicted pressure drop for the biphasic suspensions similar to those reported previously (1~10 psi), but exhibit electronic conductivities that are nearly two orders of magnitude higher, which allows for roughly 25 times thicker electrodes, therefore much higher areal capacities. The biphasic suspensions also possess nearly optimal electronic transference numbers ($\geq$ 0.5).

- **Electrochemical Performance of Static Cells**

  Half-cell static cycling test with a 0.5 mm thick LFP electrode showed initial specific capacity of 129 mAh g^{-1} at a rate of C/8. The capacity is stable for 100 cycles, with a capacity of 115 mAh g^{-1} on the 100th cycle, or a loss of 0.1% per cycle. Capacity is roughly the same at a rate of C/4, but drops significantly at C/2. Coulombic efficiency is consistently over 99% for the biphasic LFP suspension. Half-cell static cycling test with a 0.5 mm thick LTO electrode showed capacity up to 170 mAh g^{-1} at a rate of C/8, with Coulombic efficiencies exceeding 99%.

- **Electrochemical Performance of Flow Cells & Future Directions**

  We tested biphasic LFP electrode suspension in a lab-scale half-flow cell against a Li metal negative electrode, using the intermittent flow mode. Two aliquots of suspensions were pumped through the electroactive region (1.5 mm x 1.5 mm x 20 mm) for charging and discharging. An overall Coulombic efficiency of 72.3%, energetic efficiency of 63.1%, capacity of 131 mAh g^{-1} (equivalent to 93 Wh L^{-1}) were achieved at a current density of 1.67 mA cm^{-2}. The potential of semisolid flow cell could be further realized by replacing the non-ionic surfactant PVP with Triton X-100 (TX100) for better long term cyclability, and analyzing state of charge-dependency of rheological and electrochemical properties.

References

[1] G. Crabtree, E. Kócs, L. Trahey, *MRS Bull.* **2015**, *40*, 1067.
[2] J. M. Tarascon, M. Armand, *Nature Communications* **2001**, DOI 10.1038/35104644.
[3] I. Gyuk, M. Johnson, J. Vetrano, K. Lynn, W. Parks, R. Handa, L. Kannberg, S. Hearne, K. Waldrip, R. Braccio, *Grid Energy Storage*, Washington, DC, **2013**.
[4] B. Nykvist, M. Nilsson, *Nature Climate change* **2015**, *5*, 329.
[5] X. Luo, J. Wang, M. Dooner, J. Clarke, *Applied Energy* **2015**, *137*, 511.
[6] J. Liu, D. G. D. Galpaya, L. Yan, M. Sun, Z. Lin, C. Yan, C. Liang, S. Zhang, *Energy Environ. Sci.* **2017**, DOI 10.1039/C6EE03033E.
[7] M. Duduta, B. Ho, V. C. Wood, P. Limthongkul, V. E. Brunini, W. C. Carter, Y.-M. Chiang, *Adv. Energy Mater.* **2011**, *1*, 511.
[8] G.-F. Yang, K.-Y. Song, S.-K. Joo, *RSC Adv.* **2015**, *5*, 16702.
[9] Q. Huang, J. Yang, C. B. Ng, C. Jia, Q. Wang, *Energy Environ. Sci.* **2016**, *9*, 917.
[10] S. M. Spearing, *Acta Materialia* **2000**, *48*, 179.
[11] C. Zhang, J. Xu, W. Ma, W. Zheng, *Biotechnology Advances* **2006**, *24*, 243.
[12] D. A. LaVan, T. McGuire, R. Langer, *Nat Biotechnol* **2003**, *21*, 1184.
[13] J. D. Fowler, M. J. Allen, V. C. Tung, Y. Yang, R. B. Kaner, B. H. Weiller, *ACS Nano* **2009**, *3*, 301.
[14] P. S. Waggoner, H. G. Craighead, *Lab Chip* **2007**, *7*, 1238.
[15] M. Carbajales-Dale, C. J. Barnhart, S. M. Benson, *Energy Environ. Sci.* **2014**, *7*, 1538.
[16] S. Chu, A. Majumdar, *Nature Communications* **2012**, *488*, 294.
[17] M. R. Palacin, A. de Guibert, *Science* **2016**, *351*, 1253292.
[18] Y. Sun, N. Liu, Y. Cui, *Nat. Energy* **2016**, *1*, 16071.
[19] H. Gao, T. Zhou, Y. Zheng, Y. Liu, J. Chen, H. Liu, Z. Guo, *Adv. Energy Mater.* **2016**, *6*, 1601037.
[20] F. Shen, W. Luo, J. Dai, Y. Yao, M. Zhu, E. Hitz, Y. Tang, Y. Chen, V. L. Sprenkle, X. Li, L. Hu, *Adv. Energy Mater.* **2016**, *6*, 1600377.
[21] C. Zhu, P. Kopold, P. A. van Aken, J. Maier, Y. Yu, *Adv. Mater.* **2016**, *28*, 2409.
[22] D. Kundu, E. Talaie, V. Duffort, L. F. Nazar, *Angew. Chem. Int. Ed.* **2015**, *54*, 3431.
[23] F. Wang, Y. Lin, L. Suo, X. Fan, T. Gao, C. Yang, *Energy Environ. Sci.* **2016**, *9*, 3666.
[24] Y. Yamada, K. Usui, K. Sodeyama, S. Ko, Y. Tateyama, A. Yamada, *Nat. Energy* **2016**, *1*, 16129.
[25] Z. Hou, X. Li, J. Liang, Y. Zhu, Y. Qian, *J. Mater. Chem. A* **2015**, *3*, 1400.
[26] J. F. Whitacre, S. Shanbhag, A. Mohamed, A. Polonsky, K. Carlisle, J. Gulakowski, W. Wu, C. Smith, L. Cooney, D. Blackwood, J. C. Dandrea, C. Truchot, *Energy Technology* **2014**, *3*, 20.
[27] J. Wang, Y. Yamada, K. Sodeyama, C. H. Chiang, Y. Tateyama, A. Yamada, *Nature Communications* **2016**, *7*, 12032.
[28] A. M. Haregewoin, A. S. Wotango, B. J. Hwang, *Energy Environ. Sci.* **2016**, *9*, 1955.
[29] Y.-S. Hu, *Nat. Energy* **2016**, *1*, 16042.

[30] D. T. Hallinan Jr., N. P. Balsara, *Annu. Rev. Mater. Res.* **2013**, *43*, 503.
[31] W. G. Chong, J.-Q. Huang, Z.-L. Xu, X. Qin, X. Wang, J.-K. Kim, *Adv. Funct. Mater.* **2016**, 1604815.
[32] Q. Huang, D. Wang, Z. Zheng, *Adv. Energy Mater.* **2016**, *6*, 1600783.
[33] Y. H. Kwon, S.-W. Woo, H.-R. Jung, H. K. Yu, K. Kim, B. H. Oh, S. Ahn, S.-Y. Lee, S.-W. Song, J. Cho, H.-C. Shin, J. Y. Kim, *Adv. Mater.* **2012**, *24*, 5192.
[34] W. Liu, M.-S. Song, B. Kong, Y. Cui, *Adv. Mater.* **2016**, DOI 10.1002/adma.201603436.
[35] F. Wu, E. Zhao, D. Gordon, Y. Xiao, C. Hu, G. Yushin, *Adv. Mater.* **2016**, *28*, 6365.
[36] Z. Song, X. Wang, C. Lv, Y. An, M. Liang, T. Ma, D. He, Y.-J. Zheng, S.-Q. Huang, H. Yu, H. Jiang, *Sci. Rep.* **2015**, *5*, 10988.
[37] A. M. Gaikwad, B. V. Khau, G. Davies, B. Hertzberg, D. A. Steingart, A. C. Arias, *Adv. Energy Mater.* **2014**, *5*, 1401389.
[38] T.-S. Wei, F. Y. Fan, A. Helal, K. C. Smith, G. H. McKinley, Y.-M. Chiang, J. A. Lewis, *Adv. Energy Mater.* **2015**, *5*, 1500535.
[39] F. Y. Fan, W. H. Woodford, Z. Li, N. Baram, K. C. Smith, A. Helal, G. H. McKinley, W. C. Carter, Y.-M. Chiang, *Nano Lett.* **2014**, *14*, 2210.
[40] Z. Li, K. C. Smith, Y. Dong, N. Baram, F. Y. Fan, J. Xie, P. Limthongkul, W. C. Carter, Y.-M. Chiang, *Phys. Chem. Chem. Phys.* **2013**, *15*, 15833.
[41] N. Nitta, F. Wu, J. T. Lee, G. Yushin, *Materials Today* **2015**, *18*, 252.
[42] X. Zhang, W. Shyy, A. Marie Sastry, *J. Electrochem. Soc.* **2007**, *154*, A910.
[43] T. Sasaki, Y. Ukyo, P. Novák, *Nature Materials* **2013**, *12*, 569.
[44] L. A.-W. Ellingsen, C. R. Hung, G. Majeau-Bettez, B. Singh, Z. Chen, M. S. Whittingham, A. H. Strømman, *Nature Nanotechnology* **2016**, *11*, 1039.
[45] S.-Y. Chung, J. T. Bloking, Y.-M. Chiang, *Nature Materials* **2002**, *1*, 123.
[46] B. Kang, G. Ceder, *Nature Communications* **2009**, *458*, 190.
[47] B. Wang, T. Liu, A. Liu, G. Liu, L. Wang, T. Gao, D. Wang, X. S. Zhao, *Adv. Energy Mater.* **2016**, *6*, 1600426.
[48] C. M. Julien, K. Zaghib, A. Mauger, M. Massot, A. Ait-Salah, M. Selmane, F. Gendron, *J. Appl. Phys.* **2006**, *100*, 063511.
[49] B. Lung-Hao Hu, F.-Y. Wu, C.-T. Lin, A. N. Khlobystov, L.-J. Li, *Nature Communications* **2013**, *4*, 1687.
[50] X. Rui, X. Zhao, Z. Lu, H. Tan, D. Sim, H. H. Hng, R. Yazami, T. M. Lim, Q. Yan, *ACS Nano* **2013**, *7*, 5637.
[51] K. Naoi, K. Kisu, E. Iwama, S. Nakashima, Y. Sakai, Y. Orikasa, P. Leone, N. Dupré, T. Brousse, P. Rozier, W. Naoi, P. Simon, *Energy Environ. Sci.* **2016**, *9*, 2143.
[52] F. Ding, W. Xu, G. L. Graff, J. Zhang, M. L. Sushko, X. Chen, Y. Shao, M. H. Engelhard, Z. Nie, J. Xiao, X. Liu, P. V. Sushko, J. Liu, J.-G. Zhang, *J. Am. Chem. Soc.* **2013**, *135*, 4450.
[53] F. Ronci, P. Reale, B. Scrosati, S. Panero, V. Rossi Albertini, P. Perfetti, M. di Michiel, J. M. Merino, *J. Phys. Chem. B* **2002**, *106*, 3082.
[54] T.-F. Yi, Y. Xie, Y.-R. Zhu, R.-S. Zhu, H. Shen, *Journal of Power Sources* **2013**, *222*, 448.
[55] M. V. Reddy, G. V. Subba Rao, B. V. R. Chowdari, *Chem. Rev.* **2013**, *113*, 5364.
[56] E. Pohjalainen, T. Rauhala, M. Valkeapää, J. Kallioinen, T. Kallio, *J. Phys.*

Chem. C **2015**, *119*, 2277.
[57] C. Jiang, M. Ichihara, I. Honma, H. Zhou, *Electrochimica Acta* **2007**, *52*, 6470.
[58] H.-G. Jung, M. W. Jang, J. Hassoun, Y.-K. Sun, B. Scrosati, *Nature Communications* **2011**, *2*, 516.
[59] Y.-B. He, B. Li, M. Liu, C. Zhang, W. Lv, C. Yang, J. Li, H. Du, B. Zhang, Q.-H. Yang, J.-K. Kim, F. Kang, *Sci. Rep.* **2012**, *2*, DOI 10.1038/srep00913.
[60] S.-H. Kim, K.-H. Choi, S.-J. Cho, S. Choi, S. Park, S.-Y. Lee, *Nano Lett.* **2015**, *15*, 5168.
[61] S. Jaiser, M. Müller, M. Baunach, W. Bauer, P. Scharfer, W. Schabel, *Journal of Power Sources* **2016**, *318*, 210.
[62] J. H. Prosser, T. Brugarolas, S. Lee, A. J. Nolte, D. Lee, *Nano Lett.* **2012**, *12*, 5287.
[63] M. Singh, J. Kaiser, H. Hahn, *J. Electrochem. Soc.* **2015**, *162*, A1196.
[64] S. Lim, S. Kim, K. H. Ahn, S. J. Lee, *Ind. Eng. Chem. Res.* **2015**, *54*, 6146.
[65] K. B. Singh, M. S. Tirumkudulu, *Phys. Rev. Lett.* **2007**, *98*, 218302.
[66] W. P. Lee, A. F. Routh, *Langmuir* **2004**, *20*, 9885.
[67] Y. Li, K. Yan, H.-W. Lee, Z. Lu, N. Liu, Y. Cui, *Nat. Energy* **2016**, *1*, 15029.
[68] H. Zheng, J. Li, X. Song, G. Liu, V. S. Battaglia, *Electrochimica Acta* **2012**, *71*, 258.
[69] F. Jiang, P. Peng, *Sci. Rep.* **2016**, *6*, 32639.
[70] R. Zhao, J. Liu, J. Gu, *Applied Energy* **2015**, *139*, 220.
[71] M. F. Hasan, C. F. Chen, C. E. Shaffer, P. P. Mukherjee, *J. Electrochem. Soc.* **2015**, *162*, A1382.
[72] D. Lv, J. Zheng, Q. Li, X. Xie, S. Ferrara, Z. Nie, L. B. Mehdi, N. D. Browning, J.-G. Zhang, G. L. Graff, J. Liu, J. Xiao, *Adv. Energy Mater.* **2015**, *5*, 1402290.
[73] W. Porcher, B. Lestriez, S. Jouanneau, *Journal of The Electrochemical Society* **2009**, DOI 10.1149/1.3046129.
[74] C.-C. Li, Y.-W. Wang, *J. Electrochem. Soc.* **2011**, *158*, A1361.
[75] J. S. Sander, R. M. Erb, L. Li, A. Gurijala, Y. M. Chiang, *Nat. Energy* **2016**, *1*, 16099.
[76] W. Lai, C. K. Erdonmez, T. F. Marinis, C. K. Bjune, N. J. Dudney, F. Xu, R. Wartena, Y.-M. Chiang, *Adv. Mater.* **2010**, *22*, E139.
[77] L. Hu, F. La Mantia, H. Wu, X. Xie, J. McDonough, M. Pasta, Y. Cui, *Adv. Energy Mater.* **2011**, *1*, 1012.
[78] J. S. Wang, P. Liu, E. Sherman, M. Verbrugge, H. Tataria, *Journal of Power Sources* **2011**, *196*, 8714.
[79] R. L. Truby, J. A. Lewis, *Nature Communications* **2016**, *540*, 371.
[80] A. Ambrosi, M. Pumera, *Chem. Soc. Rev.* **2016**, *45*, 2740.
[81] L. Hirt, A. Reiser, R. Spolenak, T. Zambelli, *Adv. Mater.* **2017**, 1604211.
[82] M. A. Skylar-Scott, S. Gunasekaran, J. A. Lewis, *PNAS* **2016**, *113*, 6137.
[83] N. Zhou, C. Liu, J. A. Lewis, D. Ham, *Adv. Mater.* **2017**, *15*, 1605198.
[84] A. Sydney Gladman, E. A. Matsumoto, R. G. Nuzzo, L. Mahadevan, J. A. Lewis, *Nature Materials* **2016**, *15*, 413.
[85] Y. L. Kong, I. A. Tamargo, H. Kim, B. N. Johnson, M. K. Gupta, T.-W. Koh, H.-A. Chin, D. A. Steingart, B. P. Rand, M. C. McAlpine, *Nano Lett.* **2014**, *14*, 7017.

[86] C. Ladd, J.-H. So, J. Muth, M. D. Dickey, *Adv. Mater.* **2013**, *25*, 5081.
[87] J. W. Boley, E. L. White, G. T. C. Chiu, R. K. Kramer, *Adv. Funct. Mater.* **2014**, *24*, 3501.
[88] J. J. Adams, E. B. Duoss, T. F. Malkowski, M. J. Motala, B. Y. Ahn, R. G. Nuzzo, J. T. Bernhard, J. A. Lewis, *Adv. Mater.* **2011**, *23*, 1335.
[89] J. T. Muth, P. G. Dixon, L. Woish, L. J. Gibson, J. A. Lewis, *PNAS* **2017**, *114*, 1832.
[90] C. Minas, D. Carnelli, E. Tervoort, A. R. Studart, *Adv. Mater.* **2016**, *28*, 9993.
[91] R. D. Farahani, M. Dubé, D. Therriault, *Adv. Mater.* **2016**, *28*, 5794.
[92] B. G. Compton, J. A. Lewis, *Adv. Mater.* **2014**, *26*, 5930.
[93] L. S. Dimas, G. H. Bratzel, I. Eylon, M. J. Buehler, *Adv. Funct. Mater.* **2013**, *23*, 4629.
[94] J. W. Boley, K. Chaudhary, T. J. Ober, M. Khorasaninejad, W. T. Chen, E. Hanson, A. Kulkarni, J. Oh, J. Kim, L. K. Aagesen, A. Y. Zhu, F. Capasso, K. Thornton, P. V. Braun, J. A. Lewis, *Adv. Mater.* **2016**, 1604778.
[95] G. M. Gratson, F. García-Santamaría, V. Lousse, M. Xu, S. Fan, J. A. Lewis, P. V. Braun, *Adv. Mater.* **2006**, *18*, 461.
[96] D. J. Lorang, D. Tanaka, C. M. Spadaccini, K. A. Rose, N. J. Cherepy, J. A. Lewis, *Adv. Mater.* **2011**, *23*, 5055.
[97] M. Wehner, R. L. Truby, D. J. Fitzgerald, B. Mosadegh, G. M. Whitesides, J. A. Lewis, R. J. Wood, *Nature Communications* **2016**, *536*, 451.
[98] K. A. Homan, D. B. Kolesky, M. A. Skylar-Scott, J. Herrmann, H. Obuobi, A. Moisan, J. A. Lewis, *Sci. Rep.* **2016**, *6*, 34845.
[99] D. B. Kolesky, K. A. Homan, M. A. Skylar-Scott, J. A. Lewis, *PNAS* **2016**, *113*, 3179.
[100] A. E. Jakus, E. B. Secor, A. L. Rutz, S. W. Jordan, M. C. Hersam, R. N. Shah, *ACS Nano* **2015**, *9*, 4636.
[101] S. V. Murphy, A. Atala, *Nature Publishing Group* **2014**, *32*, 773.
[102] F. Pati, J. Jang, D.-H. Ha, S. Won Kim, J.-W. Rhie, J.-H. Shim, D.-H. Kim, D.-W. Cho, *Nature Communications* **2014**, *5*, DOI 10.1038/ncomms4935.
[103] S. Bose, S. Vahabzadeh, A. Bandyopadhyay, *Materials Today* **2013**, *16*, 496.
[104] K. Sun, T.-S. Wei, B. Y. Ahn, J. Y. Seo, S. J. Dillon, J. A. Lewis, *Adv. Mater.* **2013**, *25*, 4539.
[105] J. A. Lewis, J. E. Smay, J. Stuecker, J. Cesarano, *J American Ceramic Society* **2006**, *89*, 3599.
[106] A. Kraytsberg, Y. Ein-Eli, *Adv. Energy Mater.* **2016**, *6*, 1600655.
[107] S. K. Rhodes, R. H. Lambeth, J. Gonzales, J. S. Moore, J. A. Lewis, *Langmuir* **2009**, *25*, 6787.
[108] S. R. Ferreira, Structure and Dynamics of Biphasic Colloidal Mixtures, Unpublished, **n.d.**
[109] A. Mohraz, E. R. Weeks, J. A. Lewis, *Phys. Rev. E* **2008**, *77*, 060403.
[110] *Chem. Rev.* **2011**, *111*, 3577.
[111] A. Z. Weber, M. M. Mench, J. P. Meyers, P. N. Ross, J. T. Gostick, Q. Liu, *J Appl Electrochem* **2011**, *41*, 1137.
[112] C. Ponce de León, A. Frías-Ferrer, J. González-García, D. A. Szánto, F. C. Walsh, *Journal of Power Sources* **2006**, *160*, 716.
[113] R. M. Darling, K. G. Gallagher, J. A. Kowalski, S. Ha, F. R. Brushett, *Energy*

Environ. Sci. **2014**, *7*, 3459.
[114] V. Presser, C. R. Dennison, J. Campos, K. W. Knehr, E. C. Kumbur, Y. Gogotsi, *Adv. Energy Mater.* **2012**, *2*, 895.
[115] K. C. Smith, Y. M. Chiang, W. Craig Carter, *J. Electrochem. Soc.* **2014**, *161*, A486.
[116] J. W. Long, D. R. Rolison, *Acc. Chem. Res.* **2007**, *40*, 854.
[117] M. Armand, J. M. Tarascon, *Nature Communications* **2008**, *451*, 652.
[118] J. W. Long, B. Dunn, D. R. Rolison, H. S. White, *Chem. Rev.* **2004**, *104*, 4463.
[119] T. S. Arthur, D. J. Bates, N. Cirigliano, D. C. Johnson, P. Malati, J. M. Mosby, E. Perre, M. T. Rawls, A. L. Prieto, B. Dunn, *MRS Bull.* **2011**, *36*, 523.
[120] A. M. Gaikwad, G. L. Whiting, D. A. Steingart, A. C. Arias, *Adv. Mater.* **2011**, *23*, 3251.
[121] S. R. Gowda, A. Leela Mohana Reddy, X. Zhan, P. M. Ajayan, *Nano Lett.* **2011**, *11*, 3329.
[122] L. Baggetto, R. A. H. Niessen, F. Roozeboom, P. H. L. Notten, *Adv. Funct. Mater.* **2008**, *18*, 1057.
[123] M. Nathan, D. Golodnitsky, V. Yufit, E. Strauss, T. Ripenbein, I. Shechtman, S. Menkin, E. Peled, *J. Microelectromech. Syst.* **2005**, *14*, 879.
[124] H. Zhang, X. Yu, P. V. Braun, *Nature Nanotechnology* **2011**, *6*, 277.
[125] J. A. Lewis, *Adv. Funct. Mater.* **2006**, *16*, 2193.
[126] J. A. Lewis, G. M. Gratson, *Materials Today* **2004**, *7*, 32.
[127] B. Y. Ahn, E. B. Duoss, M. J. Motala, X. Guo, S. I. Park, Y. Xiong, J. Yoon, R. G. Nuzzo, J. A. Rogers, J. A. Lewis, *Science* **2009**, *323*, 1590.
[128] J. E. Smay, G. M. Gratson, R. F. Shepherd, J. Cesarano, J. A. Lewis, *Adv. Mater.* **2002**.
[129] K. Zaghib, M. Armand, M. Gauthier, *Journal of the Electrochemical ...* **1998**.
[130] J. Li, C. Daniel, D. Wood, *Journal of Power Sources* **2011**, *196*, 2452.
[131] R. E. Garcı´a, Y.-M. Chiang, W. Craig Carter, P. Limthongkul, C. M. Bishop, *J. Electrochem. Soc.* **2005**, *152*, A255.
[132] J. Wolfenstine, J. L. Allen, *Journal of Power Sources* **2008**, *180*, 582.
[133] H.-S. Min, B. Y. Park, L. Taherabadi, C. Wang, Y. Yeh, R. Zaouk, M. J. Madou, B. Dunn, *Journal of Power Sources* **2008**, *178*, 795.
[134] M. Nishizawa, K. Mukai, S. Kuwabata, C. R. Martin, H. Yoneyama, *Journal of The Electrochemical Society* **1997**, *144*, 1923.
[135] M. Kotobuki, Y. Suzuki, H. Munakata, K. Kanamura, Y. Sato, K. Yamamoto, T. Yoshida, *Electrochimica Acta* **2011**, *56*, 1023.
[136] S. K. Cheah, E. Perre, M. Rooth, M. Fondell, A. Hårsta, L. Nyholm, M. Boman, T. Gustafsson, J. Lu, P. Simon, K. Edstrom, *Nano Lett.* **2009**, *9*, 3230.
[137] M. M. Shaijumon, E. Perre, B. Daffos, P.-L. Taberna, J.-M. Tarascon, P. Simon, *Adv. Mater.* **2010**, *22*, 4978.
[138] H. Mazor, D. Golodnitsky, L. Burstein, A. Gladkich, E. Peled, *Journal of Power Sources* **2012**, *198*, 264.
[139] H. Kim, J. Proell, R. Kohler, W. Pfleging, A. Pique, *J Laser Micro/Nanoeng* **2012**.
[140] S. R. Gowda, A. Leela Mohana Reddy, X. Zhan, H. R. Jafry, P. M. Ajayan, *Nano Lett.* **2012**, *12*, 1198.
[141] K. Yoshima, H. Munakata, K. Kanamura, *Journal of Power Sources* **2012**,

208, 404.
[142] J. B. Bates, N. J. Dudney, B. Neudecker, A. Ueda, C. D. Evans, *Solid State Ionics* **2000**, *135*, 33.
[143] J. H. Pikul, H. Gang Zhang, J. Cho, P. V. Braun, W. P. King, *Nature Communications* **2013**, *4*, 1732.
[144] N. Liu, Z. Lu, J. Zhao, M. T. McDowell, H.-W. Lee, W. Zhao, Y. Cui, *Nature Nanotechnology* **2014**, *9*, 187.
[145] B. Li, S. Li, J. Xu, S. Yang, *Energy Environ. Sci.* **2016**, *9*, 2025.
[146] X. Wang, Y. Fan, R. A. Susantyoko, Q. Xiao, L. Sun, D. He, Q. Zhang, *Nano Energy* **2014**, *5*, 91.
[147] M. Youssry, L. Madec, P. Soudan, M. Cerbelaud, D. Guyomard, B. Lestriez, *Phys. Chem. Chem. Phys.* **2013**, *15*, 14476.
[148] T. Nishida, K. Nishikawa, Y. Fukunaka, in *211th ECS Meeting*, Ecs, **n.d.**, pp. 1–14.
[149] J. N. Israelachvili, *Intermolecular and Surface Forces*, Academic Press, San Diego, CA, **1992**.
[150] Y. Zhao, S. Wang, C. Zhao, D. Xia, *Rare Metals* **2009**, *28*, 117.
[151] H. Wang, X. Qiao, J. Chen, X. Wang, S. Ding, *Materials Chemistry and Physics* **2005**, *94*, 449.
[152] L. Zhang, Y. Jiang, Y. Ding, M. Povey, D. York, *J Nanopart Res* **2006**, *9*, 479.
[153] J. Zhang, D. Jiang, Q. Lin, *J American Ceramic Society* **2005**, *88*, 1054.
[154] K. C. Smith, P. P. Mukherjee, T. S. Fisher, *Phys. Chem. Chem. Phys.* **2012**, *14*, 7040.
[155] S.-H. Kim, K.-H. Choi, S.-J. Cho, E.-H. Kil, S.-Y. Lee, *J. Mater. Chem. A* **2013**, *1*, 4949.
[156] N. J. Dudney, J. Li, *Science* **2015**, DOI 10.1126/science.aaa2643.
[157] Z.-A. Zhang, C.-M. Qu, M. Jia, Y.-Q. Lai, J. Li, *J. Cent. South Univ.* **2014**, *21*, 2604.
[158] B. P. N. Nguyen, S. Chazelle, M. Cerbelaud, W. Porcher, B. Lestriez, *Journal of Power Sources* **2014**, *262*, 112.
[159] Y. Li, S. Meyer, J. Lim, S. C. Lee, W. E. Gent, S. Marchesini, H. Krishnan, T. Tyliszczak, D. Shapiro, A. L. D. Kilcoyne, W. C. Chueh, *Adv. Mater.* **2015**, *27*, 6591.
[160] S. Yamada, H. Sato, *Nature Communications* **1962**.
[161] Y. Gogotsi, P. Simon, *True Performance Metrics in Electrochemical Energy Storage (November, Pg 917, 2011)*, Science, **2012**.
[162] Q. Cheng, Z. Song, T. Ma, B. B. Smith, R. Tang, H. Yu, H. Jiang, C. K. Chan, *Nano Lett.* **2013**, *13*, 4969.
[163] W. Liu, Z. Chen, G. Zhou, Y. Sun, H. R. Lee, C. Liu, H. Yao, Z. Bao, Y. Cui, *Adv. Mater.* **2016**, *28*, 3578.
[164] K. Fu, Y. Wang, C. Yan, Y. Yao, Y. Chen, J. Dai, S. Lacey, Y. Wang, J. Wan, T. Li, Z. Wang, Y. Xu, L. Hu, *Adv. Mater.* **2016**, *28*, 2587.
[165] E. C. Self, R. Wycisk, P. N. Pintauro, *Journal of Power Sources* **2015**, *282*, 187.
[166] W. Weng, Q. Sun, Y. Zhang, S. He, Q. Wu, J. Deng, X. Fang, G. Guan, J. Ren, H. Peng, *Adv. Mater.* **2015**, *27*, 1363.
[167] L. Madec, M. Youssry, M. Cerbelaud, P. Soudan, D. Guyomard, B. Lestriez, *ChemPlusChem* **2014**, *80*, 396.

[168] S. Hamelet, T. Tzedakis, J. B. Leriche, S. Sailler, D. Larcher, P. L. Taberna, P. Simon, J. M. Tarascon, *J. Electrochem. Soc.* **2012**, *159*, A1360.
[169] S. Hamelet, D. Larcher, L. Dupont, J. M. Tarascon, *J. Electrochem. Soc.* **2013**, *160*, A516.
[170] V. E. Brunini, Y.-M. Chiang, W. C. Carter, *Electrochimica Acta* **2012**, *69*, 301.
[171] M. Zhu, J. Park, A. M. Sastry, W. Lu, *J. Electrochem. Soc.* **2014**, *161*, A1247.
[172] B. Y. Ho, An Experimental Study on the Structure-Property Relationship of Composite Fluid Electrodes for Use in High Energy Density Semi-Solid Flow Cells, Massachusetts Institute of Technology, **2012**.
[173] G. Ovarlez, S. Cohen-Addad, K. Krishan, J. Goyon, P. Coussot, *Journal of Non-Newtonian Fluid Mechanics* **2013**, *193*, 68.
[174] A. Yoshimura, R. K. Prud'homme, *J. Rheol.* **1988**, *32*, 53.
[175] R. Buscall, *J. Rheol.* **2010**, *54*, 1177.
[176] H. A. Barnes, *Journal of Non-Newtonian Fluid Mechanics* **1995**, *56*, 221.
[177] P. Coussot, *Rheometry of Pastes, Suspensions, and Granular Materials: Applications in Industry and Environment*, Wiley Interscience, Hoboken, NJ, **2005**.
[178] H. A. Barnes, *Journal of Non-Newtonian Fluid Mechanics* **1999**, *81*, 133.
[179] Z. Rotem, *J. Appl. Mech.* **1962**, *29*, 421.
[180] K. C. Smith, V. E. Brunini, Y. Dong, Y.-M. Chiang, W. C. Carter, *Electrochimica Acta* **2014**, *147*, 460.
[181] L. Madec, M. Youssry, M. Cerbelaud, P. Soudan, D. Guyomard, B. Lestriez, *J. Electrochem. Soc.* **2014**, *161*, A693.
[182] B. J. Hopkins, K. C. Smith, A. H. Slocum, Y.-M. Chiang, *Journal of Power Sources* **2015**, *293*, 1032.
[183] D. Young, A. Ransil, R. Amin, Z. Li, Y.-M. Chiang, *Adv. Energy Mater.* **2013**, *3*, 1125.
[184] M. Youssry, L. Madec, P. Soudan, M. Cerbelaud, D. Guyomard, B. Lestriez, *Journal of Power Sources* **2015**, *274*, 424.
[185] A. Yermukhambetova, C. Tan, S. R. Daemi, Z. Bakenov, J. A. Darr, D. J. L. Brett, P. R. Shearing, *Sci. Rep.* **2016**, *6*, 35291.
[186] J. Billaud, F. Bouville, T. Magrini, C. Villevieille, A. R. Studart, *Nat. Energy* **2016**, *1*, 16097.
[187] D. S. Eastwood, V. Yufit, J. Gelb, A. Gu, R. S. Bradley, S. J. Harris, D. J. L. Brett, N. P. Brandon, P. D. Lee, P. J. Withers, P. R. Shearing, *Adv. Energy Mater.* **2013**, *4*, 1300506.
[188] M. Ebner, F. Marone, M. Stampanoni, V. Wood, *Science* **2013**, DOI 10.1007/978-1-4419-9863-7_101414.
[189] Q. Zhao, C. E. Finlayson, D. R. E. Snoswell, A. Haines, C. Schäfer, P. Spahn, G. P. Hellmann, A. V. Petukhov, L. Herrmann, P. Burdet, P. A. Midgley, S. Butler, M. Mackley, Q. Guo, J. J. Baumberg, *Nature Communications* **2016**, *7*, 11661.